Shock and Vibration

The Mechanism, Characteristics and Risk Assessments of Seismic Landslides

Lead Guest Editor: Lanmin Wang
Guest Editors: Ai Lan Che, Hemanta Hazarika, and Zhi-Jian Wu

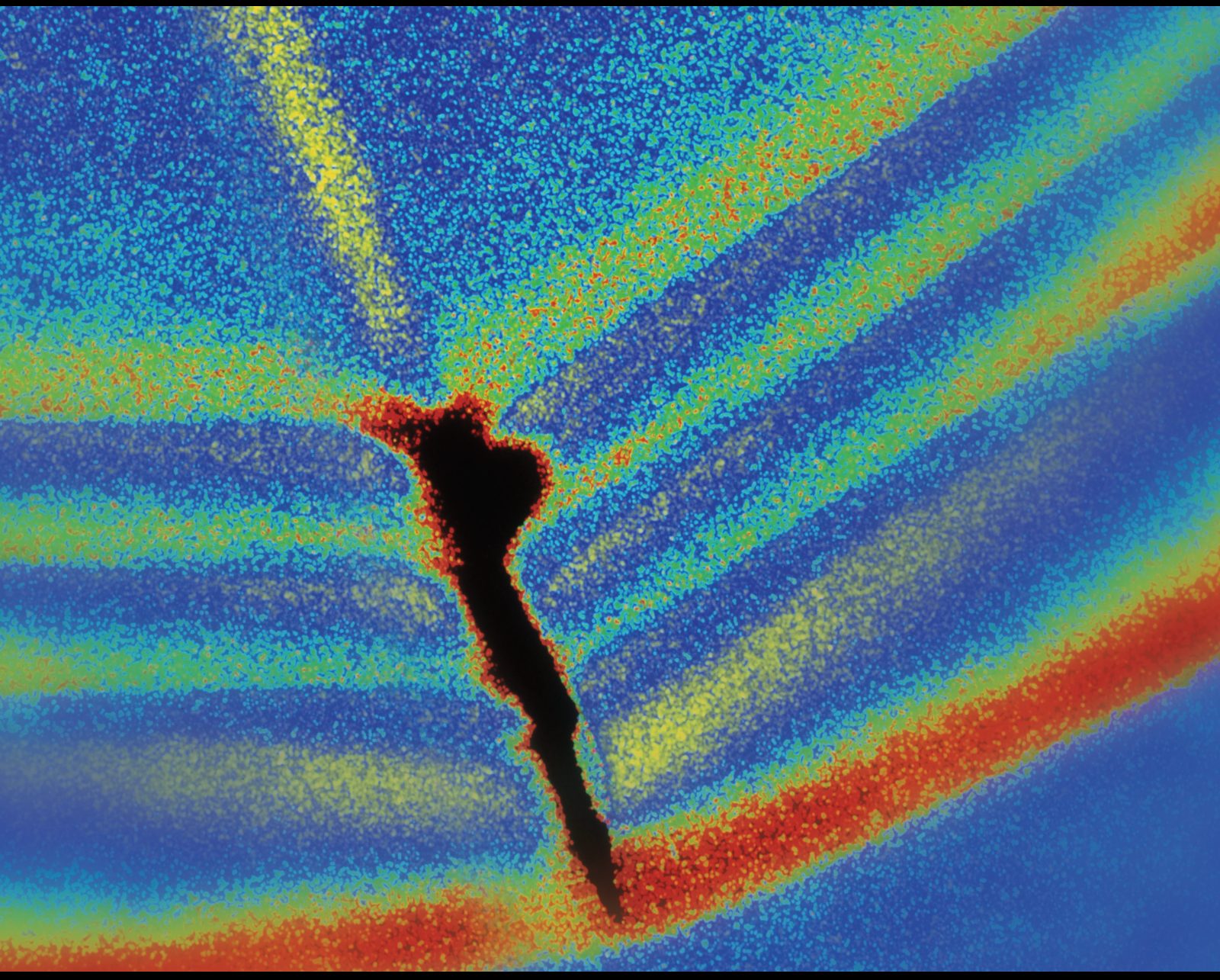

The Mechanism, Characteristics and Risk Assessments of Seismic Landslides

Shock and Vibration

The Mechanism, Characteristics and Risk Assessments of Seismic Landslides

Lead Guest Editor: Lanmin Wang
Guest Editors: Ai Lan Che, Hemanta Hazarika, and Zhi-Jian Wu

Contents

Hindawi
Shock and Vibration
Volume 2024, Article ID 3510391, 15 pages
https://doi.org/10.1155/2024/3510391

Research Article

Field Testing and Numerical Simulation of the Dynamic Response of Loess Hill Site under High-Speed Train Load

Wujian Yan,[1] **Xinxin Tian**,[1] **Ping Wang**,[1] **Lin Kang**,[1] **and Zhijian Wu**[2]

[1]*Lanzhou Institute of Seismology, Key Laboratory of Loess Earthquake Engineering, China Earthquake Administration, Lanzhou 730000, China*
[2]*College of Transportation Engineering, Nanjing Tech University, Nanjing 211800, China*

Correspondence should be addressed to Zhijian Wu; zhijian@njtech.edu.cn

Received 31 July 2022; Revised 18 January 2023; Accepted 30 December 2023; Published 27 February 2024

Academic Editor: W. Zhang

In this study, the loess hill site of an elevated bridge section in Tongwei-Qin'an of the Baolan high-speed railroad was selected as the research object, and the vibration acceleration of the loess hill site under the elevated bridge was tested in the field under the train operating load. The results show that under the same intensity of train load, the time range of vibration acceleration observed by field test and numerical simulation decays linearly with increasing distance from the source, while the amplification effect appears in the loess hill site at a greater distance, and the vibration duration also appears to increase. The vibration acceleration waveforms at each observation point observed by field tests and numerical simulations are similar, and the peak vertical acceleration at each observation point obtained from numerical simulations is overall greater than the peak acceleration at each point obtained from field tests, with $a_{\text{Simulated}-\max}/a_{\text{Observated}-\max}$ values ranging from 1.04 to 1.63. The Fourier spectrum frequencies recorded by numerical simulation and field test are mainly concentrated in the range of 1~40 Hz, but the difference between the main frequencies recorded by the two is large. The main frequency of the energy spectrum recorded by the numerical simulation is around 15 Hz, which is the same as the main frequency of the energy spectrum vibration of the input vibration wave, and the main frequency of the energy spectrum vibration recorded by the field test is around 25 Hz.

1. Introduction

There are various complex topographical features along the high-speed railroad line, and the dynamic response of different topographical features under the high-speed train load is not the same. In recent years, with the growth of the urban population and people's travelling needs are also getting bigger and bigger, so that the contradiction between the production and life of people and the increasing demand for transport is becoming more and more prominent. On the one hand, due to the factors of safety, economy, and comfort of high-speed train operation, it becomes the primary tool for people to travel; on the other hand, the vibration problem caused by high-speed trains is becoming more and more serious, causing the vibration of buildings along the line and generating a lot of noise, which seriously affects the normal life of residents along the line. In addition, the environmental vibration caused by high-speed trains is closely related to the nature of the soil of the site, the form of the railroad section, the running speed of the train, and the grouping of the train.

During the past decades, many researches have been carried out to unravel the vibration problems. These studies mainly can be divided into three categories: theoretical analysis [1–6], numerical simulation, and field test. However, field test and numerical calculation are the most common and important methods to study vibration. Regarding the numerical simulation, the finite element (FE) numerical simulation is a very effective method to predict and analyze the track-subgrade behavior and the ground vibration induced by train loads. Xia et al. [7] studied the vibration of ground and buildings caused by train operation under elevated bridges through field tests and found that the vibration intensity had a significant relationship with the train speed, and the ground vibration was amplified in a certain range. Gao et al. [8] studied the vibration of the

ground along the Qin-Shen railroad using field testing techniques and discussed the effect of train grouping and speed on vibration. Chen et al. [9] tested and studied the vibration characteristics of the ground in a section of the Beijing–Guangzhou railway and its attenuation law. Guoyuan et al. [10, 11] analyzed the vibration characteristics and found that the graded gravel section could significantly reduce the settlement based on the vibration and settlement field test results of railroad road bridges and road culverts. Zhang [12] tested the vibration caused by the train operation under the viaduct and analyzed the vibration isolation effect of the barrier. Xiao et al. [13] tested and analyzed the vibration caused by train operation in the tunnel in three directions and found that the vibration in the vertical direction is smaller than that in the circular and radial directions, and there is a vibration amplification zone within a certain distance from the center of the tunnel. Zhang [14] and Gong-qi [15] studied the vibration generated by train operation in the embankment section using field measurements and numerical simulations. Xiang-Lian and Zhou [16] studied the vibration of the site during the passage of trains along the West-Bao railroad through field actual measurements and found that the vibration in each direction of vibration increases with the increase of train speed and axle weight, and there is a vibration amplification in a certain range. Wu et al. [17, 18] studied the vibration characteristics of the permafrost area under train load and the deformation characteristics of the soil under repeated train load and found that the vibration would attenuate substantially when passing through the embankment, and the deformation of the soil would reach the maximum in the first year of train operation and finally stabilize. Wang et al. [19] tested the vibration caused by train operation in different seasons of the roadbed section in the seasonal permafrost area, and found that the vibration of the site in winter is due to the soil is in the frozen state, the modulus of elasticity of the soil increases, and the damping ratio decreases, and the peak vibration acceleration of each component is larger, but in the spring thawing season, the soil contains a large amount of water, which results in the vibration acceleration of the peak of the vibration in all directions is a phenomenon of decreasing. The peak acceleration in the horizontal direction is slightly enhanced. Chen and Zhou [20] established the 3D FEM of the vehicle-track-subgrade coupling systems to study the different stiffness effects of the subgrade surface layer, bottom layer, embankment, foundation, and fastener by analyzing the vertical displacement of the track-subgrade. Connolly et al. [21, 22] established a three-dimensional numerical model to study the vibration characteristics of embankment in the soft soil regions under train loads. Degrande et al. [23] presented a three-dimensional FEM of tunnel soil to predict the vibrations in the free field from excitation. Andersen and Jones [24] compared the 2D and 3D FEM of railway tunnels. These results showed that the 2D soil-tunnel FEM could effectively calculate the dynamic response of soil and tunnels. Lyratzakis et al. [25] established a 3D FEM to analyze the influence of HST-induced vibration on the adjacent buildings and applied the efficient measure to minimize the vibration. Bian et al. [26] calculated the dynamic response of soil-induced train loads by using 2.5D FEM and analyzed the effects of track irregularity on ground vibration. Alves Costa et al. [27, 28] established a 2.5D FEM-BEM model of roadbed-soil structure, considering the train-track dynamic interaction, and validated the correctness of the model by the field vibration tests. Villalba Sanchis et al. [29] studied the dynamic responses of a dual gauge track induced by the train passage by experimental and numerical investigations. In order to accurately analyze vibration characteristics and site effects of loess hills under the moving load of a high-speed train, Yan et al. [30] established four types of loess hill models under railway viaduct by the finite element analysis software by field test, the dynamic response and stability of loess hills under two different vibration sources under high-speed train load were studied by using two-dimensional equivalent linear response time history analysis, and the influence of the mechanical parameters of loess on the vibration of different types of loess hill was analyzed.

From the above studies, it can be seen that the research on vibration caused by train operation is mainly focused on flat sites in soft soil, permafrost, and loess areas, and there is less research on the vibration characteristics of complex terrain landforms along railroad lines. The role of topography has been considered by scholars in the field of earthquake engineering [31, 32], and it is found that topography makes the vibration propagation characteristics significantly different from those of a flat site. However, there are significant differences between the characteristics of vibrations caused by high-speed trains and ground vibrations in the time and frequency domains. The Bao-Lan high-speed railway is the main component of the "eight horizontal and eight vertical" high-speed passenger transportation network in China, and one-third of the total length of the railroad is located in the Tianli basin, where the loess layer thickness is large, the wetness level is high, and there are complex topographical features such as tableland, beam, and hill [33].

Due to the very complex geomorphology of the Loess Plateau, there are not only roadbeds but also a large number of bridges and tunnels along the railroad line. Meanwhile, quite a number of previous studies did not consider the effects of different sites and landforms on vibration propagation. In order to accurately analyze the vibration characteristics of loess hilly sites under high-speed train operating loads and their site effects, a series of field vibration tests were conducted in this work based on the site test profiles, and a finite element (FE) model of loess hilly sites under high-speed railroad viaducts was established. The two-dimensional equivalent linear response time dynamic analysis method is used to study and analyze the dynamic response of the loess hilly site under the vibration source of the train operating load and its stability under the high-speed train load. The vibration propagation characteristics, attenuation law, and spectral characteristics of the loess hilly site from the field test and numerical simulation are compared and analyzed, and the vibration characteristics of the bridge piers and surrounding sites along the Baolan high-speed railroad are studied. The study is of great help to the stability and safety prediction of railroad projects in loess areas.

2. Field Testing

2.1. Testing Instruments. The ground vibration test instrument used is an 891-II type vibration meter (Figure 1), which is developed by the Institute of Engineering Mechanics of China Earthquake Bureau and can be used to test ground vibration, pulsation or vibration of building structures, and engineering vibration. The vibrometer is mainly composed of a geophone and a SysCom data acquisition system, which mainly includes amplifiers, recorders, filters, and data acquisition instruments. This instrument has the characteristics of small size, lightweight, easy to carry and use, and large test range. The acceleration test range of this instrument is 0~2.0 g, the sampling interval is 0.005 s, and the recording length of this instrument is 5 s before the excitation and 35 s after the excitation.

In this test, the X direction is specified as the direction of train operation, the Y direction is perpendicular to the line direction, and the Z direction is the direction of gravity.

Figure 1: 891-II vibration meter.

2.2. Loess Hill Site Environment and Measurement Point Layout. The test site is located under an elevated bridge of Qin'an-Tongwei on the Baolan passenger dedicated line, with a bridge height of about 20 m. One side of the bridge is a flat terrain, while the other side is a typical rectangular loess hill terrain. In the vertical direction of the high-speed railway bridge at a distance of 41 m on the side of the rectangular loess hills were arranged with a total of six measurement points, of which measurement point 1 was arranged at a distance of 2 m from the bridge abutment, measurement point 2 was arranged at a distance of 9 m from the bridge abutment, measurement point 3 was arranged at a distance of 18 m from the bridge abutment, measurement point 4 was arranged at a distance of 27 m from the bridge abutment, and measurement points 5 and 6 were arranged on the loess hill site, which was 30 m and 41 m away from the bridge abutment, respectively. The width of the loess hill site was 11 m. The height was 4.5 m. The measurement point layout and the shape of loess hill are shown in Figure 2.

3. Numerical Simulation

3.1. Numerical Simulation Methods: Finite Element and Infinite Element Coupled Analysis Methods

3.1.1. Finite Element Analysis Methods. The finite element unit method is an essential tool for engineering structural analysis and large-scale numerical calculations, and the emergence of the finite element method is an important breakthrough in the field of numerical calculations. The basic method is to divide the finite area into a finite number of units, establish algebraic control equations on each unit and solve them, and then connect these divided units in a certain way, and the format of the divided units can be various shapes, so it can be used to solve the calculation of complex models.

Dynamic analysis is different from statics, when the building structure receives a load, and the magnitude and direction of the load are related to time, which requires that not only the magnitude of the inertia force but also the influence of damping should be considered in the dynamic analysis. At present, two methods can be used for solving dynamics problems, which are explicit and implicit solutions.

In order to understand the dynamic characteristics of a structure, such as a building, during the whole vibration process, it is necessary to use the time course analysis method to solve the problem. The time course analysis method is used to solve the differential equations of motion of the object by numerical methods of stepwise integration and finally to find out the motion of the structure and building during the whole vibration process.

3.1.2. Infinite Element Analysis Method. In geotechnical engineering, the community foundation is actually a semi-infinite space structure, which should be considered as infinite when calculating and analyzing. However, in the dynamic analysis of geotechnical engineering, it is generally only concerned with the vibration in and around the building structures and does not need to be considered infinitely far away, so it is reduced to a near-field fluctuation problem.

In the numerical calculation model, it is impossible to build the foundation as an infinite area, and it is necessary to truncate it, but on the truncated boundary, the vibration wave will have an obvious bouncing effect, which is obviously not consistent with the actual situation, resulting in errors in the results of numerical calculation. In order to solve this problem, ABAQUS provides a new method, namely, infinite elements to meet the needs of the calculation. The definition of an infinite element in ABAQUS can only be rewritten by inp file, and the unit name of the infinite element contains "IN."

3.2. Site Model and Soil Parameters of Loess Hill Site under Viaduct of High-Speed Railroad. In order to study the influence of rectangular loess hill site and soil mechanical parameters on vibration propagation under the elevated bridge, and the vibration characteristics of different forms of loess hill site, a rectangular loess hill model consistent with the site was established according to the field measurement profile: the length of the rectangular loess hill is 11 m.

The length of the rectangular loess hill is 11 m, and the width is 4.5 m, as shown in Figure 3. The model is divided into two parts, the first part is the bridge pier and pile

(a)

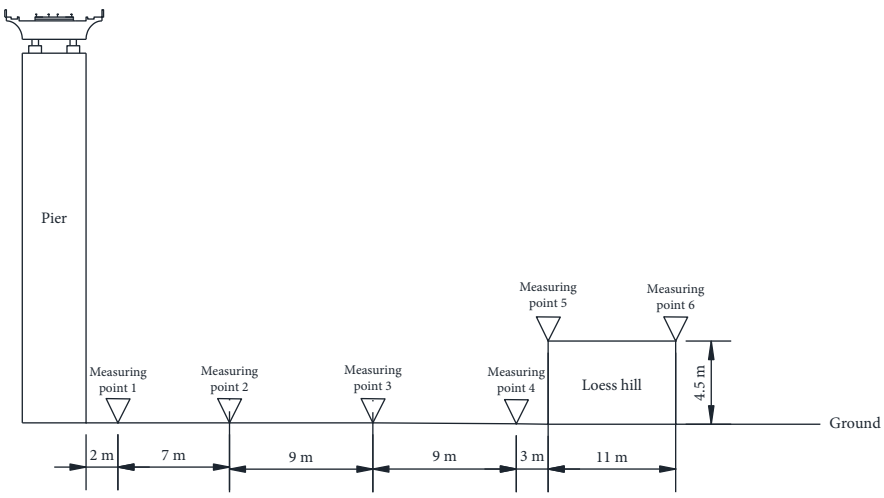

(b)

Figure 2: Schematic diagram of site and measuring points of rectangular loess hill site under the railway viaduct. (a) Field layout of vibration measuring points at the loess hill site under the railway viaduct. (b) Layout diagram of vibration measuring points at the loess hill site under the railway viaduct.

foundation, the pier height is 20 m, the width is 4 m, using bored piles and two pile foundations, and pile length is 8 m, using C30 concrete; the second part is the loess body because the acceleration and displacement of the foundation vibration caused by the train are usually small, the soil body is considered elastic, its physical and mechanical parameters are shown in Table 1 [34], and the thickness of the loess is 40 m. The left and right boundaries of loess body model are used as infinite element boundaries in order to prevent the reflection effect of waves.

In order to compare with the field test data, a total of six measurement points are arranged on the side of the rectangular loess hill under the bridge of the model structure, all of which are consistent with the location of the field test points: measurement point 1 is arranged 2 m from the bottom of the bridge pier, measurement point 2 is 9 m from the bottom of the bridge pier, measurement point 3 is 18 m from the bottom of the bridge pier, measurement point 4 is 27 m from the bottom of the bridge pier, measurement point 5 is arranged on the left side of the rectangular loess hill, and the horizontal distance of measurement point 4 is 3 m. The width of the loess hill is 11 m, the height is 4.5 m, and the measurement point 6 is arranged on the right side of the rectangular loess hill, which is 41 m from the bottom of the bridge pier, as shown in Figure 3. The finite element grid cell size is $1\,\mathrm{m} \times 0.5\,\mathrm{m}$, total of 7639 grids.

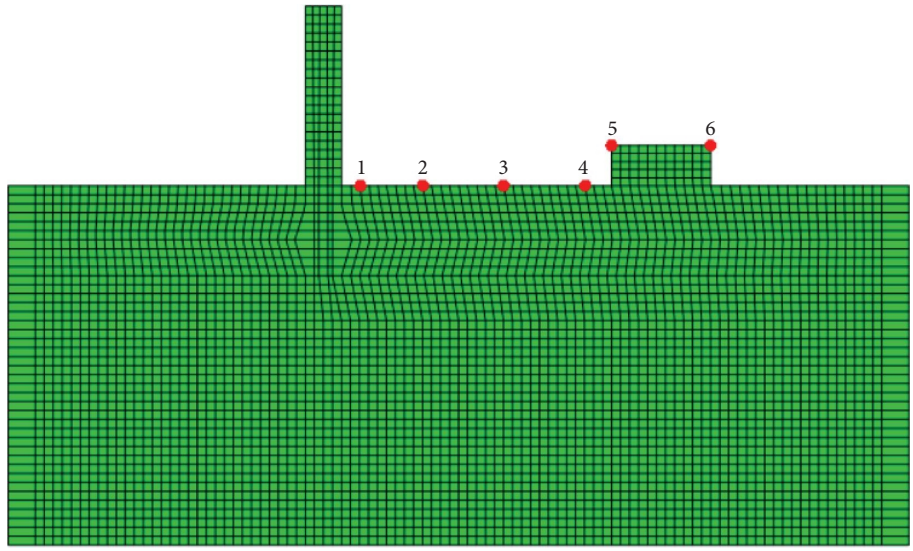

Figure 3: Model of loess hill site.

Table 1: Parameters of the soil layer in the loess site.

Soil layer no.	Soil layer type	Thickness (m)	Depth (m)	Density (kg/m^3)	Modulus of elasticity (MPa)	Poisson's ratio
1	Loess	5.0	5.0	1550	50.22	0.30
2	Loess	5.0	10.0	1600	64.00	0.30
3	Loess	5.0	15.0	1630	86.23	0.30
4	Loess	5.0	20.0	1650	129.36	0.30
5	Loess	5.0	25.0	1680	151.20	0.30
6	Loess	5.0	30.0	1700	182.95	0.30
7	Loess	10.0	40.0	1700	208.25	0.30

3.3. Model Vibration Load. Figure 4(a) shows the vibration waveform of the vertical direction (z-component) at the location of the abutment bearing platform recorded by the vibration test during the passage of a 16-section train with a speed of 240 km/h of the Baolan high-speed railroad, which is the vibration load applied by the numerical calculation. Before application, high-pass filtering and baseline correction were performed by Seismosignal software to filter out the components of seismic waves with frequencies less than 0.1 Hz. The vibration duration used for the calculation is 10.00 s, and the maximum peak acceleration is 51.27 cm^2/s. Figure 4(b) shows the vibration Fourier spectrum characteristics, and the vibration duration applied for the calculation is dominated by the medium and high-frequency components, and the excellence frequency is 15 Hz. Figure 4(c) shows the vibration energy spectrum curve with a remarkable frequency of 15 Hz.

3.4. Stability Analysis of the Rectangular Loess Hill Site under the Viaduct. Since the loess hill site and its surrounding sites are mainly subject to the action of gravity under natural conditions, their stability is mainly controlled by gravity, while the construction of the railroad viaduct in its vicinity is subject to the coupled action of gravity and train load due to the influence of train operation. Therefore, in order to further analyze the characteristics of the loess hill site elevated under the coupling action of train load and gravity, the maximum vertical displacement clouds under the action of train load and gravity, and the Mises stress clouds under the coupling action of train load and gravity were compared and analyzed, as shown in Figures 5 and 6.

As can be seen from Figure 5, the vertical maximum displacement clouds under gravity load are significantly different from those under train load. Under gravity, the vertical displacement under the viaduct is larger, and the maximum vertical displacement decreases with the increase of depth and distance from the bottom of the bridge pier; while the vertical displacement of the loess hill is the largest, and again, the maximum vertical displacement is decaying with the increase of depth and distance from the loess hill. Also, under the action of train load, the vertical displacement only occurs around the bridge pier and has no effect on the vertical displacement of the loess hill basically.

As can be seen from Figure 6, there is basically no difference between the Mises stress clouds under gravity and under the coupling of train load and gravity, except that under the coupling of train load and gravity, there is a significant increase in the Mises stress applied to the pile foundation and its bottom soil.

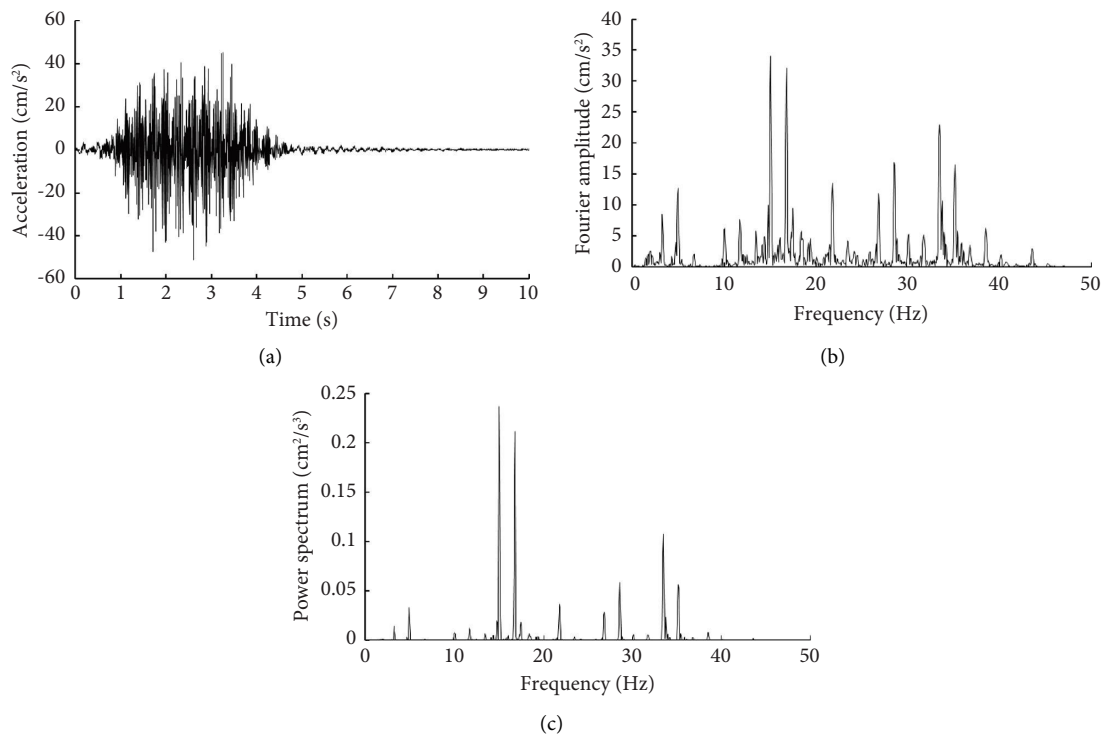

Figure 4: Numerical calculation of the input vibration acceleration time range and its spectrum curve.

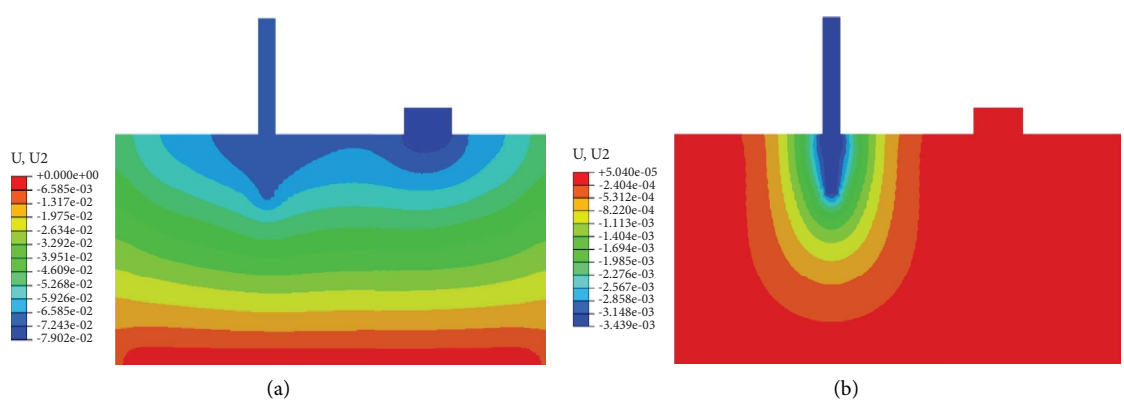

Figure 5: Comparison of maximum displacement clouds. (a) The vertical maximum displacement cloud of the loess hill site under the viaduct under gravity load. (b) The vertical maximum displacement cloud of the loess hill site under the viaduct under the high-speed train load.

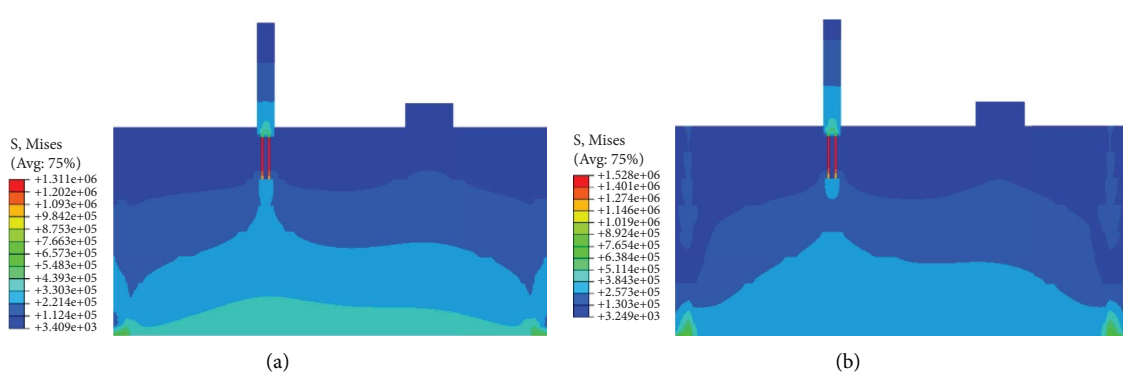

Figure 6: Mises comparison of stress clouds. (a) Mises stress clouds of the rectangular loess hill site under the viaduct under gravity load. (b) Mises stress clouds of the rectangular loess hill site under the viaduct with coupled gravity and train loads.

3.5. Numerical Simulation Acceleration Clouds. Figures 7 and 8 show the vibration acceleration clouds of the loess site under the same viaduct at different moments, respectively. From the figures, it can be seen that the vibration acceleration distribution clouds of the loess hill site at different moments (6.68 s and 6.89 s) are similar, and the vibration acceleration all gradually decreases with the increase of the vibration source distance, but the acceleration all shows a significant increase on the loess hill site.

4. Comparison Analysis of Field Test and Numerical Simulation Results

4.1. Acceleration Time Range. Figure 9 shows the vertical (z-component) vibration acceleration time course of each observation point 1 to 6 in the loess site under the viaduct during the passage of a 16-section train with a speed of 242 km/h of the high-speed railroad, and it can be seen that the ground vibration acceleration waveform of each observation point in the loess site has similarity, and there is good symmetry above and below the vibration acceleration time course curve of each measurement point, and there are obvious periodic peaks, and the vibration in the loess hill. The amplification effect is very obvious.

As can be seen from the figure, the peak vibration accelerations of measurement points 1 to 6 recorded in the field test are 18.74 cm/s^2, 12.24 cm/s^2, 9.67 cm/s^2, 8.56 cm/s^2, 11.26 cm/s^2, and 12.81 cm/s^2, respectively, and the peak vibration accelerations of measurement points 1 to 6 recorded in the numerical simulation are 19.49 cm/s^2, 15.46 cm/s^2, 15.73 cm/s^2, 10.94 cm/s^2, 13.03 cm/s^2, and 14.89 cm/s^2, respectively, and it is obvious that the peak vibration acceleration of measurement points 1~4 decays with distance as they are farther away from the bridge pier, while on the rectangular loess hill due to the influence of site conditions, which makes the peak vibration acceleration of measurement point 5 and measurement point 6 appear "rebound increase", the data recorded in the field test are 1.32 times and 1.49 times magnified, respectively, compared to measurement point 4, and the data recorded in the numerical simulation are 1.19 times and 1.36 times magnified, respectively, compared to measurement point 4. At the same time, the vibration durations of measurement points 1 to 4 recorded in the field test were all 7.5 s, while the vibration durations of measurement points 5 and 6 were both 8.81 s. Both showed an increase in vibration duration, which were amplified by 1.17 times compared with the first four measurement points.

Figure 10 shows the peak vertical (z-component) vibration acceleration curves, amplification coefficients, and $a_{\text{Simulated-max}}/a_{\text{Observated-max}}$ values for each observation point 1 to 6 at the loess site under the viaduct during high-speed railroad train operation recorded by field tests and numerical simulations. From the figure, it can be seen that the peak vibration acceleration of measurement points 1 to 4 recorded by both field test and numerical simulation decayed linearly with distance, while measurement point 5 and measurement point 6 showed amplification phenomenon, and the overall peak value of numerical simulation was larger than that of field test (Figure 10(a)). Figure10(b) shows the amplification factor obtained from the ratio of the peak acceleration at each measurement point to the peak acceleration at measurement point 1 in the field test. Figure 10(b) shows the amplification coefficient of the peak acceleration of each measurement point and the amplification coefficient of the peak acceleration of measurement point 1, $a_{\text{Simulated-max}}/a_{\text{Observated-max}}$ values range from 1.04 to 1.63, with the largest dispersion at measurement point 3, and $a_{\text{Simulated-max}}/a_{\text{Observated-max}}$ values at the other five measurement points range from 1.04 to 1.28. This indicates that there is still some error between the numerically simulated soil parameters and the real soil parameters.

4.2. Spectrum Analysis

4.2.1. Spectrum Analysis Method of Strong Vibration. Spectral analysis of data from strong vibration observations is actually a process of Fourier transform and Fourier inverse transform. The value of N (even) of the time function at equal time interval points $x_m\,(m = 0,1,2,\ldots,N-1)$:

$$A_k = \frac{2}{N}\sum_{m=0}^{N-1} x_m \cos\frac{2\pi \mathrm{km}}{N} k = 0,1,2,\ldots,\frac{N}{2}-1,\frac{N}{2}$$
$$B_k = \frac{2}{N}\sum_{m=0}^{N-1} x_m \sin\frac{2\pi \mathrm{km}}{N} k = 1,2,\ldots,\frac{N}{2}-1, \tag{1}$$

where x_m is denoted as a finite trigonometric function with A_k and B_k as coefficients.

$$x_m = \frac{A_0}{2} + \sum_{k=1}^{N/2-1}\left[A_k \cos\frac{2\pi \mathrm{km}}{N} + B_k \sin\frac{2\pi \mathrm{km}}{N}\right] + \frac{A_{N/2}}{2}\cos\frac{2\pi(N/2)m}{N}. \tag{2}$$

Considering that this function is nothing but an approximation of the metric function x_t.

$$\tilde{x}(t) = \frac{A_0}{2} + \sum_{k=1}^{N/2-1}\left[A_k \cos\frac{2\pi \mathrm{kt}}{N\Delta t} + B_k \sin\frac{2\pi \mathrm{kt}}{N\Delta t}\right] + \frac{A_{N/2}}{2}\cos\frac{2\pi(N/2)t}{N\Delta t}. \tag{3}$$

Equation (3) is a finite Fourier approximation of the function x_t. The coefficients A_k and B_k in equation (1) are of finite Fourier coefficients. The calculation of equation (1) is called the Fourier transform of the discrete value x_m, and the calculation of equation (2) is called the Fourier inverse transform.

Here, the introduction of the complex Fourier coefficients C_k is

$$x_m = \sum_{k=0}^{N-1} C_k e^{i(2\pi \mathrm{km})} \quad m = 0,1,2,\ldots,N-1. \tag{4}$$

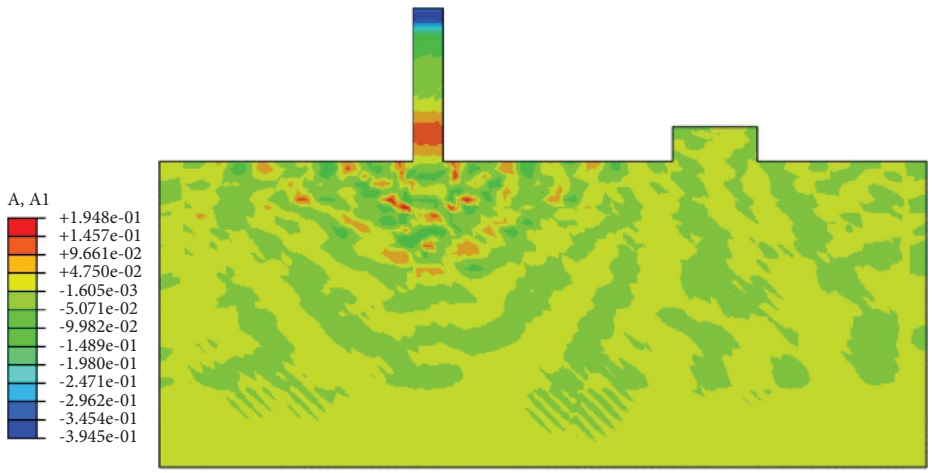

Figure 7: Acceleration clouds of the loess site under the viaduct at $t = 6.68$ s.

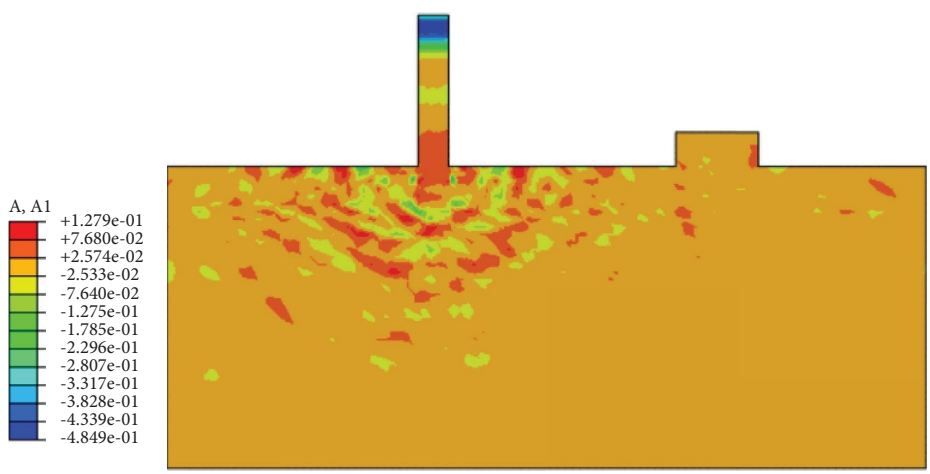

Figure 8: Acceleration clouds of the loess site under the viaduct at $t = 6.89$ s.

In a more concise way, it can be expressed as the following equation, called the finite complex Fourier series,

$$C_k = \frac{1}{N}\sum_{m=0}^{N-1} x_m e^{-i(2\pi \mathrm{km}/N)} \quad k = 0,1,2,\ldots,N-1. \tag{5}$$

Equation (4) is the Fourier transform, and equation (5) is the inverse Fourier transform. Using the above calculation method, the observed data can be subjected to spectral analysis.

4.2.2. Fourier Spectrum. From Figure 11, it can be seen that the Fourier spectrum waveforms of each measurement point recorded by numerical simulation and field test have similarity and have obvious periodic peaks, the amplification of vibration in the loess hill is very obvious, and the overall amplitude and peak acceleration are similar to the linear decay with distance, and the amplification phenomenon is presented at measurement point 5 and measurement point 6. The Fourier spectrum frequencies recorded by numerical simulation and field test are mainly concentrated in 1~40 Hz when the train with the speed of 240 km/h passes by, but the difference between the main frequencies recorded by the two is large, and the main frequency of Fourier spectrum vibration recorded by numerical simulation is around 15 Hz, which is the same as the main frequency of Fourier spectrum vibration of the input vibration wave, while the main frequency of Fourier spectrum vibration recorded by field test is around 25 Hz. The Fourier spectrum amplitude recorded by numerical simulation of the same measurement point is larger than the amplitude recorded by the field test, and the Fourier spectrum frequency range of measurement points 3~6 recorded by the field test is larger between 1 and 45 Hz, while the Fourier spectrum frequency range of measurement points 3~6 recorded by numerical simulation is between 1 and 25 Hz.

From Figure 12, it can be seen that the Fourier spectrum amplitudes of measurement points 1 to 6 recorded in the field test are 11.95 cm/s^2, 7.68 cm/s^2, 6.23 cm/s^2, 6.75 cm/s^2, 8.45 cm/s^2, and 9.62 cm/s^2, respectively, and the Fourier spectrum amplitudes of measurement points 1 to 6 recorded in the numerical simulation are 13.82 cm/s^2, 20.53 cm/s^2, 22.64 cm/s^2, 13.95 cm/s^2, 16.53 cm/s^2, and 16.83 cm/s^2, respectively, and it is obvious that the Fourier spectrum

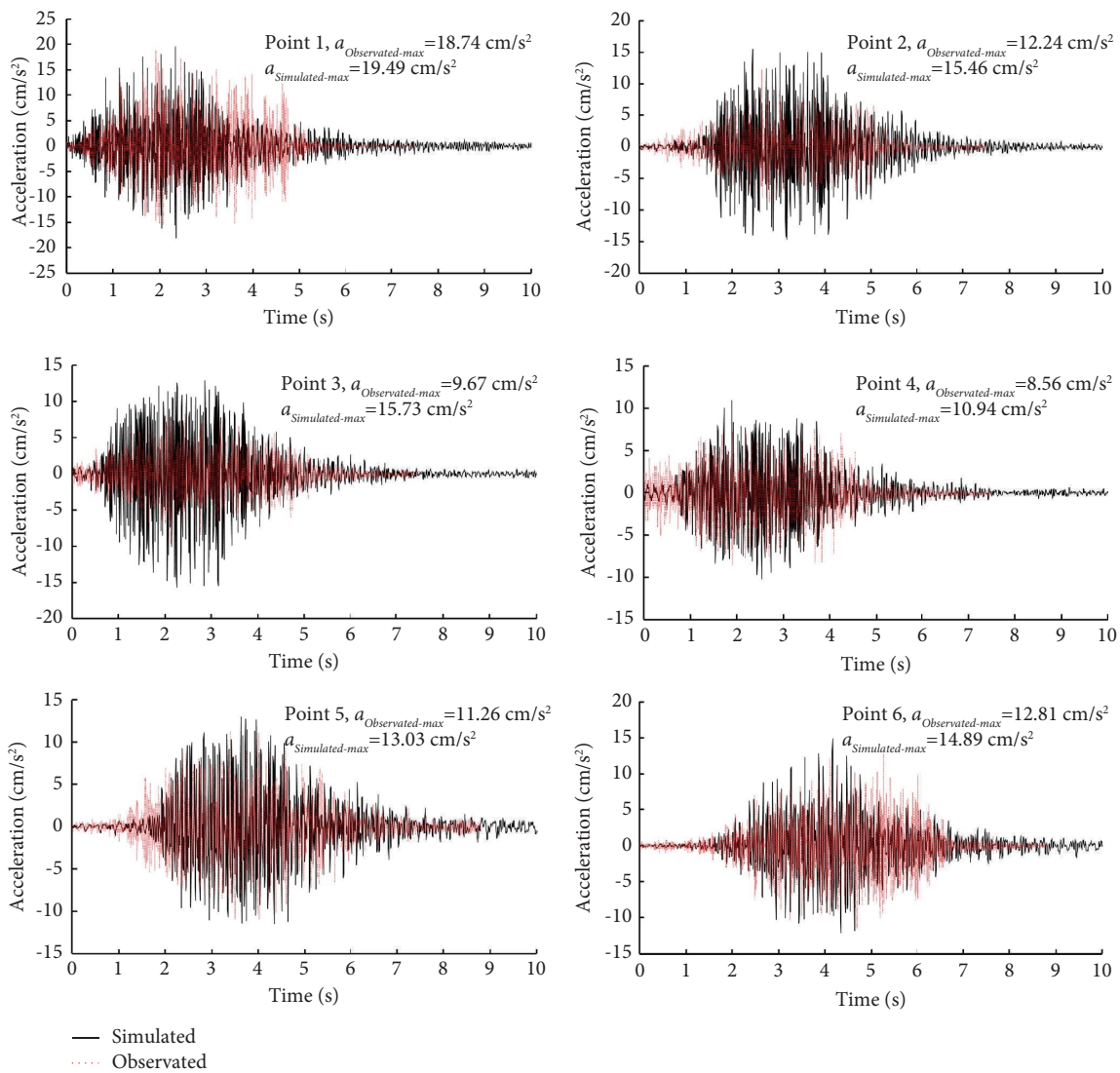

Figure 9: Time course of vertical vibration acceleration for each observation point in field test and numerical simulation.

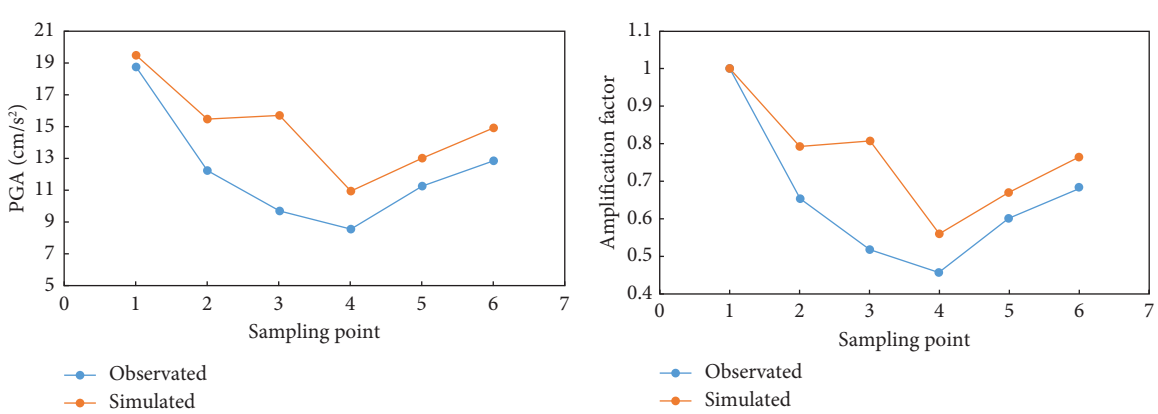

(a) (b)

Figure 10: Continued.

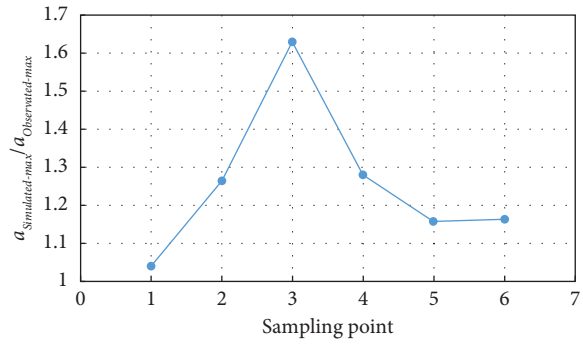

(c)

Figure 10: Comparison of acceleration peak at each measurement point between field test and numerical simulation.

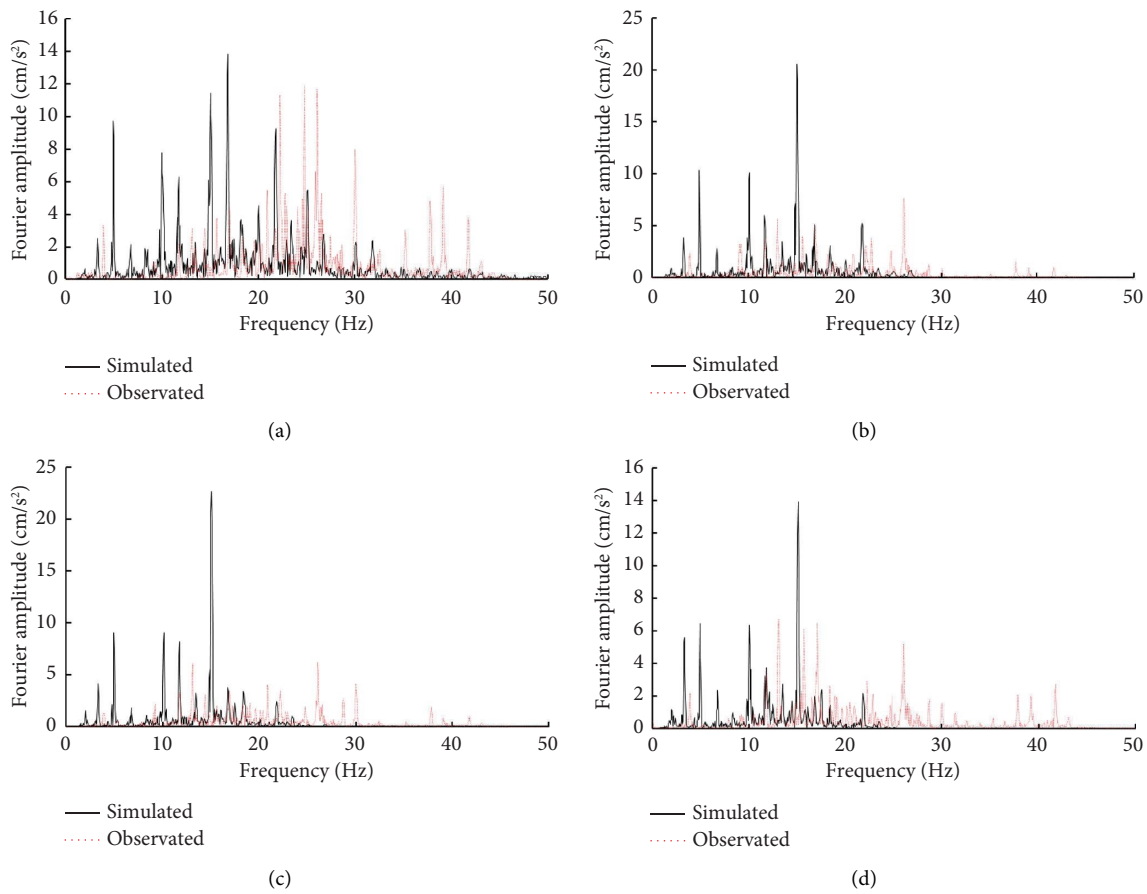

Figure 11: Continued.

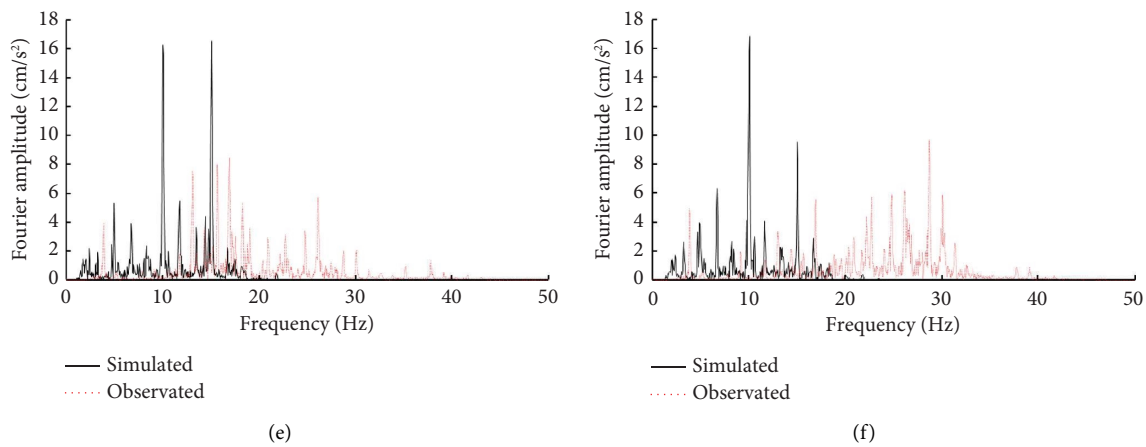

Figure 11: Fourier spectrum of each measurement point for field test and numerical simulation. (a) Point 1. (b) Point 2. (c) Point 3. (d) Point 4. (e) Point 5. (f) Point 6.

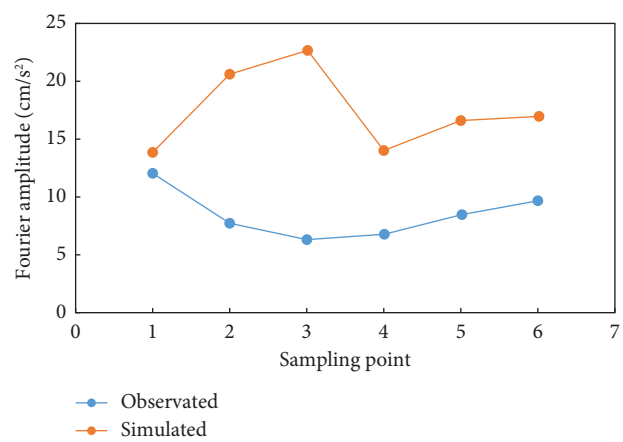

Figure 12: Comparison of Fourier spectrum amplitude at each measurement point between field test and numerical simulation.

amplitudes of measurement points 1~4 decay with distance as they are farther away from the piers, while on the rectangular loess hill due to the influence of site conditions, making the Fourier spectrum amplitudes of measurement point 5 and measurement point 6 appear "rebound increase," the data recorded in the field test are amplified 1.25 times and 1.43 times compared to measurement point 4, and the data recorded in the numerical simulation are amplified 1.19 times and 1.21 times compared to measurement point 4.

4.2.3. Energy Spectrum. The vibration acceleration energy spectrum reflects the distribution of vibration acceleration energy at individual frequencies, and the relationship between the acceleration energy spectrum function $G(\omega)$ and the spectrum function $f(j\omega)$ can be expressed as follows [35]:

$$G(\omega) = |f(j\omega)|^2. \tag{6}$$

In order to further analyze the relationship between the vibration characteristics of each measurement point and the distance from the vibration source, the vibration acceleration signals of each measurement point recorded by numerical simulation and field test were analyzed by energy spectrum, as shown in Figures 13 and 14.

From Figure 13, it can be seen that the energy spectrum waveforms of each measurement point recorded by numerical simulation and field test have similarities and have obvious periodic peaks. When a train with an hourly speed of 240 km/h passes by, the frequencies of the energy spectrum recorded by the numerical simulation and the field test are mainly concentrated in the range of 1~40 Hz, but the difference between the main frequencies recorded by the two is large. The amplitude of the energy spectrum recorded by the numerical simulation is larger than that recorded by the field test, and the frequency range of the energy spectrum of measurement points 3~6 recorded by the field test is larger between 1 and 30 Hz, while the frequency range of the Fourier spectrum of measurement points 3~6 recorded by the numerical simulation is between 1 and 20 Hz.

As can be seen from Figure 14, the energy spectrum amplitudes of measurement points 1 to 6 recorded in the field test are 0.17 cm^2/s^3, 0.26 cm^2/s^3, 0.18 cm^2/s^3, 0.19 cm^2/s^3, 0.19 cm^2/s^3, and 0.21 cm^2/s^3, respectively, and the energy

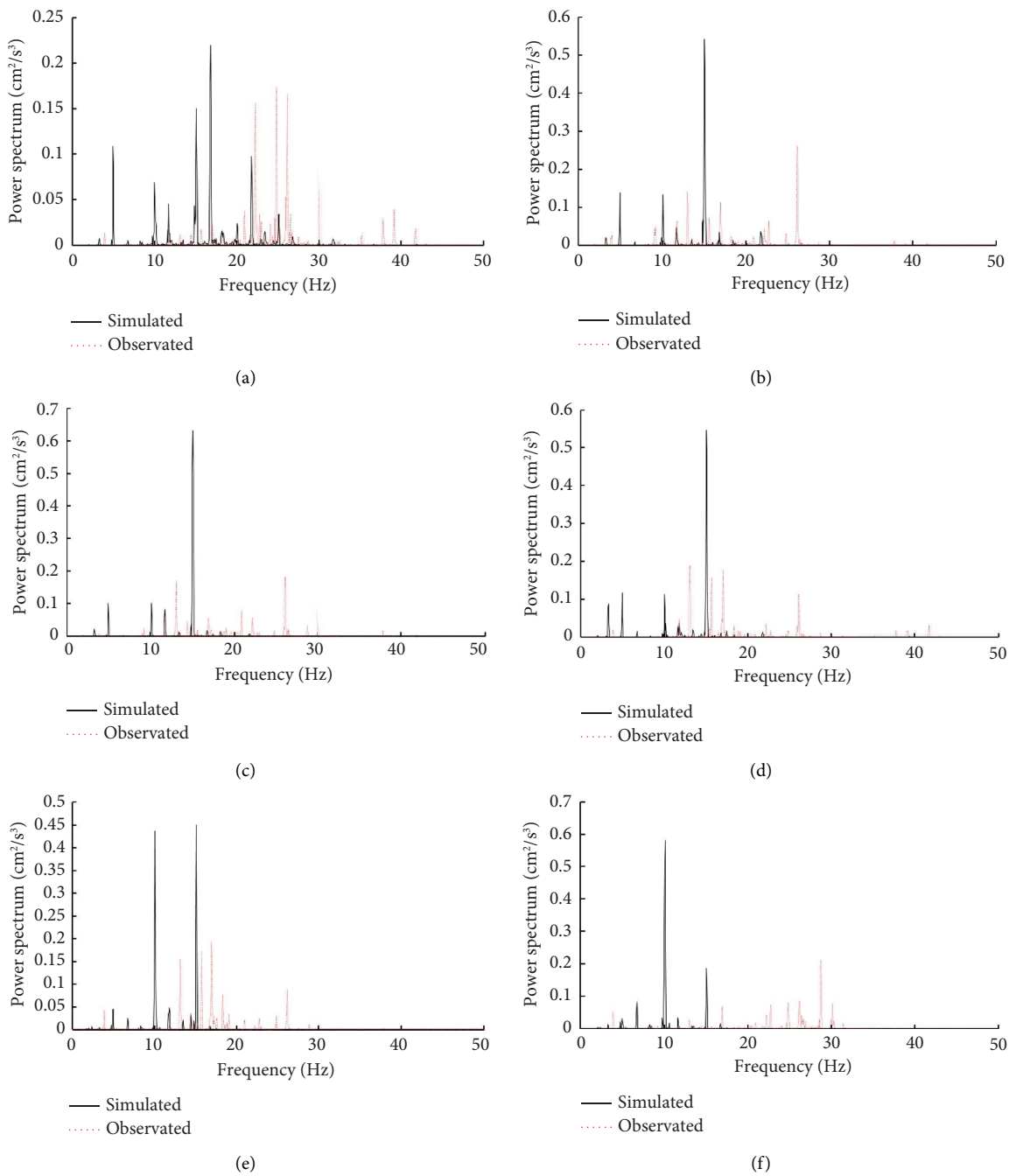

Figure 13: Energy spectrum of each measurement point from field test and numerical simulation. (a) Point 1. (b) Point 2. (c) Point 3. (d) Point 4. (e) Point 5. (f) Point 6.

spectrum amplitudes of measurement points 1 to 6 recorded in the numerical simulation is $0.22\,cm^2/s^3$, $0.54\,cm^2/s^3$, $0.63\,cm^2/s^3$, $0.55\,cm^2/s^3$, $0.45\,cm^2/s^3$, and $0.58\,cm^2/s^3$, and the energy spectra of measurement point 1 are the smallest, the data recorded in the field test are 1.11 times larger than that of measurement point 4, and the data recorded in the numerical simulation are 1.05 times larger than that of measurement point 4.

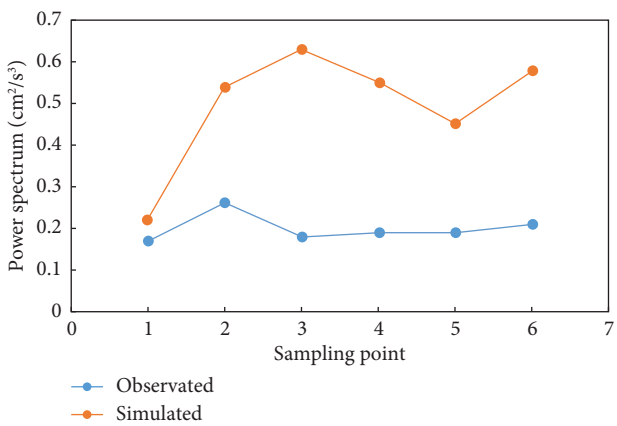

Figure 14: Comparison of energy spectrum amplitude at each measurement point between field test and numerical simulation.

5. Conclusion

Through the field vibration test and numerical simulation of the loess hill site during the passage of the train of the Baolan high-speed railway, the following conclusions were obtained based on the comparative analysis and research in both time and frequency domains:

(1) The vertical maximum displacement clouds under the action of gravity load and train load are obviously different. Under the action of gravity, the vertical displacement under the elevated bridge is larger, and the maximum vertical displacement decreases with the increase of depth and distance from the bottom of the bridge pier while the vertical displacement of the loess hill is the largest, and again, the maximum vertical displacement is decaying with the increase of depth and distance from the loess hill. Also, under the action of train load, the vertical displacement only occurs around the bridge pier and has no effect on the vertical displacement of the loess hill basically. There is basically no difference between the Mises stress clouds under gravity and the coupled train load and gravity, except that the Mises stress on the pile foundation and its bottom soil increases significantly under the coupled train load and gravity.

(2) The vibration acceleration distribution clouds of the loess hill site at different moments are similar, and the vibration acceleration all gradually decreases with the increasing distance of the vibration source, but the acceleration on the loess hill all shows a significant increase. The waveform of ground vibration acceleration at each observation point of the loess site has similarity, and there is good symmetry above and below the time course curve of vibration acceleration at each measurement point, there is an obvious periodic peak, and the vibration amplification in the loess hill is very obvious, and the ratio of peak acceleration at each measurement point is recorded by numerical simulation and field test, the $a_{\text{Simulated-max}}/a_{\text{Observated-max}}$ values range from 1.04 to 1.63, with the largest dispersion at measurement point 3, and the $a_{\text{Simulated-max}}/a_{\text{Observated-max}}$ values at the other five measurement points range from 1.04 to 1.28, generally showing that the peak acceleration recorded by the numerical simulation is larger than that of the field test. The vibration durations of measurement points 1 to 4 recorded in the field test were all 7.5 s, while the vibration durations of measurement point 5 and measurement point 6 at the location of the loess hill site were both 8.81 s. Both showed an increase in vibration duration, which was 1.17 times larger than the previous four measurement points, respectively.

(3) When a high-speed train with a speed of 240 km/h passes through, the Fourier spectrum frequencies recorded by numerical simulation and field test are concentrated between 1 and 40 Hz, but the difference of the main frequency between the two records is large, the main frequency of Fourier spectrum vibration recorded by numerical simulation is 15 Hz, which is the same as that of the input vibration waveform, but the main frequency of Fourier spectrum vibration recorded by field test is 25 Hz; as the distance from the bridge abutment gets farther and farther away, the Fourier spectrum amplitude of the loess flat site in the non-loess hills gradually decays with the distance, whereas the Fourier spectrum amplitude is amplified in the loess hill site due to the site condition.

(4) When the train with the speed of 240 km/h passes by, the energy spectrum frequencies recorded by numerical simulation and field test are mainly concentrated in 1~40 Hz, but the difference between the main frequencies recorded by the two is large, the main frequency of energy spectrum vibration recorded by numerical simulation is around 15 Hz, which is the same as the main frequency of energy spectrum vibration of the input vibration wave, while the main frequency of energy spectrum vibration recorded by field test is around 25 Hz. The energy spectrum of measurement point 1 is the smallest, and the energy spectrum of measurement points 2~5 decays with distance as the distance from the bridge pier gets farther, but the energy spectrum of measurement point 6 has a "rebound increase," and the data recorded in the field test are 1.11 times larger than that of measurement point 4, and the data recorded in the numerical simulation are 1.05 times larger than that of measurement point 4.

(5) Through the comparative analysis of the results of the field vibration test and numerical calculation of the Baolan high-speed railway, it is found that the results obtained from the field vibration test and numerical calculation of the high-speed railway have high similarity, which can provide the corresponding basis for the theoretical analysis of the vibration effect of the loess site of train vibration, verify the

correctness and applicability of the theoretical model and numerical analysis model, and can evaluate the environmental vibration caused by the train and predict the train vibration. It can also provide a basis for the assessment of train-induced environmental vibration and the prediction of train vibration.

Data Availability

The data used to support the findings of the article are included within the article.

Conflicts of Interest

The authors declare that they have no conflicts of interest.

Acknowledgments

The authors acknowledge the financial support provided by the Scientific Research Fund of Institute of Earthquake Forecasting, China Earthquake Administration (Grant nos. 2022IESLZ03 and 2022IESLZ01), the Natural Science Foundation of Gansu Province (Grant no. 22JR5RA825), the Scientific Research Fund of the Institute of Engineering Mechanics, China Earthquake Administration (Grant no. 2020EEEVL0304), the Second Tibetan Plateau Scientific Expedition and Research Program (STEP) (Grant no. 2019QZKK0905), the National Natural Science Foundation of China (Grant nos. 42330704 and U1939209), and the Science for Earthquake Resilience Program of the China Earthquake Administration (Grant no. XH242808A).

References

[1] V. V. Krylov, "On the theory of railway-induced ground vibrations," *Journal de Physique IV*, vol. 4, no. 5, 1994.

[2] V. V. Krylov, A. R. Dawson, M. E. Heelis, and A. C. Collop, "Rail movement and ground waves caused by highspeed trains approaching track-soil critical velocities," *Proceedings of the Institution of Mechanical Engineers, Part F: Journal of Rail and Rapid Transit*, vol. 214, no. 2, pp. 107–116, 2000.

[3] X. Sheng, C. J. C. Jones, and D. J. Thompson, "A comparison of a theoretical model for quasi-statically and dynamically induced environmental vibration from trains with measurements," *Journal of Sound and Vibration*, vol. 267, no. 3, pp. 621–635, 2003.

[4] W. Zhai, K. Wang, and C. Cai, "Fundamentals of vehicle-track coupled dynamics," *Vehicle System Dynamics*, vol. 47, no. 11, pp. 1349–1376, 2009.

[5] Y. Cai, H. Sun, and C. Xu, "Steady state responses of poroelastic half-space soil medium to a moving rectangular load," *International Journal of Solids and Structures*, vol. 44, no. 22-23, pp. 7183–7196, 2007.

[6] X. Lei and B. Zhang, "Analysis of dynamic behavior for slab track of high-speed railway based on vehicle and track elements," *Journal of Transportation Engineering*, vol. 137, no. 4, pp. 227–240, 2011.

[7] H. Xia, N. Zhang, and C. A. O. Yan-mei, "Experimental study of train-induced vibrations of ground and nearby buildings," *Journal of the China Railway Society*, vol. 26, no. 4, pp. 93–98, 2004.

[8] G. Gao, L. I. Zhi-yi, and F. E. N. G. Shi-jin, "Experimental results and numerical predictions of ground vibration induced by high-speed train running on Qin-Shen railway," *Rock and Soil Mechanics*, vol. 28, no. 9, pp. 1817–1822, 2007.

[9] J. Chen, H. Xia, and J. Xiao, "Experimental study of ground vibrations induced by moving train," *Rock and Soil Mechanics*, vol. 29, no. 11, pp. 3113–3118, 2008.

[10] C. H. E. N. Guo-yuan, W. E. I. Li-min, and Y. A. N. G. Guo-lin, "Experimental study on dynamic characteristics of transition section of Hujiatun Zhongqiao road and bridge," *Journal of Vibration and Shock*, vol. 29, no. 6, pp. 184–188, 2010.

[11] C. H. E. N. Guo-yuan, Y. A. N. G. Guo-lin, and W. E. I. Li-min, "Experimental study on dynamic characteristics of transition section of railway passenger dedicated line culvert," *Journal of Railway Science and Engineering*, vol. 7, no. 1, pp. 47–51, 2010.

[12] L. Zhang, "Test and analysis of vibration induced by elevated railway and snti-vibration measure," *Journal of Railway Engineering Society*, vol. 29, no. 6, pp. 118–125, 2012.

[13] M. Q Xiao, J. Yao, and D. Huang, "Study and field measurement of environmental vibration induced by underground Guangzhou-Shenzhen-Hong Kong high speed rail in Shiziyang tunneL," *Chinese Journal of Rock Mechanics and Engineering*, vol. 23, pp. 3527–3534, 2013.

[14] G. Zhang, *Study on the Ground Vibration Induced by Trains Moving on Subgrade of High-Speed Railway*, Southwest Jiaotong University, Chengdu, China, 2014.

[15] C. H. E. N. Gong-qi, "Ground vibration analysis induced by high-speed train based on in-situ data," *Chinese Journal of Rock Mechanics and Engineering*, vol. 34, no. 3, pp. 601–611, 2015.

[16] M. E. N. G. Xiang-lian and F. J. Zhou, "Spatial analysis and study of roadbed vibration effect on loess area for Xi'an baoji high speed railway," *Journal of Railway Engineering Society*, vol. 34, no. 8, pp. 28–33, 2017.

[17] Z. Wu, T. Chen, and W. Ma, "The creep analysis of plain fill embankment at the permafrost regions along Qinghai-Tibet Railway under train dynamic load," *Rock and Soil Mechanics*, vol. 32, pp. 83–87, 2011.

[18] Z. Wu, T. Chen, and W. Ma, "Characteristics of load transmission of trains in permafrost regions along Qinghai-Tibet railroad," *Chinese Journal of Geotechnical Engineering*, vol. 35, no. Suppl.1, pp. 9–13, 2013.

[19] Z. Wang, L. I. N. G. Xian-chang, and H. U. I. Shu-qing, "Field monitoring of vibration response of subgrade in a seasonally frozen region," *Chinese Journal of Geotechnical Engineering*, vol. 37, no. 9, pp. 1591–1598, 2015.

[20] J. Chen and Y. Zhou, "Dynamic vertical displacement for ballastless track-subgrade system under high-speed train moving loads," *Soil Dynamics and Earthquake Engineering*, vol. 129, 2023.

[21] D. Connolly, A. Giannopoulos, and M. C. Forde, "Numerical modelling of ground borne vibrations from high speed rail lines on embankments," *Soil Dynamics and Earthquake Engineering*, vol. 46, pp. 13–19, 2013.

[22] D. P. Connolly, G. Kouroussis, O. Laghrouche, C. L. Ho, and M. C. Forde, "Benchmarking railway vibrations– track, vehicle, ground and building effects," *Construction and Building Materials*, vol. 92, pp. 64–81, 2015.

[23] G. Degrande, D. Clouteau, R. Othman et al., "A numerical model for ground-borne vibrations from underground railway traffic based on a periodic finite element-boundary

element formulation," *Journal of Sound and Vibration*, vol. 293, no. 3-5, pp. 645–666, 2006.

[24] L. Andersen and C. J. C. Jones, "Coupled boundary and finite element analysis of vibration from railway tunnels- a comparison of two- and three-dimensional models," *Journal of Sound and Vibration*, vol. 293, no. 3-5, pp. 611–625, 2006.

[25] A. Lyratzakis, Y. Tsompanakis, and P. N. Psarropoulos, "Efficient mitigation of highspeed train vibrations on adjacent reinforced concrete buildings," *Construction and Building Materials*, vol. 314, Article ID 125653, 2022.

[26] X. Bian, H. Jiang, C. Chang, J. Hu, and Y. Chen, "Track and ground vibrations generated by high-speed train running on ballastless railway with excitation of vertical track irregularities," *Soil Dynamics and Earthquake Engineering*, vol. 76, pp. 29–43, 2015.

[27] P. Alves Costa, R. Calçada, and A. Silva Cardoso, "Track-ground vibrations induced by railway traffic: in-situ measurements and validation of a 2.5D FEM-BEM model," *Soil Dynamics and Earthquake Engineering*, vol. 32, no. 1, pp. 111–128, 2012.

[28] P. A. Costa and R. Calcada, "Influence of ballast mats on the reduction of track-ground vibrations induced by railway traffic," *Types of Environmental Vibration Tests*, vol. 25, pp. 793–800, 2011.

[29] I. Villalba Sanchis, R. Insa Franco, P. Martínez Fernández, and P. Salvador Zuriaga, "Experimental and numerical investigations of dual gauge railway track behaviour," *Construction and Building Materials*, vol. 299, Article ID 123943, 2021.

[30] W. Yan, H. Zhang, H. Z. Zheng, Z. Wu, and X. X. Tian, "Numerical modelling of vibration response in loess hills due to a high-speed train on railway viaduct," *Research in Cold and Arid Regions*, vol. 14, no. 5, pp. 329–337, 2022.

[31] Y. Shi, "Blasting vibration effect of loess site," *Chinese Journal of Rock Mechanics and Engineering*, vol. 22, no. 11, pp. 1933–1938, 2003.

[32] Y. Shi, L. U. Yu-xia, and H. E. Shao-lin, "Seismic distribution and dynamic stress response characteristics of slope body under blasting vibration," *Chinese Journal of Rock Mechanics and Engineering*, vol. 33, pp. 3707–3717, 2014.

[33] W. Fu, "Distribution rules of collapsible loess and analysis on foundation treatment technology on Baoji-Lanzhou passenger dedicated line," *Railway Standard Design*, vol. 58, no. 11, pp. 15–19, 2014.

[34] K. Xia, L. Dong, X. Pu, and L. I. Lu, "Analysis of seismic response characteristics of loess Tableland," *Rock and Soil Mechanics*, vol. 41, no. 01, pp. 295–304, 2020.

[35] O. Junhiko, *Spectral Analysis of Ground Motion*, Seismology Press, Beijing, China, 2008.

Hindawi
Shock and Vibration
Volume 2023, Article ID 1737203, 13 pages
https://doi.org/10.1155/2023/1737203

Research Article

Seismic Behavior of Qinghai-Tibetan Railway Embankment in Permafrost Regions: A Case Study

Tuo Chen,[1,2] **Jianzhou Wang**,[1] **and Bo Wang**[1]

[1]*The State Key Laboratory for Geomechanics and Deep Underground Engineering, China University of Mining & Technology, Xuzhou 221116, China*
[2]*Key State Laboratory of Frozen Soil Engineering, Northwest Institute of Eco-Environment and Resources, CAS, Lanzhou 730000, China*

Correspondence should be addressed to Jianzhou Wang; wjzh@cumt.edu.cn

Received 5 May 2022; Revised 19 October 2022; Accepted 7 February 2023; Published 20 February 2023

Academic Editor: Ai Lan Che

The temperature is a critical factor that determines the unfrozen water content and ice content in the frozen soil. In view of mechanical properties of the frozen soil depend on the volume of components of the four-phase systems, thus the temperature has a significant impact on the mechanical behaviors and deformation properties. The thermal state of the embankment in permafrost regions has a significant seasonal difference, then the seismic performance of the embankment alters with the season. In addition, the seismic performance is highly influenced by the properties of the earthquake motion, especially the seismic intensity. Combining these factors, a numerical simulation was conducted in this study. In this study, taking a typical section of Qinghai-Tibet Railway as an example, a numerical case study on the seismic behavior of embankment was carried out using the dynamic explicit FEM code ABAQUS/Explicit. The El Centro excitation with different intensities was performed in numerical analysis and two distinct thermal states of the embankment in extreme cold and warm days were considered as well. The seismic behaviors of the embankment, including the acceleration responses, the strain response, and the displacement response, were studied effectively. This paper proposes approaches and methods to study the seismic failure mechanism of the infrastructures, and the results can serve as a scientific basis for resisting earthquakes and preventing disasters in cold regions.

1. Introduction

The Qinghai-Tibet Plateau (QTP) is the largest high-altitude permafrost region at low- and mid-latitudes in the world [1]. The permafrost area on the Qinghai-Tibet Plateau is estimated to be about $1.04 \times 10^6\,\mathrm{km}^2$ [2]. With the in-depth implementation of the western China development strategy and the construction of "Belt and Road," there is an increasing demand for cold region engineering in China. It is imperative to construct major national strategic projects in high-altitude permafrost regions. The Qinghai-Tibet Expressway, the Golmud—Lhasa oil product pipeline, the high voltage power transmission and transformation line, and other major construction projects will be constructed on the QTP. Furthermore, it needs to be recognized that the tectonic movement and crustal deformation are very strong and active faults are widely distributed. The QTP is located in the region with the most intensive deformation and high-level seismic activities. Seismologists are now suggesting the QTP has entered the third active seismic period since 1995 [3]. A sequence of large earthquakes occurred, including the Mani earthquake (Ms 7.9) on November 8, 1997; the Kunlunshan earthquake (Ms 8.1) on November 14, 2001; the Wenchuan earthquake (Ms 8.0) on May 12, 2008; the Yushu earthquake (Ms 7.1) on April 14, 2010; the Yutian earthquake (Ms 7.3) on February 12, 2014, and the Menyuan earthquake (Ms 6.9) on January 8, 2022, has attracted attention from engineers and researchers. These earthquakes produced surface ruptures with complicated structures and a great length, which had brought enormous damages to the transport infrastructures in the QTP area. Figure 1 illustrates the surface rupture zone in the permafrost area caused by the

Kunlunshan earthquake and the Menyuan earthquake, respectively. The potential earthquake risk has been a significant engineering challenge to the construction and maintenance of infrastructure in permafrost regions [4]. As a typical transport infrastructure, railway embankment damage, including rupture and deformation, may occur during an earthquake. Furthermore, the damage of the embankment was not observed in a typical earthquake. Thus the study of seismic response of linear engineering structures in permafrost regions, especially railway engineering, has become a key problem that needs to be solved as soon as possible.

Frozen soil is a kind of composite material composed of soil, unfrozen water, and ice. Compared with ordinary soil, the most obvious physical quantities are freezing temperature and unfrozen water content [5, 6]. Due to mechanical instability and temperature sensitivity, frozen soil can be categorized as "special" soil and its physical and mechanical properties may broadly differ across seasons [7]. As for the embankment engineering in cold regions, the interaction between frozen soil and climatic system directly affects the seismic dynamic response and failure characteristics. The seismic performance varies significantly in different seasons and regions, directly influencing the strategies of earthquake prevention and disaster mitigation. Thus, it is essential to study the seismic response and dynamic stability of the embankment in permafrost regions. The most direct research approach to studying the seismic behavior of structures is the shaking table test. In recent years, this method has been used wildly in embankment engineering [8–11]. However, there still have some shortcomings to this method, such as the huge cost and time-consuming, reduced scale model testing. Furthermore, it is very difficult to consider the effects of environmental factors on the seismic behavior of the embankment, such as the freezing and thawing process. With the rapid development of computer technology, the numerical analysis method has become an important and practical tool and provides an economical way to study the seismic behavior of embankments in permafrost regions. Wang et al. [12, 13] studied the earthquake dynamic stress characteristic and seismic displacement characteristic of the roadbed on permafrost site, and then proposed the stress intensity criteria of earthquake breakage. Esmaeili and Noghabi [14] developed a finite-element model to investigate the dynamic behavior of ballasted railway tracks subjected to earthquake motion. Chen et al. [15] discussed the impact of permafrost change on the seismic site response and then studied the dynamic response of the traditional embankment in permafrost regions. Li et al. [16, 17] investigated seasonal differences in seismic responses of an embankment on a sloping ground in permafrost regions. In addition, a thermo-dynamic coupled model for the crushed-rock embankment was proposed and a series of numerical computations were conducted. However, despite the fact that seismic responses of embankments in permafrost regions have been studied by many authors, few papers have been published on the seasonal differences in seismic responses of embankments in permafrost regions induced by an earthquake with different intensities.

In this work, based on a prototype of a typical traditional embankment at the Beiluhe section of the QTR, a full-scale simulation model is established to study the seismic behavior of the embankment under earthquake excitation. An actual seismic record (EI Centro earthquake, 1940) is selected as the input ground motion and different intensities were considered. Moreover, two distinct thermal states of the embankment on extreme cold and warm days are considered as well. The seismic behaviors of an embankment, including the acceleration responses, the strain response, and the displacement response, were studied effectively. The objective of this research is to obtain more details about the seismic behaviors of the embankment and to investigate the seismic damage evolution and failure process of embankment in permafrost regions.

2. Numerical Model and Basic Equations

2.1. Model of Railway Embankment. The Beiluhe segment, located in an arid climate region of QTP, belongs to the unfavorable and bad engineering geological section. The MAGT of this segment varies from −1.41 and −1.68°C. The freezing period of which is from September to the following April [18]. The active layer thaws in summer while freezes in winter, and the natural permafrost table of the segment is between −2 m and −3 m [19]. Moreover, the thick ice layer underground near the permafrost table is abundant, and the temporal and spatial variations in the thermal regime are observed in this segment. Whereas, different types of embankments have been constructed, such as traditional embankments, crushed-rock embankments, duct-ventilated embankments, and thermosiphon embankments.

Figure 2 illustrates the cross-section profile of a typical traditional embankment and the soil layer structure at the Beiluhe section K1137 + 700 of the QTR. The surface layer of the ground, defined as the active layer, is a gravelly sand layer. Beneath the active layer, there exists the frozen silty clay, also named as permafrost. The underlying permafrost contains the upper ice-poor permafrost with a thickness of 6 m and the lower ice-poor permafrost with a thickness of 22 m. According to the ground temperature measurement conducted by the State Key Laboratory of Frozen Soil Engineering, Chinese Academy of Science, the natural ground temperature variation and the distribution of mean annual ground temperature are defined; [20–22]. The natural permafrost table is approximately 2 m, and the temperature of the permafrost in this area is about −1.0°C.

Based on the prototype of the typical traditional embankment at the Beiluhe section, a full-scale numerical model of the embankment is established, as shown in Figure 3. The simulation is performed based on the plane strain assumption. In this study, the size of the mesh was controlled in order to guarantee the accuracy of dynamic analysis. The mesh size is limited by the shortest wavelength of the input seismic wave. To ensure the authenticity of wave propagation in the media, the maximum size of the element must be less than 1/10~1/8 of the minimum wavelength. In our simulation, the maximum mesh size is only 1 m × 1 m, and the accuracy of calculation meets the requirements.

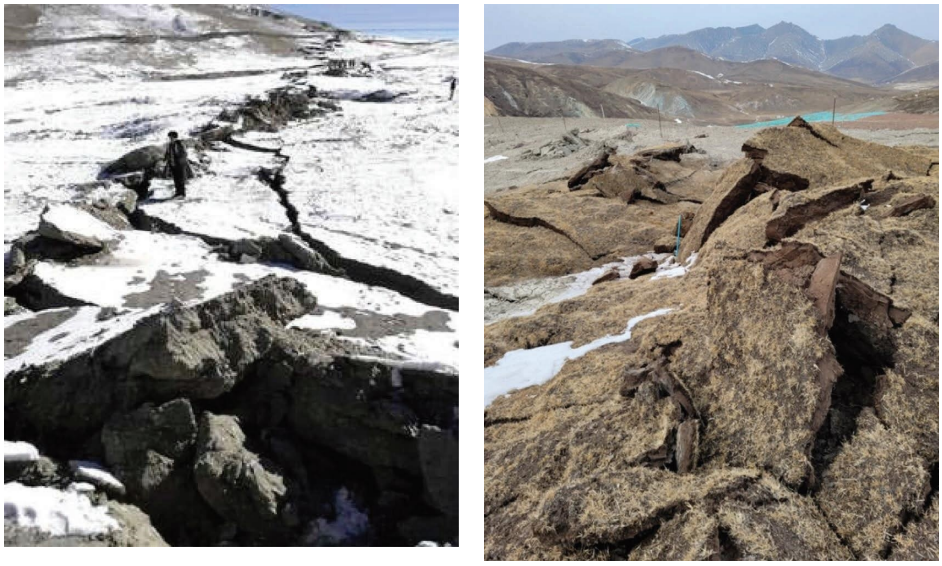

(a) (b)

Figure 1: Surface rupture zone in permafrost area caused by earthquakes: (a) Kunlunshan earthquake; (b) Menyuan earthquake.

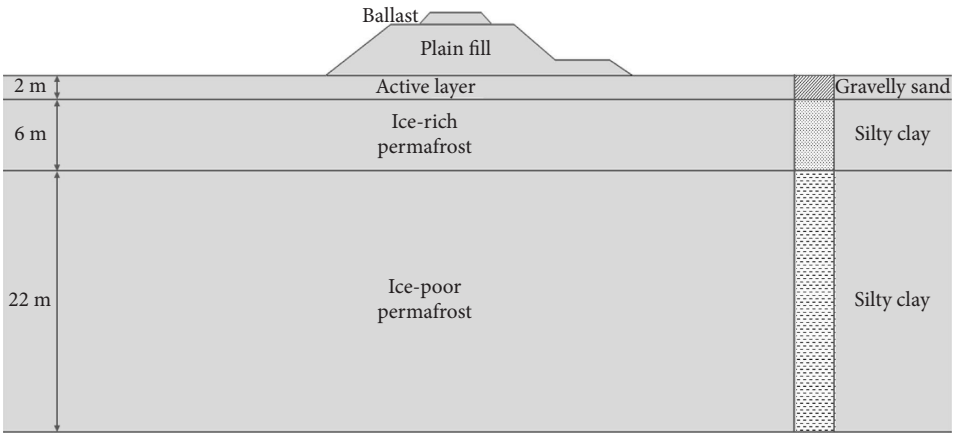

Figure 2: The cross-section profile and the soil layer structure of a typical traditional embankment.

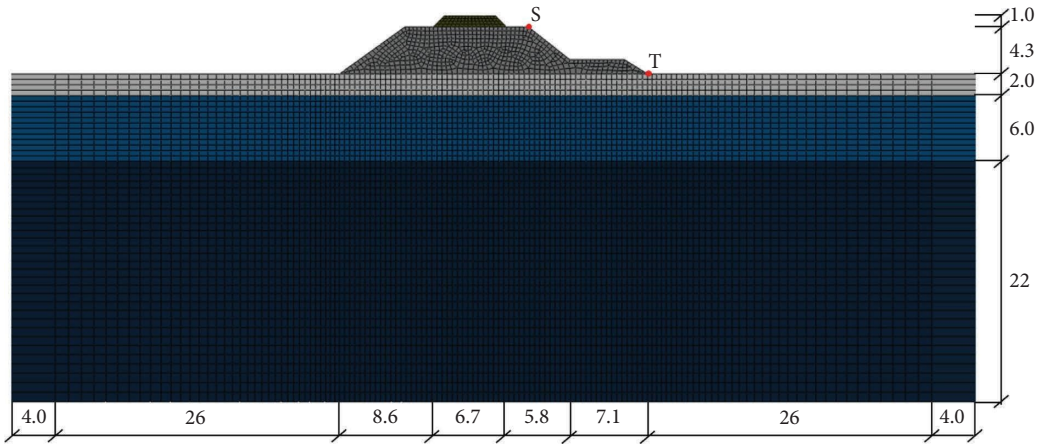

Figure 3: The full-scale numerical model of a typical traditional embankment (unit: m).

In the numerical model, two different boundary conditions are used, respectively. On the left and right sides of the numerical model, the free field method is taken to prevent wave reflection at the boundary of the embankment model. Moreover, the artificial boundary conditions are adopted at the bottom of the model where the horizontal direction is released and the artificial seismic waves are used as the input seismic motion for the numerical calculation.

2.2. Basic Equations. To study the dynamic behavior of the Qinghai-Tibet railway embankment under seismic loads, the nonlinear dynamic finite element analysis method is applied. The kinetic equation can be expressed as follows:

$$M \bullet \ddot{x}(t) + C \bullet \dot{x}(t) + K \bullet x(t) = P(t), \tag{1}$$

where M, C, and K are, respectively, the mass matrix, stiffness matrix, and damping matrix. $P(t)$ refers to the dynamic loading.

When the dynamic loading is small, the soil is in an elastic stage which adopts the linear elastic model, its stress-strain relation meets Hook's law. When the loading is getting greater, the elastoplastic properties of the soil need to be considered. As for any stress increment $d\{\sigma\}$, the total strain increment $d\{\varepsilon\}$ includes elastic strain increment $d\{\varepsilon^e\}$ and plastic strain increment $d\{\varepsilon^p\}$, which could be written as follows:

$$d\{\varepsilon\} = d\{\varepsilon^e\} + d\{\varepsilon^p\} = [D_T]^{-1} d\{\sigma\} + d\lambda \left\{\frac{\partial F}{\partial \sigma}\right\}, \tag{2}$$

where $[D_T]$ is the elastic matrix related to temperature and unfrozen water, the $d\lambda$ is the plastic coefficient, and F represents the plastic potential function.

In this paper, the Mohr–Coulomb elastic-plastic yield criterion is utilized to express the plastic potential function. This criterion assumes that soil failure occurs when shear stress in the plane of the material exceeds the value, which is linearly dependent on the normal stress to that plane [23, 24]. The Mohr–Coulomb criterion can be written as follows:

$$F = \frac{J_1}{3} \sin\varphi + \sqrt{J_2'}\left(\cos\theta - \frac{1}{\sqrt{3}} \sin\theta \sin\varphi\right) - C\cos\varphi = 0, \tag{3}$$

where J_1 is the first stress tensor invariant; J_2' denotes the second deviatoric stress tensor invariant, and θ is the Lode angle. C denotes the cohesive strength and φ denotes the internal friction angle, C and φ are related to the temperature.

3. Model Parameters and Input Seismic Motion

The freezing and thawing states are different at different times with the variation of the air temperature, which influences the soil water migrations in the embankment. The seismic behavior analysis of the embankment in the permafrost area is a very complicated problem when considering this impact. However, in order to simplify the study, two extreme situations including the warmest and coldest seasons are considered. In the warmest season, the roadbed filling and the active layer are supposed to be completely thawed. While in the coldest season, the roadbed filling and the active layer are fully frozen. The mudstone is always frozen all year round. The soil was regarded as an elastic-plastic material and the ballast was assumed to be a linear elastic material [25]. Then different soil mechanic parameters are endowed in different situations. The mechanical parameters of the numerical model are presented in Table 1, based on a series of triaxial tests [26–28]. The temperature in Table 1 is determined based on the ground temperature data at the Beiluhe section.

In this work, the El Centro earthquake wave (N-S direction) that occurred in 1940, is selected as seismic load in the numerical case study. Acceleration time history and fast Fourier transform (FFT) curves are presented in Figure 4. The maximum acceleration is 0.348 g and the predominant frequency is 1.47 Hz.

According to the seismic intensity zoning map in China, the QTP is located in areas with high seismic intensity above VII degrees. Thus in the numerical analysis, the acceleration amplitude of the input seismic motion is adjusted from 0.15 g to 0.4 g, which corresponds to different earthquake intensities (from intensity VII to intensity IX). The adjusted amplitudes and the amplification coefficients are shown in Table 2.

4. Numerical Simulation Results

In order to accurately capture the mechanical behavior of the embankment during the seismic loading, the acceleration response characteristics are investigated, as well as the dynamic strain and displacement response. Considering the dynamic stability of the embankment is largely concerned, then the characteristic point S on the embankment's shoulder and the characteristic point T at the toe of the embankment, are arranged in the model.

4.1. Acceleration Response Analysis. In this case study, the seismic input motion is in the horizontal direction and thus the horizontal acceleration response of the embankment in different seasons is investigated. The acceleration contour map of the embankment in warm and cold seasons, under the El Centro seismic motion, are depicted in Figures 5(a) and 5(b), respectively.

It can be well demonstrated that the rail embankment has an obvious amplification effect on the seismic wave, comparing the natural surface. The acceleration response of the embankment is greater in the warm season than in the cold season. Furthermore, the maximum acceleration appears at the top of the embankment in the cold season, while the acceleration at both embankment slopes is more significant in the warm season. The main reason for this phenomenon is the stiffness improvement of the embankment in cold seasons. The elastic modulus and strength of soil inside the embankment are distinctly enhanced. Consequently, the seismic acceleration responses of the

Table 1: Soil mechanics parameters at the survey area.

Lithology	Water content (%)	Temperature (°C)	Density (kN/m^3)	Elastic modulus (kPa)	Poisson ratio	Cohesion force (kPa)	Internal frictional angle
Ballast	—	5	20.0	2.00*E*5	0.30	—	—
Roadbed filling	26.3	2	19.0	6.10*E*4	0.31	30	23°
	26.3	−1	19.0	1.14*E*5	0.29	120	32°
Silty clay	20	0.5	18.0	2.80*E*4	0.35	150	22°
	20	−1	18.0	5.40*E*4	0.31	240	30°
Mudstone	15.2	−1	21.0	3.40*E*5	0.25	340	39°

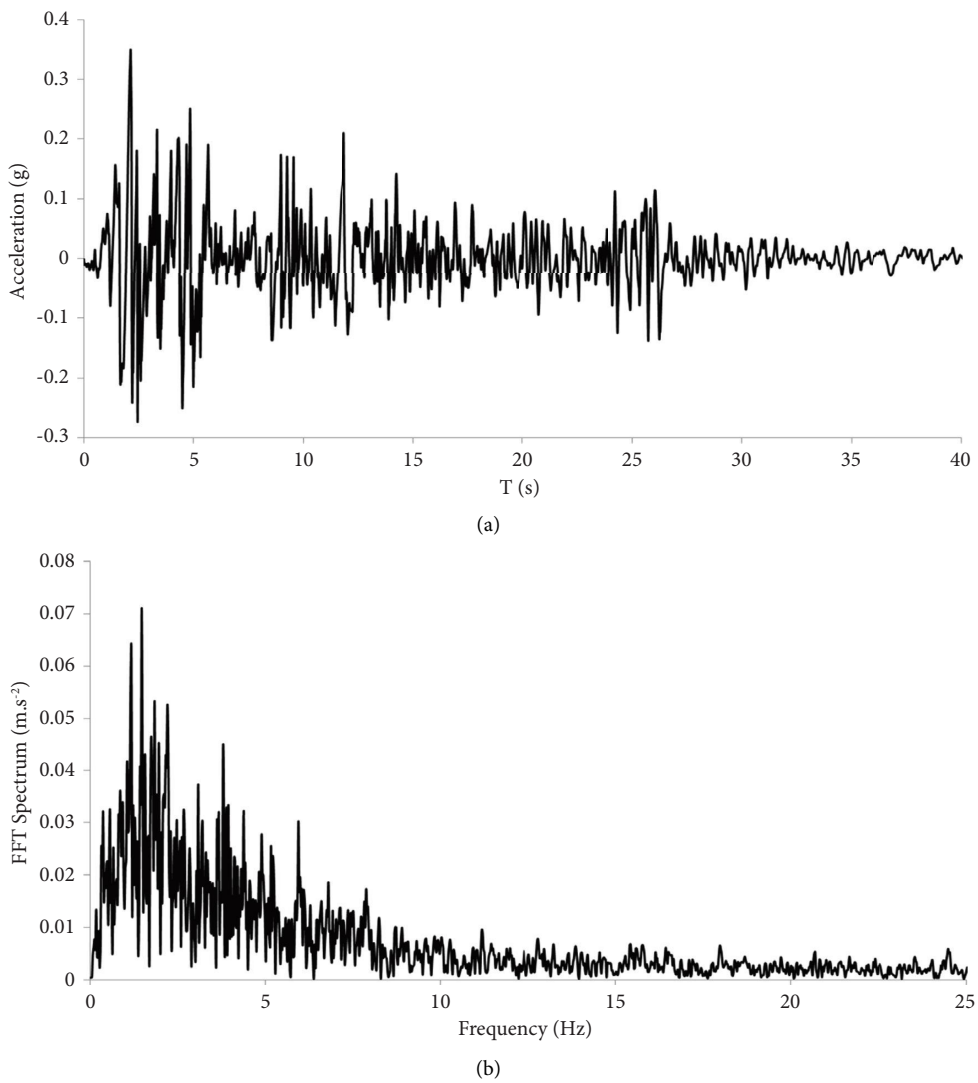

Figure 4: Acceleration time historie and FFT spectra of El Centro earthquake wave: (a) the acceleration time history; (b) the FFT spectra.

Table 2: Adjusted amplitudes and the amplification coefficients of the input seismic load.

Adjusted amplitude	0.15 g	0.2 g	0.25 g	0.3 g	0.348 g	0.4 g
Amplification coefficients	0.43	0.57	0.72	0.86	1.0	1.15
Seismic intensity	VII	VIII	VIII	VIII	VIII	IX

embankment are weakened, which is similar to the soil reinforcement effect.

The acceleration time history curve of the characteristic point S and point T is indicated in Figures 6(a) and 6(b), respectively. The maximum acceleration on the embankment's shoulder is 8.45 $m{\cdot}s^{-2}$ and 7.86 $m{\cdot}s^{-2}$ in the warm and cold seasons, respectively. In contrast, the maximum acceleration at the toe of the embankment is 5.08 $m{\cdot}s^{-2}$ and 4.65 $m{\cdot}s^{-2}$ in the warm and cold seasons, respectively. The acceleration amplitude becomes larger in the warm season and the amplification effect of the embankment's shoulder is more significant compared with the toe of the embankment.

In order to quantify the seismic response of the rail embankment, the maximum acceleration is characterized using the amplification coefficient, which is defined as the ratio of peak ground acceleration to input seismic acceleration. The variation of amplification coefficients with the input ground motion acceleration amplitude, of characteristic points S and T, are illustrated in Figure 7.

The results indicate that the acceleration amplification coefficient of railway embankment is significantly larger in warm seasons compared with cold seasons, and the acceleration amplification effect on the embankment's shoulder is more significant than the slope toe. Moreover, the

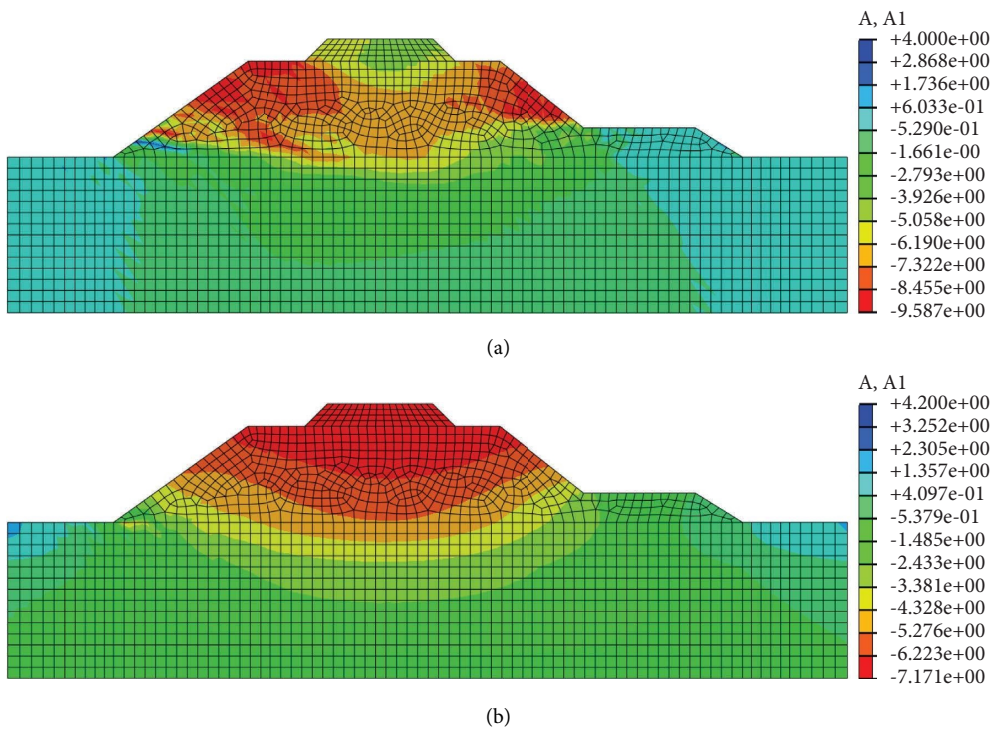

Figure 5: The Peak ground horizontal acceleration contour in different seasons: (a) horizontal acceleration contour map of the embankment in the warm season; (b) horizontal acceleration contour map of the embankment in the cold season.

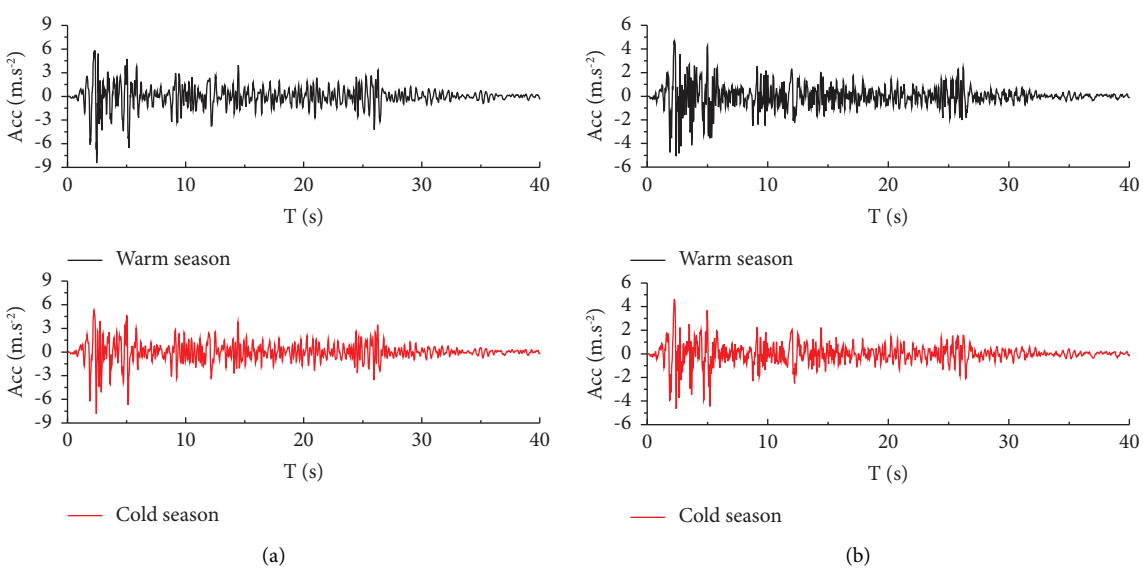

Figure 6: The acceleration time history curve of the characteristic point in different seasons: (a) characteristic point S; (b) characteristic point T.

acceleration amplification coefficient will decrease with the increase of input acceleration amplitude, exhibiting approximately linear characteristics. This tendency can be expressed using the following linear formula in slope-intercept form:

$$y = -kx + b. \tag{4}$$

In the formula mentioned above (equation (4)), the slope parameter k indicates the attenuation degree of acceleration,

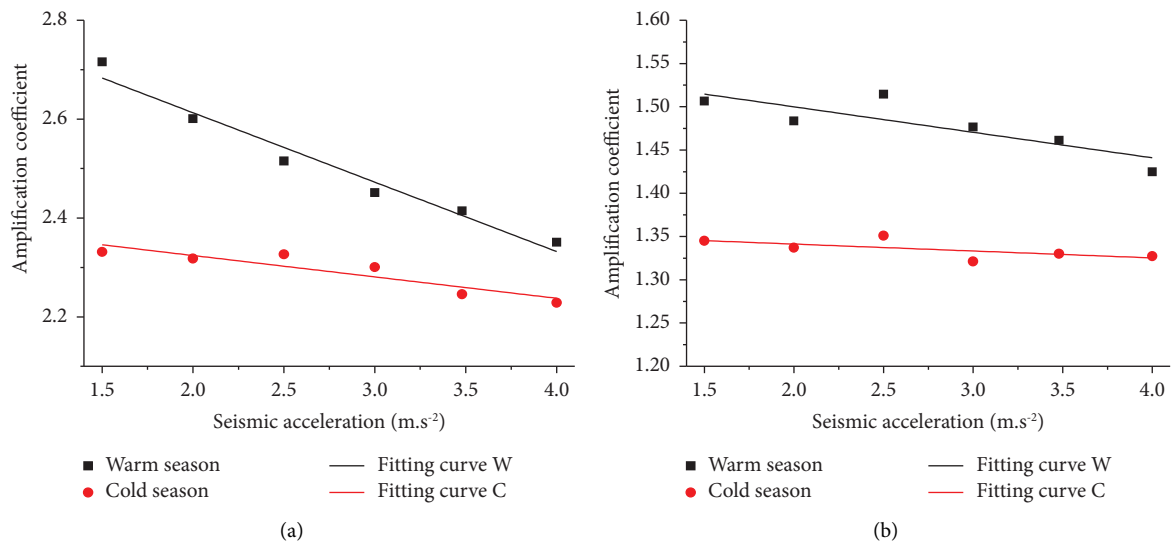

Figure 7: The variation of amplification coefficient with the input ground motion acceleration amplitude: (a) characteristic point S; (b) characteristic point T.

and the intercept parameter b shows the maximum amplification coefficient, as shown in Table 3.

4.2. Velocity Response Analysis. The velocity time history curve of the characteristic point S and point T is indicated in Figures 8(a) and 8(b), respectively. The maximum velocity on the embankment's shoulder is 0.84 m·s^{-1} and 0.67 m·s^{-1} in the warm and cold seasons, respectively. In contrast, the maximum acceleration at the toe of the embankment is 0.60 m·s^{-1} and 0.54 m·s^{-1} in the warm and cold seasons, respectively. The velocity response is greater in the warm season and the value is larger on the embankment's shoulder compared with the toe of the embankment.

Figure 9 illustrates the variation of the maximum velocity magnitude with the input ground motion acceleration amplitude. The maximum velocity magnitude increases with the increase of input acceleration amplitude. Moreover, the velocity difference ΔV between the point S and point T increases with the increasing input acceleration, and this value in the warm season ΔV_w is greater than in the cold season ΔV_c. It is indicated that the embankment is prone to cracking or deformation in the warm season.

4.3. Displacement Response Analysis. Figure 10 illustrates the displacement time history on the embankment's shoulder in a horizontal direction. This displacement is the relative value between point S and point T. The displacement changes nonlinearly with the duration time of the earthquake, presenting a maximum value at the peak acceleration time. The maximum displacement on the embankment's shoulder is 7.44 cm and 6.74 cm in the warm and cold seasons, respectively.

Figure 11 illustrates the distribution of the maximum relative displacement with the input ground motion acceleration amplitude in different seasons. As observed in Figure 10, the horizontal displacement on the embankment's shoulder is larger in the warm season than in the cold season. The displacement increases with the increase of input ground motion acceleration amplitude, and the variation tendency is approximately linear. The maximum displacement on the embankment's shoulder can reach up to 9 cm under the action of 0.4 g seismic excitation in the warm season, while this value is only 2.6 cm under the action of 0.2 g seismic excitation in the cold season. It can be considered that cracks or even collapse will occur when the input peak acceleration reaches a certain value.

4.4. Strain Response Analysis. Figure 12 illustrates the maximum plastic strain of the embankment under the seismic motion with different peak accelerations, in different seasons. It is concluded from the results that the plastic zone gradually appears in the embankment when the seismic intensity reaches a certain value. The plastic zone starts to develop at the slope toe of the embankment, and there exists a continuous extension of the plastic zone with the increase of the seismic intensity. Moreover, on the left side of the embankment, where there is no pavement, the plastic strain exponent is larger and the plastic deformation was significantly higher.

Subsequently, the variation of the maximum plastic strain magnitude in the railway embankment with the input ground motion acceleration amplitude is illustrated in Figure 13. With the increase of input acceleration amplitude, the maximum plastic strain magnitude increase, and this trend is more significant in warm seasons. In a warm season, there is no plastic zone generated in the embankment until the input acceleration amplitude reaches 2.0 m·s^{-2}. The plastic strain magnitude ranges from 4.43 $E-3$ to 2.92 $E-2$, and the corresponding acceleration amplitude is within the range from 2.0 to 4.0 m·s^{-2}. In a cold season, the plastic will appear when the input acceleration amplitude reaches 2.5 m·s^{-2}, and the plastic strain magnitude varies from

Table 3: The value of slope and intercept parameter.

Characteristic point	The location	Characteristic time	Slope-intercept parameters	
			k	b
S	Embankment's shoulder	Warm season	0.14	2.89
	Embankment's shoulder	Cold season	0.04	2.41
T	Embankment slope toe	Warm season	0.02	1.56
	Embankment slope toe	Cold season	0.007	1.36

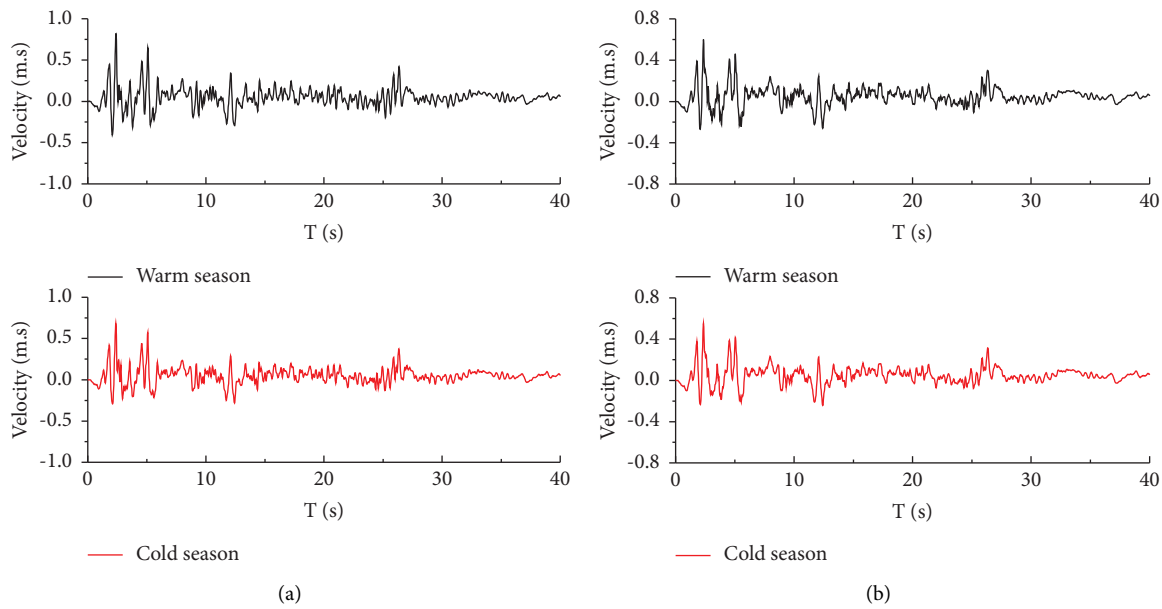

Figure 8: The velocity time history curve of the characteristic point in different seasons: (a) characteristic point S; (b) characteristic point T.

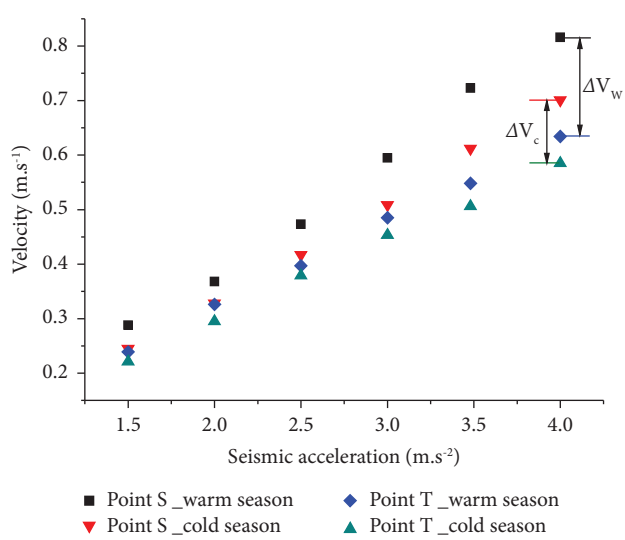

Figure 9: The variation of maximum velocity with the input ground motion acceleration amplitude.

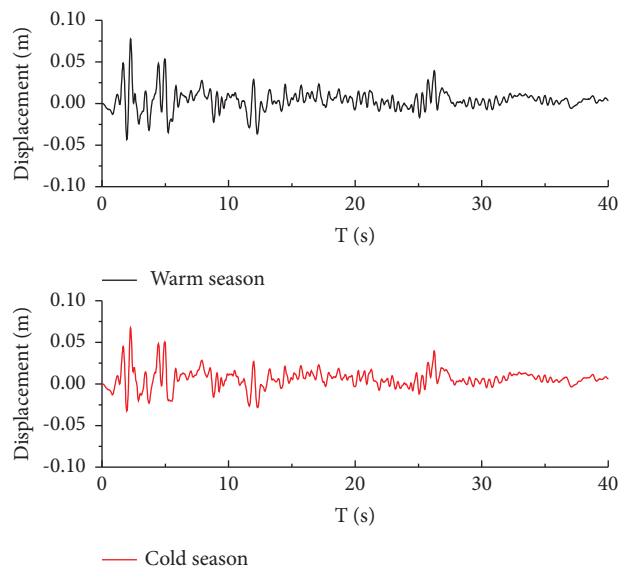

Figure 10: The displacement time history on the embankment's shoulder.

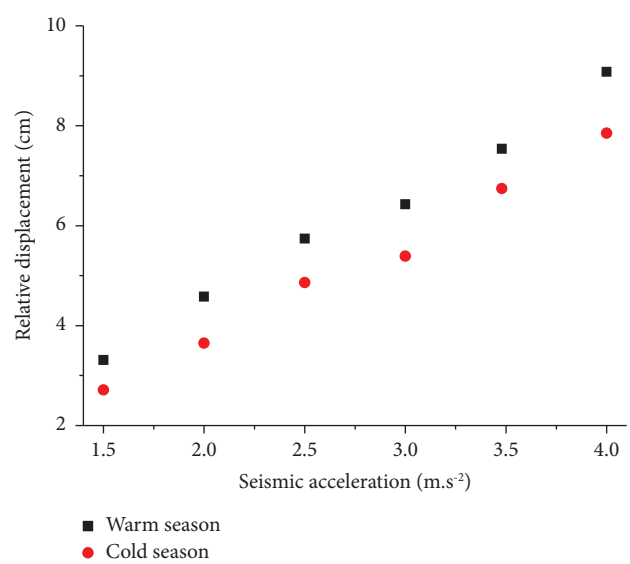

Figure 11: The distribution of the maximum relative displacement.

2.19 $E-3$ to 6.17 $E-3$ when the input acceleration amplitude change from 2.5 to 4.0 m·s^{-2}.

5. Discussion

It has now been confirmed that the seismic response of the embankment structure in permafrost regions is a very complicated water-heat-dynamic coupled problem. There is a real difficulty in the ability to simulate soil hydro-thermal transport processes and the deformation-damage-failure process, especially under earthquake excitation. Because of this, very few theoretical and practical results available up to now. As a preliminary study, the numerical simulation in this paper still has some deficiencies. But despite this, the results of our study are consistent with the findings of previous research. Furthermore, our study has revealed some other interesting findings. It is observed that the location of the maximum plastic strain that occurred seems not to coincide with the peak acceleration locations. Because the plastic strain is a parameter to quantify the damage, which reflects the differences or the relationship between the stress and strength. While the acceleration response characteristic is mainly related to the soil layer stiffness.

In this paper, starting from the variation of the dynamic response characteristics, we try to make a quantitative risk analysis of the embankment in permafrost regions. Through our research work, it is found that the vulnerability evaluation of the embankment becomes possible when associated with the variation of the plastic strain.

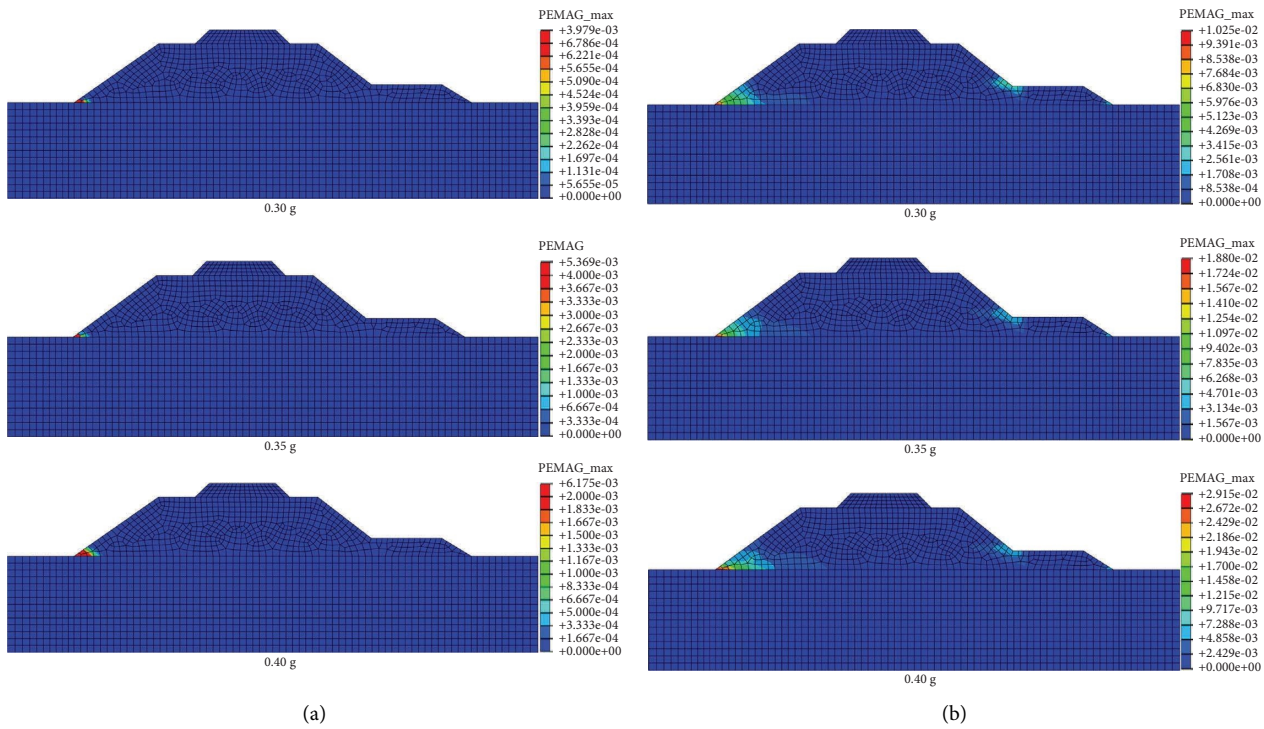

Figure 12: The maximum plastic strain of the embankment under the seismic motion: (a) in the cold season; (b) in the warm season.

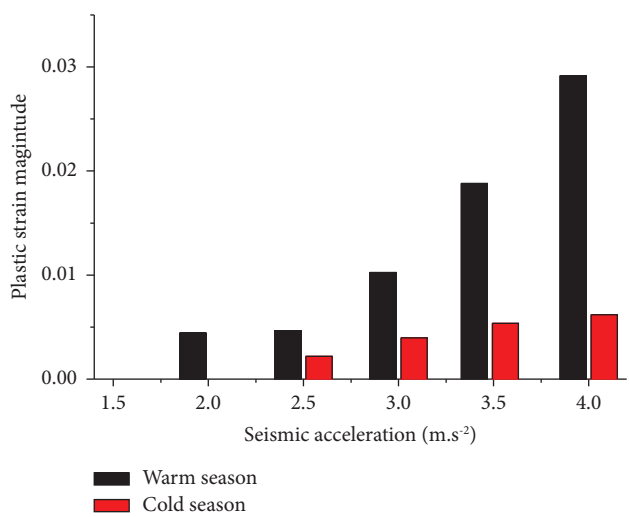

Figure 13: The variation of maximum plastic strain with the input ground motion acceleration amplitude.

6. Conclusions

In this work, based on a prototype of a typical traditional embankment at the Beiluhe section of the QTR, a full-scale simulation model is established and a numerical case study on the seismic behavior of embankment is performed. Two different thermal states of the embankment in extreme cold and warm days are considered, and the influence of seismic intensity on the dynamic response is discussed. The following conclusions can be drawn from the results of this study:

(1) The dynamic response at different positions of the embankment varies greatly in different seasons. The maximum acceleration appears at the top of the embankment in the cold season, while the acceleration at both embankment slopes is more significant in the warm season.

(2) From the acceleration, velocity, and displacement analysis, it can be concluded that cracks or even collapses will occur when the input peak acceleration reaches a certain value. The embankment is prone to collapse or damage in the warm season.

(3) The acceleration amplification coefficient will decrease with the increase of input acceleration amplitude, exhibiting approximately linear characteristics. The displacement increases with the increase of input ground motion acceleration amplitude, and the variation tendency is approximately linear.

(4) With the increase of input acceleration amplitude, the maximum plastic strain magnitude increase, and this trend is more significant in warm seasons. In a warm season, there is no plastic zone generated in the embankment until the input acceleration amplitude reaches 2.0 $m \cdot s^{-2}$. In a cold season, the plastic will appear when the input acceleration amplitude reaches 2.5 $m \cdot s^{-2}$.

Data Availability

All data included in this study are available from the corresponding author upon request.

Conflicts of Interest

The authors declare that they have no conflicts of interest.

Acknowledgments

This study is financially supported by the National Natural Science Foundation of China (grant nos. 41701058 and 51874286), the Open Fund of State Key Laboratory of Frozen Soil Engineering (grant no. SKLFSE201606). The authors would like to express their sincere thanks to the anonymous reviewers for their valuable suggestions and constructive comments which greatly improved the presentation of this paper.

References

[1] X. Li, Q. Wu, R. Li et al., "Characteristic, changes and impacts of permafrost on Qinghai-Tibet Plateau," *Chinese Science Bulletin*, vol. 64, no. 27, pp. 2783–2795, 2019.

[2] J. Ni, T. Wu, X. Zhu et al., "Simulation of the present and future projection of permafrost on the Qinghai-Tibet Plateau with statistical and machine learning models," *Journal of Geophysical Research: Atmospheres*, vol. 126, no. 2, Article ID e2020JD033402, 2021.

[3] Q. D. Deng, S. P. Cheng, J. Ma, and P. Du, "Seismic activities and earthquake potential in the Tibetan plateau," *Chinese Journal of Geophysics*, vol. 57, no. 7, pp. 2025–2042, 2014.

[4] A. M. Lin, B. H. Fu, J. M. Guo et al., "Coseismic strike-slip and rupture length produced by the 2001 Ms 8.1 Central Kunlun Earthquake," *Science*, vol. 296, no. 5575, pp. 2015–2017, 2002.

[5] Z. W. Wu and Y. Z. Liu, *Frozen Subsoil and Engineering*, Ocean Press, Lancing, England, 2005.

[6] F. J. Niu, J. M. Zhang, and J. Z. Zhang, "Engineering geological characteristics and evaluations of permafrost in Beiluhe testing field of Qinghai-Tibetan Railway," *Journal of Glaciology and Geocryology*, vol. 24, no. 3, pp. 264–269, 2002.

[7] L. U. Arenson and S. M. Springman, "Mathematical descriptions for the behaviour of ice-rich frozen soils at temperatures close to 0 °C," *Canadian Geotechnical Journal*, vol. 42, no. 2, pp. 431–442, 2005.

[8] J. B. Li, H. R. Zhang, and Z. Q. Li, "Large scale shaking table test study of dynamic response and dynamic failure of subgrade," *Chinese Journal of Rock Mechanics and Engineering*, vol. 30, no. S2, pp. 3746–3754, 2011.

[9] Y. L. Lin, "Deformation behavior of reinforced embankment slopes under seismic excitation," *Disaster Advances*, vol. 6, no. 7, pp. 12–19, 2013.

[10] C. W. Yang, X. H. Tong, and D. Wang, "Shaking table test of dynamic response law of subgrade with ballast track under earthquake," *Rock and Soil Mechanics*, vol. 41, no. 7, pp. 2215–2223, 2020.

[11] W. Z. Chen, Y. Liu, and H. Y. Chen, "Shaking table test on slope subgrade reinforced by boredpiles of Sichuan-Tibet railway," *Chinese Journal of Rock Mechanics and Engineering*, vol. 39, no. 12, pp. 2540–2556, 2020.

[12] L. X. Wang, X. Z. Ling, and X. Y. Xu, "Study on earthquake dynamic stress characteristic of roadbed on permafrost site," *Earthquake Engineering and Engineering Vibration*, vol. 24, no. 1, pp. 117–121, 2004.

[13] L. X. Wang and X. Z. Ling, "Study on differentiate criteria of earthquake breakage of frozen roadbed," *Chinese Journal of Rock Mechanics and Engineering*, vol. 24, no. 4, pp. 638–642, 2005.

[14] M. Esmaeili and H. H. Noghabi, "Investigating seismic behavior of ballasted railway track in earthquake excitation using finite-element model in three-dimensional space," *Journal of Transportation Engineering*, vol. 139, no. 7, pp. 697–708, 2013.

[15] T. Chen, W. Ma, and G. Q. Zhou, "Numerical analysis of ground motion characteristics in permafrost regions along the Qinghai-Tibet Railway," *Cold Regions Science and Technology*, vol. 148, pp. 88–95, 2018.

[16] S. Y. Li, Y. M. Lai, M. Y. Zhang, and W. Yu, "Seasonal differences in seismic responses of embankment on a sloping ground in permafrost regions," *Soil Dynamics and Earthquake Engineering*, vol. 76, no. 1, pp. 122–135, 2015.

[17] S. Y. Li, M. Y. Zhang, W. S. Pei, Y. Lai, and W. Yu, "Thermo-seismic characteristics of a crushed-rock interlayer embankment on a permafrost slope," *Cold Regions Science and Technology*, vol. 151, pp. 249–259, 2018.

[18] Z. Z. Sun, W. Ma, and D. Q. Li, "Ground temperature characteristics of block stone embankment characteristics of block stone embankment and traditional embankment at Beiluhe along Qinghai-Tibet Railway," *Chinese Journal of Geotechnical Engineering*, vol. 30, no. 2, pp. 303–308, 2008.

[19] M. L. Zhang, Z. Wen, and K. Xue, "The effects of precipitation on thermal - moisture dynamics of active layer at Beiluhe permafrost region," *Journal of Arid Land Resources & Environment*, vol. 30, no. 4, pp. 159–164, 2016.

[20] W. Ma, C. H. Shi, Q. B. Wu, L. X. Zhang, and Z. J. Wu, "Monitoring study on technology of the cooling roadbed in permafrost region of Qinghai–Tibet plateau," *Cold Regions Science and Technology*, vol. 44, no. 1, pp. 1–11, 2006.

[21] W. Ma, Y. H. Mu, Q. B. Wu, Z. Z. Sun, and Y. Z. Liu, "Characteristics and mechanisms of embankment deformation along the Qinghai–Tibet Railway in permafrost regions," *Cold Regions Science and Technology*, vol. 67, no. 3, pp. 178–186, 2011.

[22] Y. H. Mu, W. Ma, Q. B. Wu, Z. Z. Sun, Y. Z. Liu, and G. Qu, "Thermal regime of conventional embankments along the Qinghai–Tibet Railway in permafrost regions," *Cold Regions Science and Technology*, vol. 70, no. 1, pp. 123–131, 2012.

[23] M. Taiebat, H. Shahir, and A. Pak, "Study of pore pressure variation during liquefaction using two constitutive models for sand," *Soil Dynamics and Earthquake Engineering*, vol. 24, pp. 551–564, 2007.

[24] R. Uzuoka, N. Sento, M. Kazama, F. Zhang, A. Yashima, and F. Oka, "Three-dimensional numerical simulation of earthquake damage to group-piles in a liquefied ground," *Soil Dynamics and Earthquake Engineering*, vol. 27, no. 5, pp. 395–413, 2007.

[25] A. L. Che, I. Takahiro, and X. R. Ge, "Dynamic behaviors of subway structure subjected to strong earthquake motions using shaking table tests and dynamic analyses," *Rock and Soil Mechanics*, vol. 27, no. 8, pp. 1293–1298, 2006.

[26] S. P. Zhao, Y. L. Zhu, and P. He, "Testing study on dynamic mechanics parameters of frozen soil," *Chinese Journal of Rock Mechanics and Engineering*, vol. 22, no. 2, pp. 2677–2681, 2003.

[27] Y. M. Lai, Y. Zhang, S. J. Zhang, and L. Jin, "Experimental study of strength of frozen sandy soil under different water contents and temperatures," *Rock and Soil Mechanics*, vol. 30, no. 12, pp. 3665–3670, 2008.

[28] H. Du, W. Ma, S. Zhang, Z. Zhou, and E. Liu, "Strength properties of ice-rich frozen silty sands under uniaxial compression for a wide range of strain rates and moisture contents," *Cold Regions Science and Technology*, vol. 123, pp. 107–113, 2016.

Hindawi
Shock and Vibration
Volume 2022, Article ID 5241257, 13 pages
https://doi.org/10.1155/2022/5241257

Research Article

Ground Motion and Site Characteristics Evaluation Using Hilbert-Huang Transform Method Based on Light-Moderate Earthquakes

Jinchang Chen,[1] Lanmin Wang,[2,3] Ailan Che,[4] and Hanxu Zhou[5]

[1]*School of Naval Architecture, Ocean and Civil Engineering, Shanghai Jiao Tong University, Shanghai 200040, China*
[2]*Lanzhou Institute of Seismology, China Earthquake Administration, Lanzhou 730000, China*
[3]*Key Lab of Loess Earthquake Engineering, China Earthquake Administration, Lanzhou 730000, China*
[4]*School of Naval Architecture, Ocean and Civil Engineering, Shanghai Jiao Tong University, Shanghai 200040, China*
[5]*School of Naval Architecture, Ocean and Civil Engineering, Shanghai Jiao Tong University, Shanghai 200040, China*

Correspondence should be addressed to Lanmin Wang; wanglm2304@126.com

Received 14 April 2022; Accepted 15 July 2022; Published 12 August 2022

Academic Editor: Pengfei Wang

Compared with strong earthquakes (Ms ≥ 6.0), light-moderate earthquakes (Ms 4–5.9) occurred more frequently and distributed more widely, and rich ground motions have been collected around world. It provides a solid data base for the investigation on the ground motion and regional site characteristics which are closely related to seismic geological disaster. We chose two light-moderate earthquakes in China as study cases. Based on Hilbert-Huang transform, we analyzed the ground motion characteristics in time-frequency domain. Using a stable coda wave and marginal spectrum of it based on horizontal to vertical Fourier spectral ratio (HVSR) method, the site characteristics are clarified. Result shows that the amplitude (instantaneous frequency energy) of Hilbert-Huang spectrum is mainly concentrated within 20 Hz at the stations that are close to epicenter. The energy will change from concentration to divergence in time and frequency and decrease with the increase of epicenter distance under soil site condition. Two earthquakes present a low prominent frequency characteristic (1.075–2.45 Hz). Hilbert energy at soil layer is about 3 times greater than it at rock site when the epicenter distance is close and soil layer can also amplify the instantaneous energy. The predominant frequency of site at each station is within 3.6–6.2 Hz. The predominant frequencies of the earthquakes are lower than the predominant frequencies of the sites and would not produce resonance effects. The result can provide meaningful references for later study works about the characteristics and application of light-moderate earthquakes.

1. Introduction

Ground motion and regional site characteristics are closely related to seismic geological disaster. The seismic response of slope will be significantly amplified, when the predominant frequency of ground motion approaches the natural frequency of slope [1]. The comparative study on the ground motion of bedrock site and soil site with close epicenter distance shows that the ground motion of bedrock site is much smaller than that of soil site, which is mainly due to the amplification effect of soil site on ground motion [2, 3]. Previous studies focused on the characteristics and effects of strong earthquakes (Ms ≥ 6.0), because large casualties and natural disasters were caused [4–6]. However, there are fewer large earthquakes with rich near-field waveform records on the mainland. Therefore, it is difficult to clarify the general law and site characteristics from these earthquakes. Correspondingly, there are many light-moderate earthquakes (Ms 4–5.9) with wide geographical distribution. With the development of observation technology, many light-moderate earthquakes have been recorded, and rich ground motion data have been accumulated all over the world. Using light-moderate earthquakes can comprehensively clarify the regional site characteristics and reveal the correlation between ground motion characteristics and disasters in a wider range. Meanwhile, light-moderate

earthquakes also induced many disasters in history. For example, in 1995, an earthquake with magnitude of Ms 5.8 occurred at Yongdeng, Gansu province, China. Ten people died in the earthquake, which was mainly caused by the loess landslides [7]. A Ms 5.2 earthquake with shallow source depth occurred in Minxian-Zhangxian, Gansu province, China on November 13, 2003. In the earthquake, one person died and 26 people were injured, 3344 houses collapsed, and 3052 buildings became dangerous [8]. Relative studies to light-moderate earthquakes have been performed. A series of moderate earthquakes (M 5.8–6.5) in western Gulf greatly impacted the marine sedimentary [9]. The dynamical process of ionosphere following a moderate magnitude earthquake ($M \approx 5.9$) has been studied [10]. Ground motion prediction equation was proposed to assess the probabilistic seismic hazard in low-to-moderate seismic areas [11]. The characteristics of soil radon (Rn-222) during a series of moderate earthquakes (M 4.5–5.8) were clarified [12]. In low-to-moderate earthquake areas, non-uniform Timoshenko beam models have been used to assess the seismic performance of buildings [13]. As for the investigation about ground motion and regional site characteristics, and the relationship with seismic geological disasters using light-moderate earthquakes is insufficient.

Seismic ground motion analysis enables us to know the natural characteristics of earthquakes and the stratum conditions. It is the base for further geotechnical disaster prevention, seismic design of structures, and seismological research. Time domain analysis of signals can reflect the characteristics of amplitude with time and the attenuation law and attenuation model of amplitude. However, frequency information of signal cannot be clarified. Fourier transform is widely used in seismic signal or ambient vibration [14, 15]; however, it is only suitable for linear and stationary data analysis in theory. The seismic wave triggered by an earthquake is a kind of sudden event, which can be regarded as a nonlinear and nonstationary process, which makes it difficult to apply the seismic signal processing technology based on the traditional linear stationary system theory. Hilbert-Huang transform (HHT) can be used for nonlinear and nonstationary data analysis, which developed rapidly in recent years and is used in many fields [16–20]. Especially in mining engineering, the structure and rock mass under different stress state show different spectral characteristics during failure process [21–25].

For the record of microtremors, HVSR methods were often used to evaluate the site effects. The method is based on two assumptions [26]: 1. The vertical and horizontal values (amplitude and spectrum components) on the bedrock are equivalent; 2. The soil layer has a significant impact on the horizontal vibration, while it has little impact on the vertical vibration in the frequency components. It represents the transfer function of the surface horizontal component to the bedrock horizontal component, and the reference site is no longer needed. Studies [27] verified that the HVSR of light-moderate earthquake records can identify the amplification effect of the site, at least its resonance frequency domain. Later, this method was extended to analyze seismic response of nonlinear sites. Lermo & Chavez Garcia (1993) [28] analyzed the transfer functions of three sites in different cities in Mexico. The results of HVSR are very close to the transfer function obtained directly from the records. It shows that the predominant period and local amplification level of simple geological conditions can be obtained by the method. Bonilla, F. et al. [27] used direct S-wave, coda, and HVSR to estimate the site amplification effect in San Fernando Valley, California. The results show that the dominant period of site effect estimated by HVSR is the same as that calculated by direct S-wave and coda method, but the amplification effect is smaller. For microtremors or near-field vibration of light-moderate earthquakes, hypothesis 1 may be acceptable, but it is impossible for large earthquakes, especially for far-field nonlinear response in large earthquakes [29]. It reflects that site characteristics can be evaluated based on light-moderate earthquakes using HVSR method.

We chose two light-moderate earthquakes with magnitude Ms 5.0 and Ms 4.9 that occurred in loess area of China as study cases and investigated the spectrum characteristics of them based on HHT method in the study. First, all the seismic waves recorded by different strong motion stations that in different site conditions and epicenter distances were performed baseline correction. Second, the seismic waves were decomposed into a series of Intrinsic Mode Functions (IMFs) through Empirical mode decomposition (EMD) and each of them satisfied the hypothesis of Hilbert transform. Third, the correlation coefficients between IMFs and original signal were calculated, and the seismic signals were reconstructed by eliminating the IMFs that have low correlation with the original signal. Forth, Hilbert transform was performed on the reconstructed signal. Then, the Hilbert-Huang spectrum, marginal spectrum, and instantaneous energy spectrum of each seismic wave were obtained. We analyzed the three types of spectrums of light-moderate earthquakes and clarified the characteristics of them from time-frequency domain. At last, the site characteristics are discussed based on the coda wave of the light-moderate earthquakes using HVSR method.

2. Case Study

Light-moderate earthquakes (Ms 4–5.9) frequently occurred in Gansu Province, China. More than 119 light-moderate earthquakes occur in loess area of China from June 1, 1980 to October 28, 2019, which include 96 earthquakes with magnitude Ms 4–4.9 and 23 earthquakes with magnitude Ms 5–5.9. This study chose two typical light-moderate earthquake events in the area as study cases.

The locations of epicenter of two earthquakes and the strong motion stations were shown in Figure 1. The elevation of the area changed from 1224 m to 5218 m. Many faults distributed in this area such as Yumushan, Minle-Damaying, Huangcheng-Shuangta, Lenglongling, and Longshoushan. So, earthquakes frequently occur in this area. A Ms 5.0 earthquake with source depth about 11 km occurred on September 16, 2019. In the study area, two strong motion stations which are HZH and MLE recorded this event, as it is shown in Figure 1. Another Ms 4.9 earthquake with source depth about 16 km also occurred on May 11, 2012. In the

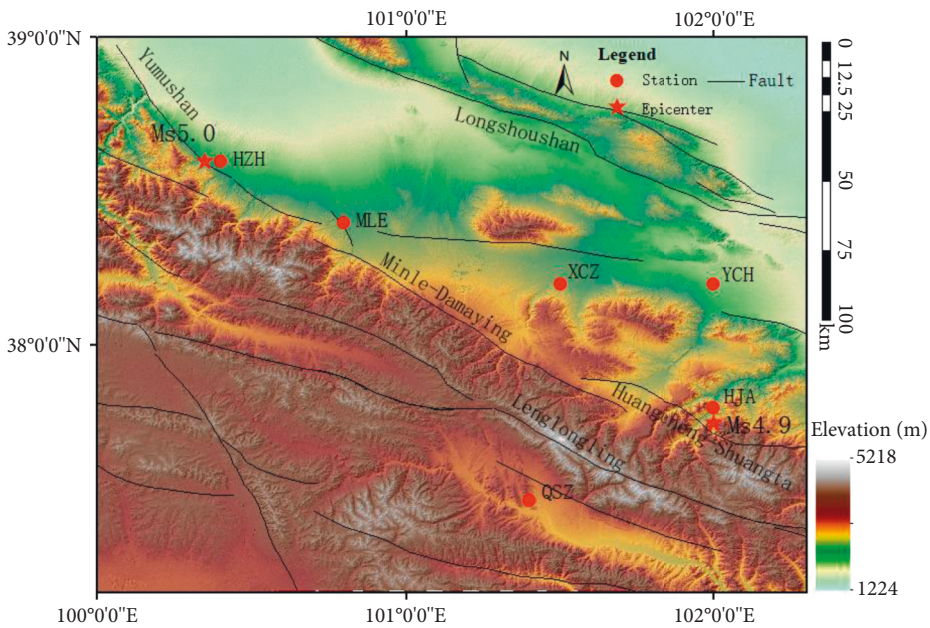

Figure 1: Study area and location of epicentral and strong motion stations.

area, four strong motion stations recorded the event, which are HJA, XCZ, YCH, and QSZ. The location, elevation, and epicenter distance of each strong motion station was shown in Table 1. It shows that HZH and HJA stations are about 2.4 km and 5.7 km away from the epicenter of Ms 5.0 and Ms 4.9, respectively, which can reflect many meaningful natural information of the two earthquake events. Among these stations, QSZ is on the rock site and with epicenter distance close to YCH and XCZ which are on soil sites. So, it can reflect the effect of site conditions on the ground motions.

3. Method

HHT is composed of two parts which are EMD and Hilbert Transform [17]. First, the signal is processed by EMD to obtain a series of IMFs, and each order of IMF can satisfy the hypothesis of Hilbert transform; Second, each order of IMF is to perform Hilbert transform to obtain Hilbert-Huang spectrum, Hilbert marginal spectrum, and instantaneous energy spectrum.

According to the theory of EMD, every time history of signal X(t) can be decomposed into n IMFs with frequency from high to low and a $r(t)$, as it is shown in:

$$x(t) = \sum_{i=1}^{n} IMF_i(t) + r(t), \tag{1}$$

where IMF_1, IMF_2, IMF_3 ... are the Intrinsic Mode Functions of different frequencies from high to low; r (t) is residual.

Based on EMD, the intrinsic mode functions of seismic waves recorded by HZH-EW were obtained, as shown in Figure 2. The duration of original signal is 76.87 s. Peak value 71.573 cm/s^2 occurred at 23.56 s. The seismic wave was decomposed into 10 IMF with frequency from high to low and a residual. From IMF1 to IMF10, the amplitude gradually decreases, and IMF1-5 contain the most of amplitude of the original seismic wave.

In the IMFs, some low frequency components are generated by numerical error and do not have any effects on the original signal. In order to acquire the useful components, the threshold of each signal was established [30]. The calculation method of threshold value ρ for extracting useful signals was shown in (2). When $\mu_i \geq \rho$, the former IMF_i were retained, and the remaining IMF were eliminated [17].

$$\rho = \frac{\max(\mu_i)}{10\max(\mu_i) - 3}, \quad i = 1, 2 \ldots n, \tag{2}$$

where μ_i represents the correlation coefficient of the IMF_i to the original signal; n is total number of IMFs.

The correlation coefficients were shown in Figure 3. The threshold of intrinsic mode functions of seismic waves recorded by HZH-EW is 0.16 according to the calculation method mentioned in (2). The correlation coefficients of IMF1-5 greater than threshold, which were retained. The correlation coefficients of IMF6-10 close to 0, which were eliminated. The IMF2 has the most correlation with original signal and the correlation coefficient up to 0.8. Then, the reconstructed signal composed by IMF1-5 was used to make Hilbert transfer.

After the original signals were decomposed by EMD and extracted the useful components, the instantaneous frequency corresponding to each of IMF_i is calculated by Hilbert transform. Hibert-Huang spectrum is obtained. As it is shown in:

$$H(t, w) = \sum_{i=1}^{n} a_i(t, w_i), \tag{3}$$

where ω_i (t) is the instantaneous frequency corresponding to each of IMF_i; $a_i(t, w_i)$ is the amplitude corresponding to ω_i (t) of the IMF_i at certain a time t; H (t, ω) is time-frequency distribution of the amplitude of the whole signal.

Table 1: Details about each strong motion station.

Magnitude	Epicenter	Strong motion stations	Location	Epicentral distance (km)	Elevation (m)	Site condition
Ms 5.0	100.35 E, 38.6 N	HZH	100.4 E, 38.6 N	2.4	2186	Soil
		MLE	100.8 E, 38.4 N	38.42	2383	Soil
Ms 4.9	102 E, 37.75 N	HJA	102 E, 37.8 N	5.7	2774	Soil
		YCH	102 E, 38.2 N	50.25	2011	Soil
		QSZ	101.4 E, 37.5 N	59.81	3085	Rock
		XCZ	101.5 E, 38.2 N	66.5	2511	Soil

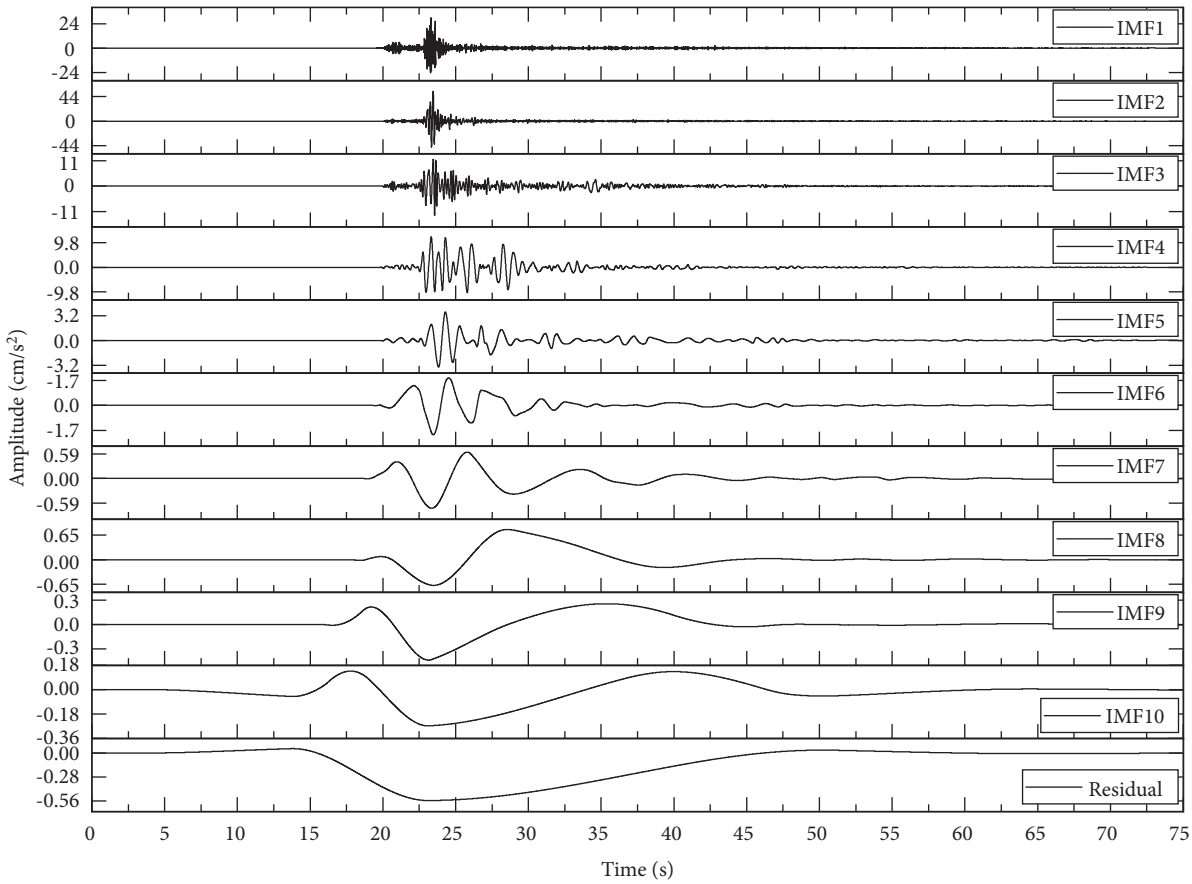

Figure 2: Intrinsic mode functions (IMFs) of HZH-EW.

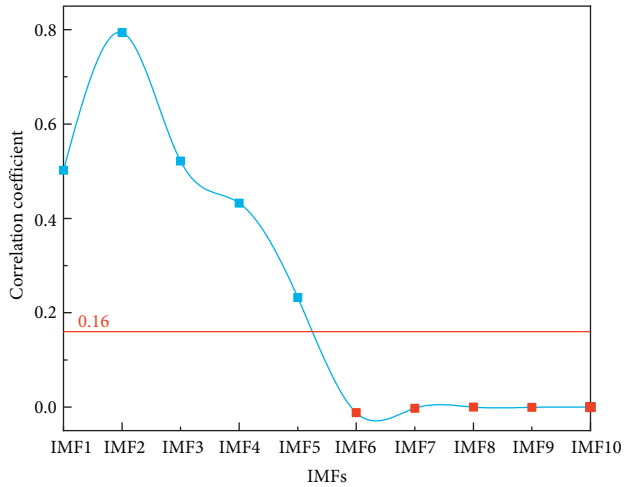

Figure 3: Correlation coefficient distribution.

The Hilbert marginal spectrum is shown in:

$$h(w) = \int_0^T H(t, w)\mathrm{d}t. \quad (4)$$

The instantaneous energy spectrum is acquired by integrating the $H^2(t, w)$ in frequency. As it shows in:

$$IE(t) = \int_w H^2(t, w)\mathrm{d}w. \quad (5)$$

All the seismic waves were performed baseline correction at first in this study. The calculation process of the HHT is implemented based on MATLAB software.

4. Results

4.1. Spectrum Characteristics of Strong Motion

4.1.1. Hilbert-Huang Spectrum Characteristics. Hilbert-Huang spectrums of seismic waves recorded by station HZH, MLE, HJA, XCZ, YCH, and QSZ were shown in Figures 4 and 5 respectively. Every station records the seismic wave with three directions and we just list the results of EW and NS directions for the amplitude of UD direction is much smaller than EW and NS directions. In the Hilbert-Huang spectrum, the relationship among time, frequency, and energy can be obtained. The amplitude of the spectrum represents the energy of instantaneous frequency.

The Hilbert-Huang spectrums of seismic waves of Ms 5.0 recorded by two strong motion stations were shown in Figure 4. Results show that the Hilbert-Huang spectrums of two stations with different epicenter distances show totally different characteristics and the distribution has certain similarity at the same station in different directions. The spectrum of HZH-EW shows that the energy concentrated at 20–30 s and instantaneous frequency concentrated within 20 Hz. Compared with HZH-EW, the energy of HZH-NS also concentrated at 20–30 s and instantaneous concentrated within 20 Hz, but peak value gradually shifts to relative high frequency (close to 20 Hz). The spectrum of MLE-EW shows that the energy widely distributed at 15–40 s and instantaneous frequency distributed within 40 Hz. Similarly, the energy of seismic wave which recorded by MLE-NS also distributed within 40 Hz. Except for the distribution characteristics, the amplitudes of two stations also have quite a difference. The peak energy of HZH-EW is about 62.3 cm/s^2 and HZH-NS is about 41.2 cm/s^2; however, the energy of MLE-EW is 4.6 cm/s^2, and MLE-NS is 4.0 cm/s^2. The peak amplitude of HZH-NS is about 10 times greater than MLE-NS and the HZH-EW is more than 10 times greater than MLE-EW, which reflect that the energy of seismic wave will changes from concentration to divergence in time and frequency and gradually decreases with the increase of epicenter distance.

The Hilbert-Huang spectrums of Ms 4.9 were shown in Figure 5. The spectrums of HJA-EW and HJA-NS show that the energy concentrated at 20–25 s and instantaneous frequency concentrated within 20 Hz. The peak amplitude of HJA-EW is about 30 cm/s^2 and the peak value of HJA-NS is about 25 cm/s^2. The location of YCH has the same longitude as HJA and lower elevation than HJA. The energy of seismic wave at YCH station is distributed within 10–40 s and with instantaneous frequency within 30 Hz. The peak values are 4.5 cm/s^2 and 5.2 cm/s^2 in the directions of EW and NS, respectively. Compared with the HJA, energy at YCH is more scattered and the peak value decreases about 5 times, which reflects that seismic energy attenuates with the epicenter distance increasing. The distribution of energy at station XCZ is more scattered compared with other stations and the peak amplitudes are 3.12 cm/s^2 and 2.60 cm/s^2, respectively, which are smaller than YCH, because the epicenter distance of XCZ is more far than YCH. The energy of seismic wave recorded by QSZ is concentrated at 20–25 s, the instantaneous frequency is concentrated within 20 Hz, and the peak amplitude are 1.5 cm/s^2 and 1.58 cm/s^2 in the directions of EW and NS, respectively. The epicenter distance of QSZ is between YCH and XCZ, whereas the energy of it is very concentrated compared with YCH and XCZ and the energy is smallest among them. This is because the site condition of QSZ station is rock, which is different from others. The results reflect that site conditions can significantly influence the distribution characteristics of instantaneous frequency energy. The energy of a seismic wave is more divergent in the soil than it is in the rock in the process of seismic wave propagation, the distribution characteristics of instantaneous frequency energy are closer to epicenter compared to the soil site condition, and the soil layer can greatly amplify the instantaneous frequency energy.

4.1.2. Marginal Spectrum Characteristics. Marginal spectrum reflects the distribution law of Hilbert energy with frequency. Hilbert energy Marginal spectrum is different from Fourier spectrum. Marginal spectrum is based on the HHT and its frequency is a function of time. So, the frequency in marginal spectrum may not necessarily appear in the whole period, but at a certain time or several times [31].

The marginal spectrums of Ms 5.0 and Ms 4.9 seismic waves at different strong motion stations were shown in Figures 6(a) and 6(b), respectively. Result shows that the shapes of marginal spectrum in N-S and E-W directions are similar with each other at each station and Hilbert energy of frequency mainly distributed within 20 Hz. Peak Hilbert energy of HZH-NS is about 23.9 and the energy is about 4.0 at MLE-NS, which reflects that peak amplitude of HZH-NS is about 6.6 times greater than MLE-NS. Peak amplitudes of HZH-NS and MLE-NS occurred at 1.125 Hz. Peak amplitudes of HZH-EW and MLE-EW occurred at 1.625 Hz and 1.375 Hz, respectively, and peak amplitude of HZH-EW is about 6.03 times greater than MLE-EW. Hilbert energy of Ms 5.0 seismic waves shows a downward trend with the increase of epicenter distance and presents low prominent frequency characteristics. The energy of HJA, XCZ, YCH, and QSZ also mainly distributed within 20 Hz and the predominant frequency was within 1.075–2.45 Hz which shows low prominent frequency characteristic. The peak Hilbert energy of HJA, YCH, QSZ, and XCZ are 5.8, 4.7, 0.59, and 0.65, respectively, which shows a decreasing trend with the increase of epicenter distance except for QSZ. Result

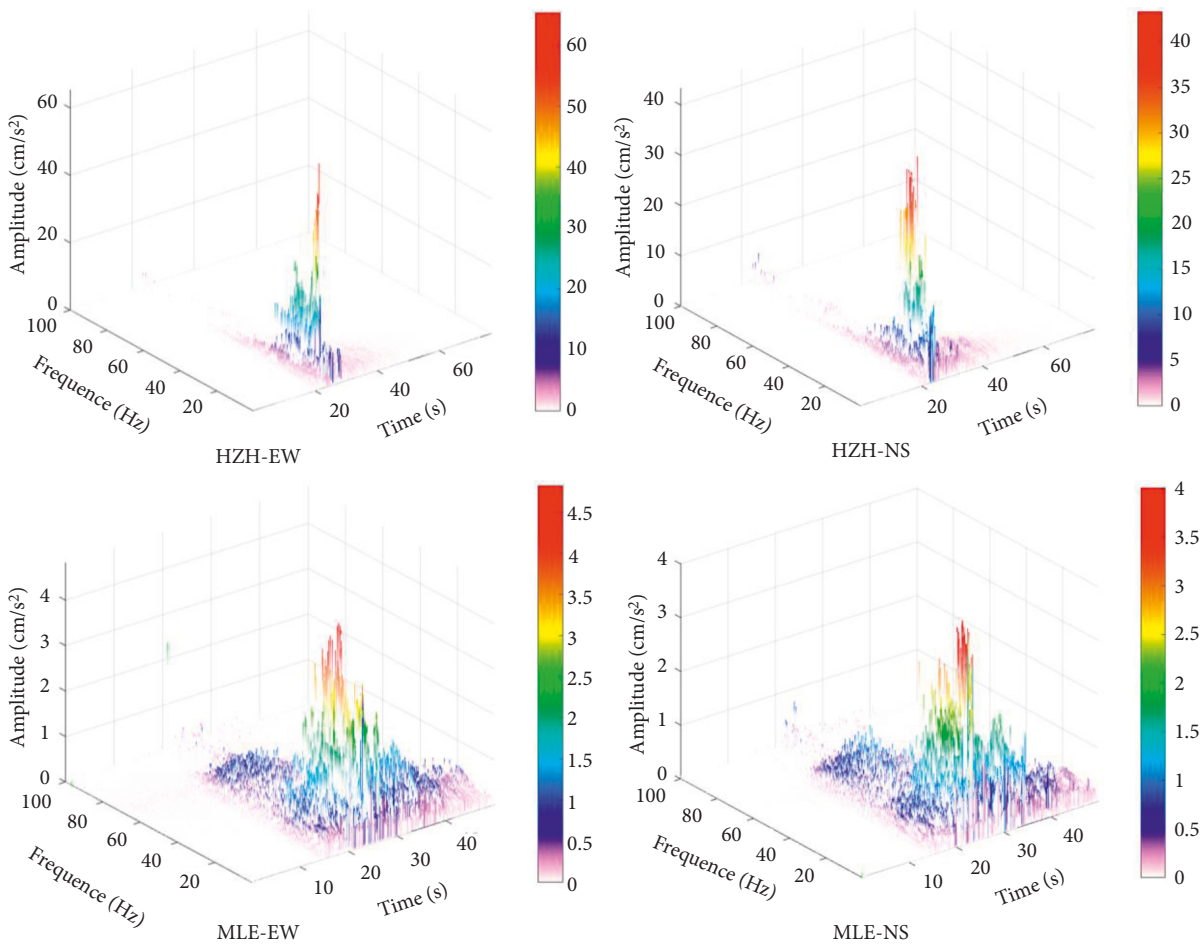

Figure 4: Hilbert-Huang spectrum of the reconstructed signal of HZH and MLE.

shows that the epicenter distance of XCZ is larger than QSZ, whereas the peak value is greater than QSZ. This result is related to the site conditions of two stations, which reflects that soil layer can greatly amplify the Hilbert energy of an earthquake. The result is consistent with the result of Hilbert-Huang spectrum.

Above results show that the prominent frequencies of the seismic waves of two earthquakes present low frequency (1.125–1.625 Hz and 1.075–2.45 Hz, respectively), the Hilbert energy shows a decreasing trend with the increase of epicenter distance, and the loess layer can amplify the Hilbert energy.

4.1.3. Instantaneous Energy Spectrum Characteristics. Instantaneous energy is an energy corresponding to time, which can reflect the instantaneous energy fluctuation of earthquakes in the whole duration.

Instantaneous energy spectrums of different strong motion stations were shown in Figure 7. Result shows that the instantaneous energy at HZH is concentrated within 20–30 s and the amplitude of two directions up to maximum value at the same time. The instantaneous energy of MLE distributed within 15–40 s and the time that amplitude of MLE-EW up to maximum is before MLE-NS. The peak amplitudes of HZH and MLE in EW direction are 7.45×10^5 and 6.45×10^3, respectively, which are about 1.6–1.7 times greater than it in NS direction. The peak value of instantaneous energy of HZH is larger than that of MLE, which reflects that the instantaneous energy attenuates quickly with the increase of epicenter distance. The instantaneous energy of HJA concentrated within 20–25 s and the amplitude in two directions up to peak is also at the same time. The peak value of HJA-EW is 2.4×10^5, which is about 1.67 times larger than HJA-NS which is about 1.6×10^5. The instantaneous energy of XCZ is distributed within 10–40 s and the time that amplitude of two directions up to maximum is same. The peak value of XCZ-EW is about 1.36 times greater than XCZ-NS. The instantaneous energy of YCH is distributed within 20–50 s and the time that peak amplitude of YCH-EW and YCH-NS occurred is different. The results show that the peak amplitude of NS direction is larger than EW at YCH. The instantaneous energy of QSZ is concentrated within 20–30 s and the time that peak amplitude of QSZ-EW and QSZ-NS occurred is different. The peak value of QSZ-NS is about 2.3 times larger than QSZ-EW. The results reflect that distribution characteristics of instantaneous energy spectrum in two directions are not unified. The peak value of EW is larger than NS at HJA and XCZ, but the value has the opposite characteristics at YCH and QSZ. The

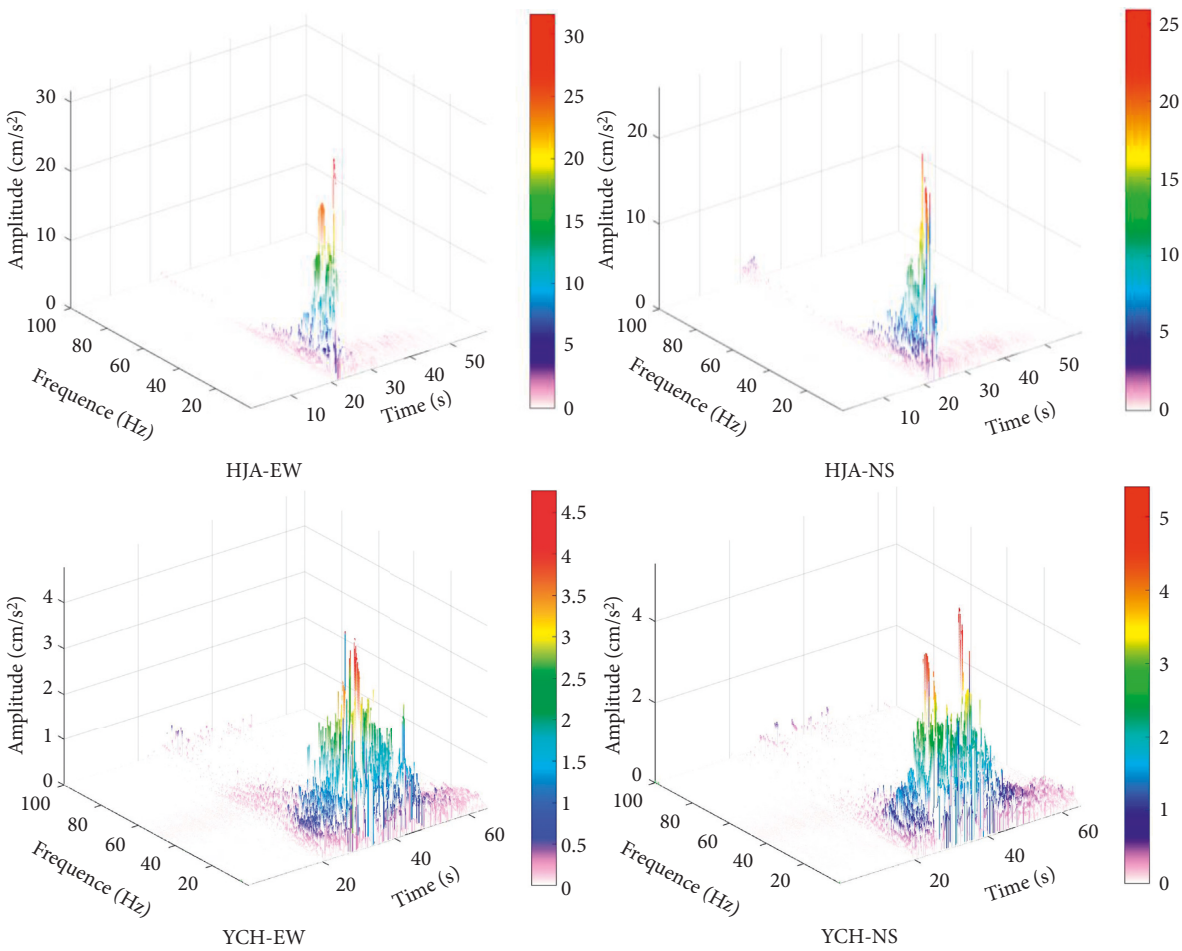

(a)

Figure 5: Continued.

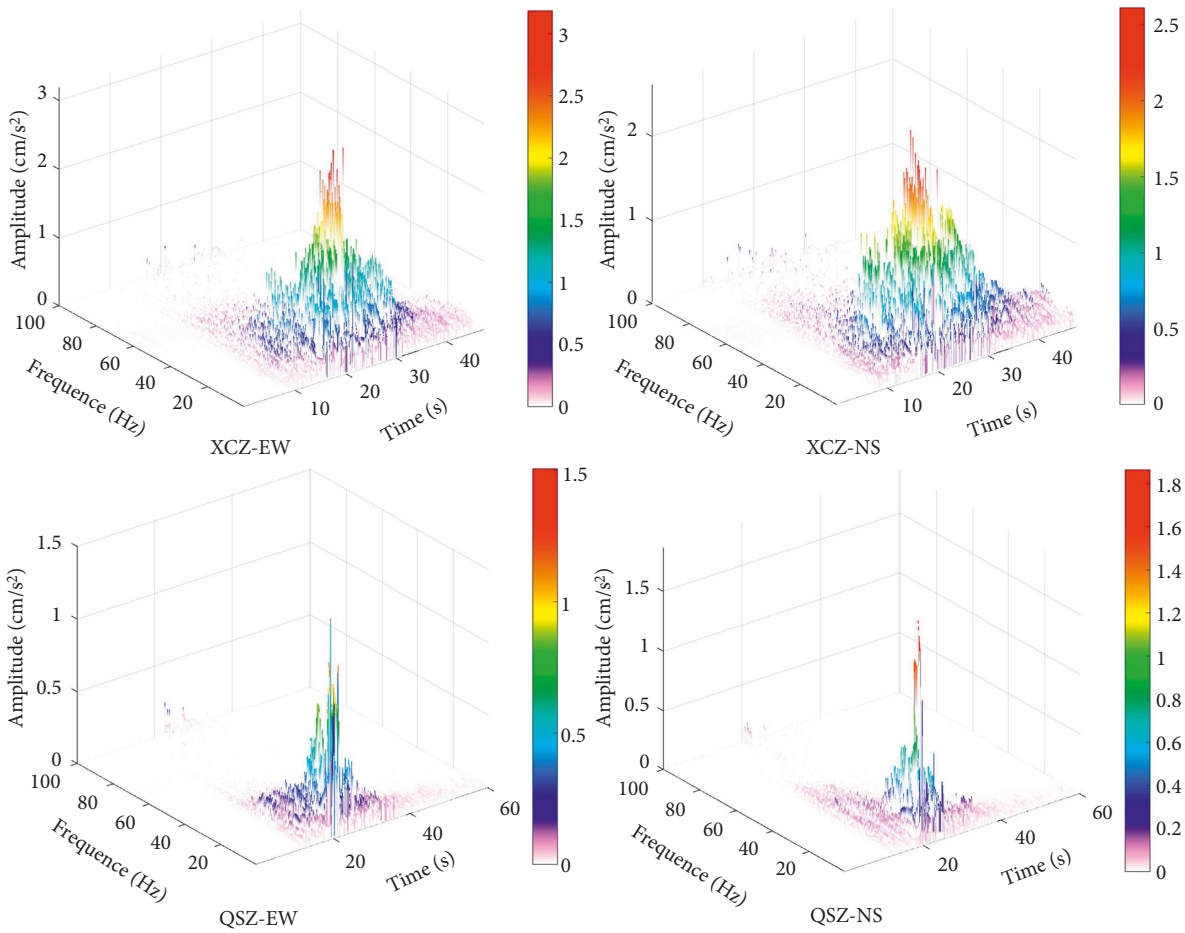

(b)

Figure 5: Hilbert-Huang spectrum of the reconstructed signal of HJA, YCH, XCZ, and QSZ.

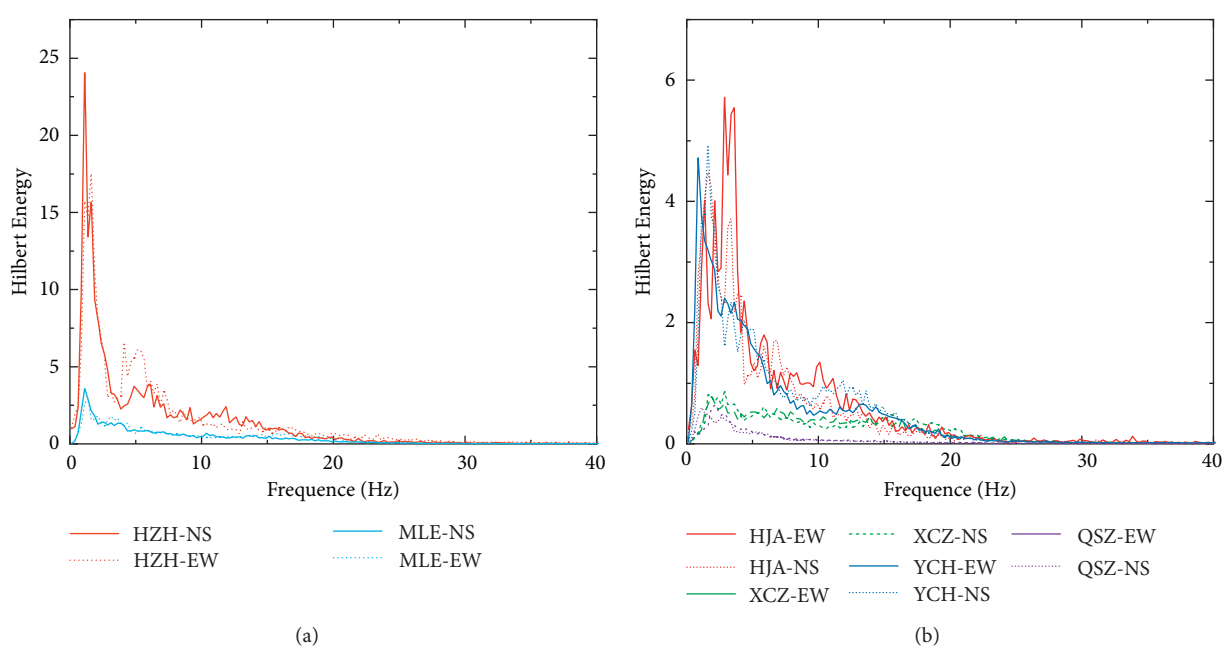

(a) (b)

Figure 6: Marginal spectrum of each strong motion station. (a) Ms 5.0 (b) Ms 4.9.

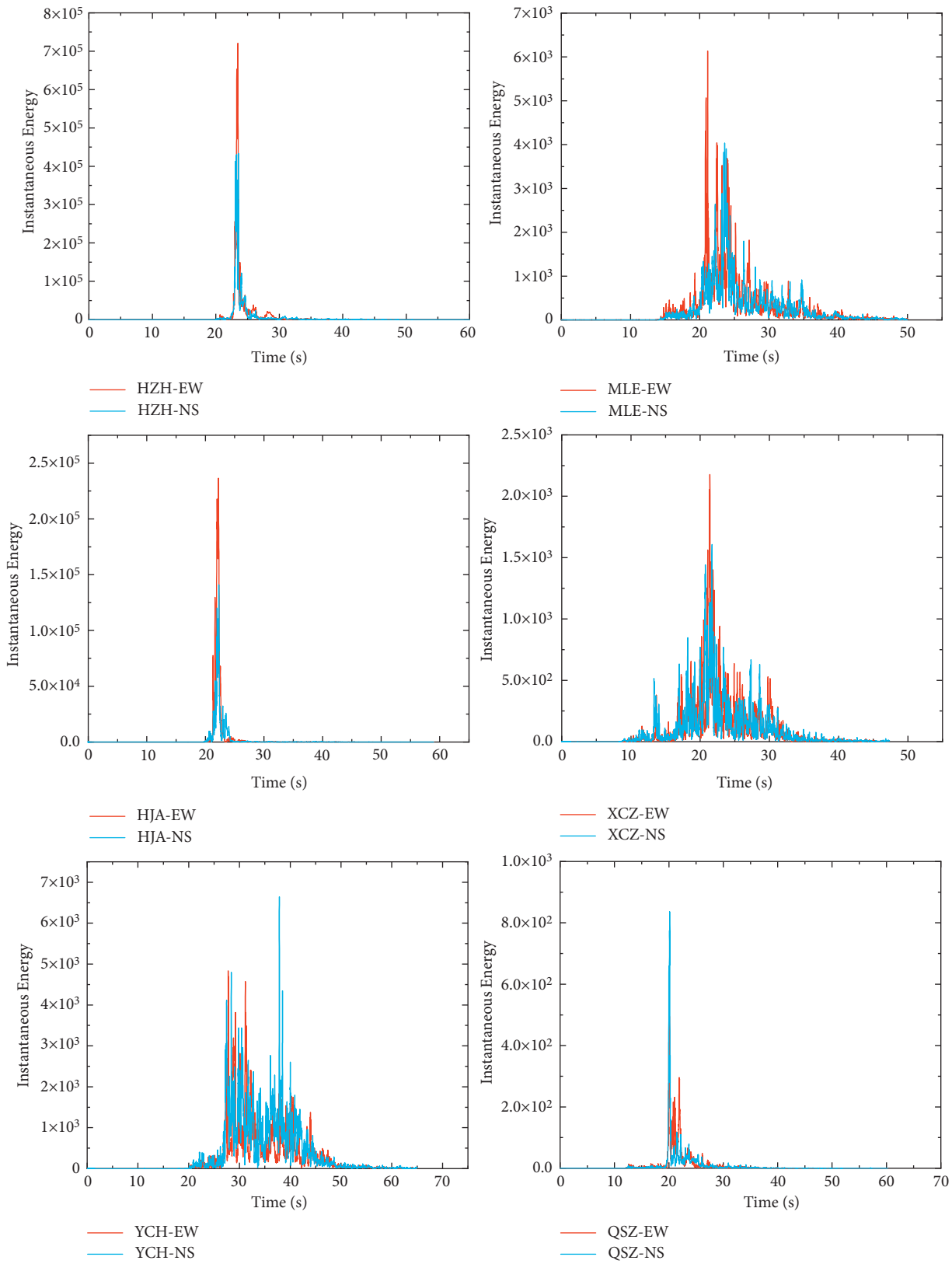

Figure 7: Instantaneous energy spectrum of each strong motion station.

instantaneous energy at QSZ is smaller than XCZ or YCH. This result shows that soil layer can amplify the instantaneous energy.

4.2. Site Characteristics. The HVSR method was often used to investigate the site effect [32]. Similarly, we used horizontal to vertical marginal spectrum ratio based on coda wave to study the site characteristics, because the marginal spectrum can reflect the frequency components more clearly than the Fourier spectrum. The calculation is shown in:

$$R(f) = \frac{H(f)}{V(f)}, \tag{6}$$

where $H(f)$ is the marginal spectrum of horizontal ground motion, $V(f)$ is the marginal spectrum of vertical ground motion.

The time history of seismic wave includes source, propagation path, and site information. Coda wave is a superposition of discontinuous scattered waves formed by the scattering of seismic waves on a nonuniform body in the Earth medium [33]. The generation of coda is related to the incompleteness elasticity, inhomogeneity, and anisotropy of the Earth medium, so coda contains a lot of information about the source and medium. So, coda wave analysis is better than the whole time history of ground motion to obtain the characteristics of the medium. Rautian [34] pointed out that $t >> ts$ (ts is the arrival time of S wave from the time of earthquake occurrence) is the starting point of the coda wave. The starting point and length of coda wave do not have a unified selection method. We select the last 20 s of ground motion as the coda wave in this study, as shown in Figure 8.

The HVSR results based on coda wave using marginal spectrum and the contour map of HVSR in study area are shown in Figures 9 and 10 respectively. It reflects that the predominant frequency of site at each station is within 3.6–6.2 Hz. Although the data are limited, the site characteristics are obvious. The amplification factor (H/V) at rock site (QSZ) is 2, which is minimum among all stations. The factor reaches maximum at HZH which is soil site. The factors at other sites are within 3–5.2. Because of the lack of soil layer thickness data, relationship between the factor and soil layer thickness cannot be discussed further. However, it clearly reflects that soil layer can amplify the ground motion when compared with a rock site. So, HVSR based on coda wave of light-moderate earthquakes using marginal spectrum can be used to investigate the site effect.

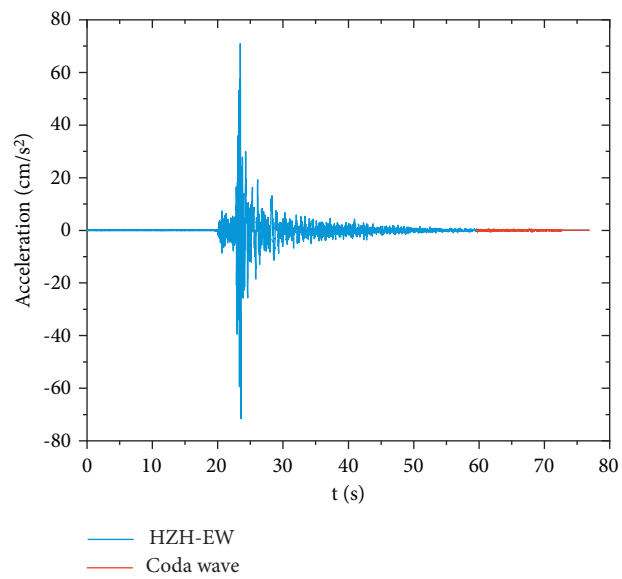

Figure 8: Coda wave.

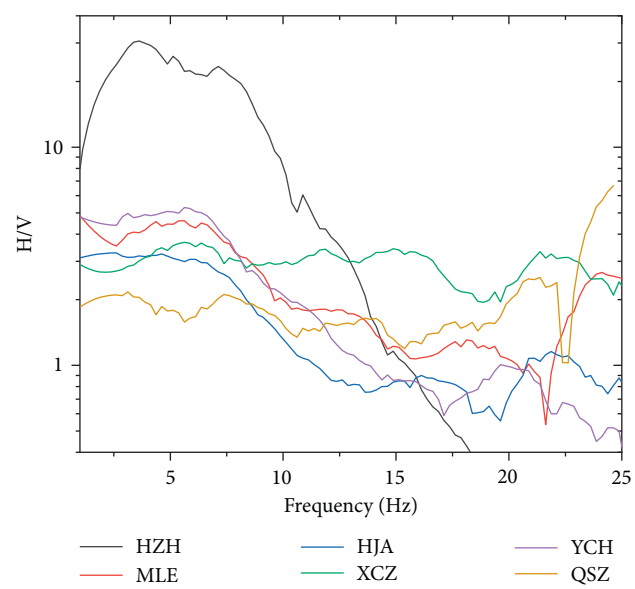

Figure 9: HVSR result based on coda wave using marginal spectrum.

5. Discussion

5.1. Comparison of Predominant Frequency of Ground Motion and Site. The severity of disasters caused by earthquakes is not only related to earthquake intensity but also closely related to ground motion and site characteristics. Site characteristics are related to landform, soil type, soil thickness, stratum structure, and so on. The predominant frequency of site is the comprehensive reflection of these factors. When the predominant frequency of site is close to the seismic ground motion, the resonance effect would be produced and the disaster would also be more serious. Figure 11 presents the HVSR results of HZH and HJA stations and the marginal spectrum of two light-moderate earthquakes in the study. It reflects that the predominant frequencies of the earthquakes are in the low frequency range, which are lower than the predominant frequencies of sites. So, the disasters induced by the two earthquakes are minor.

5.2. Comparison of Fourier Spectrum and Marginal Spectrum. The frequency characteristics of two light-moderate earthquakes in this study are clearly according to the Hilbert-Huang spectrum and marginal spectrum based on HHT.

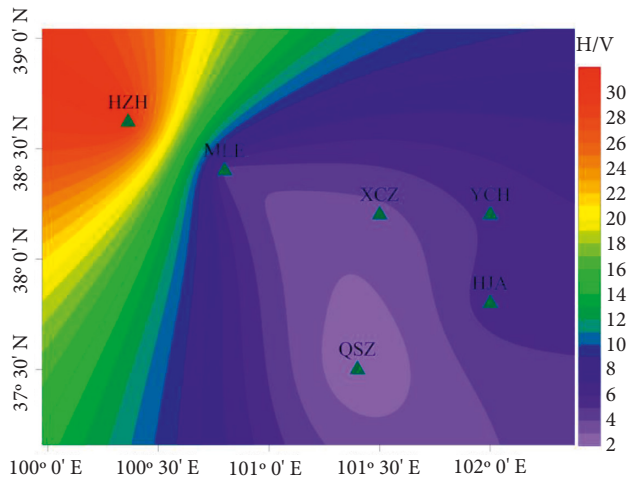

Figure 10: Contour map of HVSR in study area.

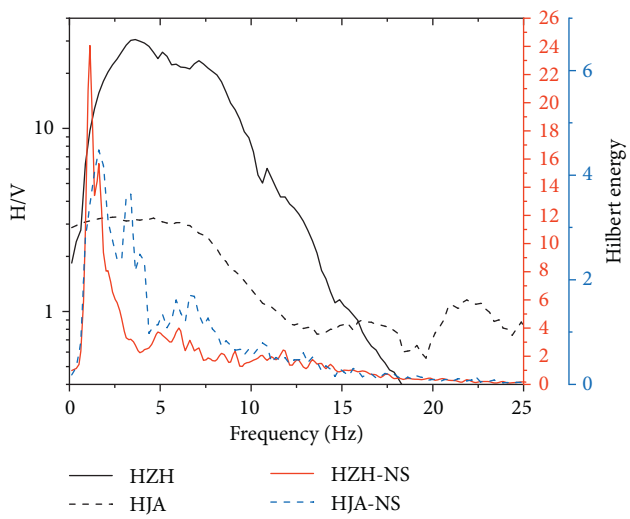

Figure 11: Marginal spectrum and HVSR results.

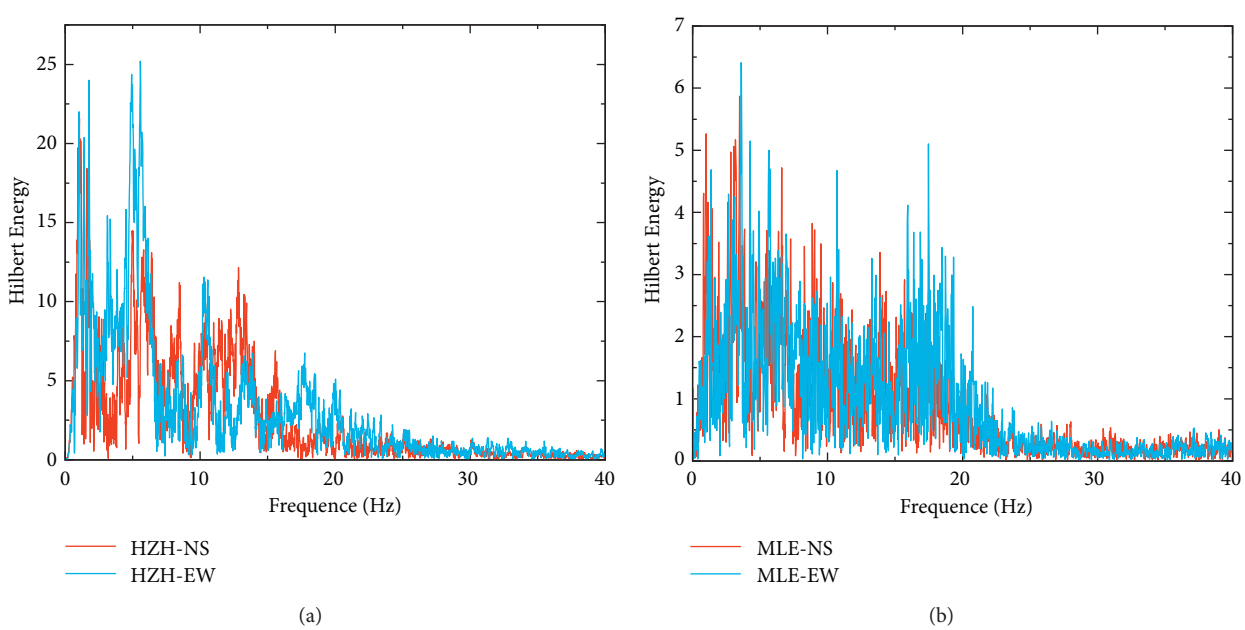

Figure 12: Fourier spectrum of Ms 5.0 earthquake. (a) HZH (b) MLE.

Generally, we use FFT to clarify the frequency characteristics. However, FFT applicable to linear and stationary signal analysis, which cannot present the frequency features of seismic waves for the earthquake signal is nonlinear and nonstationary. In order to clear that, we performed FFT on the seismic waves of Ms 5.0, as it is shown in Figure 12. The prominent frequency of HZH is within 0–8 Hz and the prominent frequency of MLE is within 0–20 Hz. Compared with marginal spectrum that is shown in Figure 6 Fourier spectrum cannot reflect the predominant frequency clearly and the low frequency energy is not well presented. So, HHT is better than FFT in the frequency analysis of seismic waves, which gives a direction for future relative studies.

6. Conclusions

In the study, we analyzed the spectrum characteristics of two light-moderate earthquakes that occurred in loess area of China from time-frequency domain based on HHT and the site characteristics based on the coda wave of the earthquakes using HVSR method. The main conclusions are shown as follows:

(1) Hilbert-Huang spectrum based on HHT can clearly reflect the relationship among time, frequency, and amplitude (instantaneous frequency energy) of seismic waves of light-moderate earthquakes. The energy of seismic wave at strong motion station that close to epicenter is mainly concentrated within 20 Hz. With the increase of epicenter distance, the energy will change from concentration to divergence in time and frequency and gradually decrease at same site condition. In the process of propagation, the energy of a seismic wave is more concentrated under the rock site condition than it under the soil site situation and a loess layer can amplify the energy.

(2) The marginal spectrum distinctly shows the accumulation of energy of light-moderate earthquake in time. Two earthquakes present low prominent frequency characteristics. Peak amplitude of Ms 5.0 earthquake in two directions occurred within 1.125–1.625 Hz, and the value of Ms 4.9 earthquake is within 1.075–2.45 Hz, respectively. With the increase of epicenter distance, Hilbert energy shows a downward trend. The Hilbert energy at soil site is about 3 times greater than at rock site when the epicenter distance is close, which suggests that soil layer can greatly amplify the Hilbert energy of an earthquake.

(3) Instantaneous energy spectrum shows the change law of instantaneous energy of light-moderate earthquakes with time. Instantaneous energy attenuates quickly with the increase of epicenter distance. Site conditions greatly impact on the characteristics of instantaneous energy. Instantaneous energy at the rock site is much smaller than at soil site, which reflects that soil layer can significantly amplify the instantaneous energy of an earthquake.

(4) HVSR based on coda wave of light-moderate earthquakes using marginal spectrum can be used to investigate the site characteristics. The predominant frequency of site at each station is within 3.6–6.2 Hz. Compared with a rock site, soil layer can amplify the ground motion. The amplification factor at rock site is minimum with value 2 and the factor reaches 30.2 at HZH which is soil site.

Data Availability

Basic data can be obtained from the corresponding author upon request.

Conflicts of Interest

The authors declare that they have no conflicts of interest.

Acknowledgments

Data for this study are provided by the Institute of Engineering Mechanics, China Earthquake Administration. This research work was financially supported by the Key Project of National Natural Science Foundation of China (No. U1939209).

References

[1] S. L. Kramer and M. W. Smith, "Modified Newmark model for seismic displacements of compliant slopes," *Journal of Geotechnical and Geoenvironmental Engineering*, vol. 123, no. 7, pp. 635–644, 1997.

[2] R. D. Borcherdt, "Estimates of site dependent response spectra for design (methodology and justification)," *Earthquake Spectra*, vol. 10, no. 4, pp. 617–653, 1994.

[3] T. I. Allen and D. J. Wald, "On the use of high-resolution topographic data as a proxy for seismic site conditions (VS30)," *Bulletin of the Seismological Society of America*, vol. 99, no. 2A, pp. 935–943, 2009.

[4] Y. Gao, Z. L. Wu, Z. Liu, and H. Zhou, "Seismic source characteristics of nine strong earthquakes from 1988 to 1990 and earthquake activity since 1970 in the sichuan-qinghai-xizang (tibet) zone of China," *Pure and Applied Geophysics*, vol. 157, no. 9, pp. 1423–1443, 2000.

[5] V. M. Smirnov, E. V. Smirnova, M. N. Tsidilina, and M. V. Gaponova, "Seismo-ionospheric variations during strong earthquakes based on the example of the 2010 earthquake in Chile," *Cosmic Research*, vol. 56, no. 4, pp. 267–275, 2018.

[6] S. T. Akopian, "Detection of features of the strong earthquake of march 25, 2020, east of the kuril islands using the seismic entropy method," *Seismic Instruments*, vol. 56, no. 5, pp. 620–631, 2020.

[7] Lanzhou Institute of Seismology, *Catalogue of strong Earthquakes in Shaanxi, Gansu, Ningxia and Qinghai Provinces (1177 BC-1982),* Shaanxi Science and Technology Press, Xian, China, 1985.

[8] X. Y. Du and S. L. Huang, "Risk factors of earthquake and the management of its secondary disasters," *Journal of Catastrophology*, vol. 23, pp. 71–74, 2008.

[9] A. Beckers, C. Beck, A. F. Hubert et al., "Sedimentary impacts of recent moderate earthquakes from the shelves to the basin

floor in the western Gulf of Corinth," *Marine Geology*, vol. 384, pp. 81–102, 2017.

[10] Q. Guo, L. F. Chernogor, K.-P. Garmash, V. Rozumenko, and Y. Zheng, "Dynamical processes in the ionosphere following the moderate earthquake in Japan on 7 July 2018," *Journal of Atmospheric and Solar-Terrestrial Physics*, vol. 186, pp. 88–103, 2019.

[11] D. Bindi, F. Cotton, S. R. Kotha, C. Bosse, D. Stromeyer, and G. Grunthal, "Application-driven ground motion prediction equation for seismic hazard assessments in non-cratonic moderate-seismicity areas," *Journal of Seismology*, vol. 21, no. 5, pp. 1201–1218, 2017.

[12] V. Shukla, V. Chauhan, N. Kumar, and D. Hazarika, "Assessment of Rn-222 continuous time series for the identification of anomalous changes during moderate earthquakes of the Garhwal Himalaya," *Applied Radiation and Isotopes*, vol. 166, Article ID 109327, 2020.

[13] R. K. L. Su, T. O. Tang, and K. C. Liu, "Simplified seismic assessment of buildings using non-uniform Timoshenko beam model in low-to-moderate seismicity regions," *Engineering Structures*, vol. 120, pp. 116–132, 2016.

[14] Q. J. Chen, W. Z. Yuan, Y. C. Li, and Ly Cao, "Dynamic response characteristics of super high-rise buildings subjected to long-period ground motions," *Journal of Central South University*, vol. 20, no. 5, pp. 1341–1353, 2013.

[15] M. G. Tian and W. J. Yi, "Dynamic behavior of reinforced concrete frame structure during construction," *Journal of Central South University of Technology*, vol. 15, no. 3, pp. 418–422, 2008.

[16] N. E. Huang, Z. Shen, S. R. Long et al., "The empirical mode decomposition and the Hilbert spectrum for nonlinear and non-stationary time series analysis," *Proceedings of the Royal Society of London. Series A: Mathematical, Physical and Engineering Sciences*, vol. 454, no. 1971, pp. 903–995, 1998.

[17] J. C. Chen, L. M. Wang, P. Wang, and A. L. Che, "Failure mechanism investigation on loess–mudstone landslides based on the Hilbert–Huang transform method using a large-scale shaking table test," *Engineering Geology*, vol. 302, Article ID 106630, 2022.

[18] S. R. Garcia, M. P. Romo, and L. Alcántara, "Analysis of nonlinear and non-stationary seismic recordings of Mexico City," *Soil Dynamics and Earthquake Engineering*, vol. 127, Article ID 105859, 2019.

[19] D. Q. Song, X. L. Liu, J. Huang, and J. M. Zhang, "Energy-based analysis of seismic failure mechanism of a rock slope with discontinuities using Hilbert-Huang transform and marginal spectrum in the time-frequency domain," *Landslides*, vol. 18, no. 1, pp. 105–123, 2021.

[20] G. Fan, J. J. Zhang, J. B. Wu, and K. M. Yan, "Dynamic response and dynamic failure mode of a weak intercalated rock slope using a shaking table," *Rock Mechanics and Rock Engineering*, vol. 49, no. 8, pp. 3243–3256, 2016.

[21] X. L. Li, S. J. Chen, S. Liu, and Z. H. Li, "AE waveform characteristics of rock mass under uniaxial loading based on Hilbert-Huang transform," *Journal of Central South University*, vol. 28, no. 6, pp. 1843–1856, 2021.

[22] S. M. Liu, X. L. Li, and D. K. Wang, "Investigations on the mechanism of the microstructural evolution of different coal ranks under liquid nitrogen cold soaking," *Energy Sources, Part A: Recovery, Utilization, and Environmental Effects*, pp. 1–17, 2020.

[23] X. L. Li, S. J. Chen, Q. M. Zhang, X. Gao, and F. Feng, "Research on theory, simulation and measurement of stress behavior under regenerated roof condition," *Geomechanics and Engineering*, vol. 26, no. 1, pp. 49–61, 2021.

[24] X. L. Li, S. J. Chen, S. Wang, M. Zhao, and H. Liu, "Study on in situ stress distribution law of the deep mine taking Linyi Mining area as an example," *Advances in Materials Science and Engineering*, vol. 2021, no. 4, pp. 1–11, Article ID 5594181, 2021.

[25] H. Y. Liu, B. Y. Zhang, X. L. Li et al., "Research on roof damage mechanism and control technology of gob-side entry retaining under close distance gob," *Engineering Failure Analysis*, vol. 138, no. 5, Article ID 106331, 2022.

[26] Y. Nakmura, "A method for dynamic characteristics estimation of subsurface using microtremor on the ground surface," *Quarterly Report of RTRI*, vol. 30, no. 1, pp. 25–33, 1989.

[27] L. F. Bonilla, J. H. Steidl, G. T. Lindley, A. G. Tumarkin, and R. J. Archuleta, "Site amplification in the San Fernando Valley, California: variability of Site-effect estimation using the s-wave, coda, and H/V methods," *Bulletin of the Seismological Society of America*, vol. 87, no. 3, pp. 710–730, 1997.

[28] J. Lermo and F. J. C. García, "Site effect evaluation using spectral ratios with only one station," *Bulletin of the Seismological Society of America*, vol. 83, no. 5, pp. 1574–1594, 1993.

[29] X. J. Li, "Thoughts on the research of earthquake damage phenomenon and engineering earthquake in recent years," *International earthquake dynamics*, vol. 8, pp. 26–31, 2001.

[30] A. Ayenu and N. A. Attoh, "Criterion for selecting relevant intrinsic mode functions in empirical mode decomposition," *Advances in Adaptive Data Analysis*, vol. 02, no. 01, pp. 1–24, 2010.

[31] H.-X. Liu, Q. Xu, X. Zhu, X. P. Zhou, and W. D. Liu, "Marginal spectrum characteristics of the rock slope with a soft interlayer during an earthquake," *Rock and Soil Mechanics*, vol. 40, no. 4, pp. 1387–1396, 2019.

[32] L. Agostini, J. Boaga, A. Galgaro, and A. Ninfo, "HVSR technique in near-surface thermal-basin characterization: the example of the Caldiero district (North-East Italy)," *Environmental Earth Sciences*, vol. 74, no. 2, pp. 1199–1210, 2015.

[33] K. Aki, "Analysis of the seismic coda of local earthquakes as scattered waves," *Journal of Geophysical Research*, vol. 74, no. 2, pp. 615–631, 1969.

[34] T. G. Rautian and V. I. Khalturin, "The use of the coda for determination of the earthquake source spectrum," *Bulletin of the Seismological Society of America*, vol. 68, no. 4, pp. 923–948, 1978.

Hindawi
Shock and Vibration
Volume 2022, Article ID 8232065, 20 pages
https://doi.org/10.1155/2022/8232065

Research Article

Seismic Signal-Based Investigation on the Disaster Differences between 2021 Yangbi Ms 6.4 Earthquake and 2014 Ms 6.5 Ludian Earthquake in Yunnan Province, China

Jinchang Chen,[1] Ailan Che,[1] Lanmin Wang,[1,2] and Lixin Jiang[3]

[1]*School of Naval Architecture, Ocean and Civil Engineering, Shanghai Jiao Tong University, Shanghai 200040, China*
[2]*Lanzhou Institute of Seismology, China Earthquake Administration, Lanzhou 730000, China*
[3]*China Earthquake Networks Center, Beijing 100045, China*

Correspondence should be addressed to Ailan Che; alche@sjtu.edu.cn

Received 11 April 2022; Revised 25 June 2022; Accepted 7 July 2022; Published 1 August 2022

Academic Editor: Annalisa Greco

An Ms 6.4 earthquake occurred in Yangbi County, Yunnan Province, on May 21, 2021. The magnitude is only 0.1 difference when compared with the 2014 Ms 6.5 earthquake in Ludian County, Yunnan Province, but the disasters show a big difference. Seismic signal includes the comprehensive information of source, propagation path, and site effect, which directly reflect the effect of the earthquake on the ground. The study mainly investigated the difference between seismic signals of two events in time domain and time-frequency-energy space based on variational mode decomposition and Hilbert transform to clarify the reasons for disaster differences. Most damaged buildings are column-and-tie timber structures with Earth walls with local collapse or vertical crack at the corner of the Earth wall in the Yangbi earthquake. Multistorey buildings are intact, and a few small landslides are triggered, whereas, in the Ludian earthquake, multistorey buildings with the frame structure and masonry structure occurred with serious X-type cracking, large interlayer displacement, and even complete collapse, and large landslides with length about 165 m are triggered. 53LLT and 53YBX are two strong motion stations in the Ludian earthquake and Yangbi earthquake, respectively, and are near the disaster investigation points. Peak ground acceleration in 53LLT is up to 949.2 cm/s^2, which is larger than 720.3 cm/s^2 in 53YBX, and the duration in 53LLT is longer than 53YBX. The instantaneous energy of 53YBX is concentrated within 0–10 Hz and 10–20 Hz, respectively; however, the instantaneous energy of 53LLT is concentrated at 5 Hz. Cumulative energy of 53YBX is mainly distributed at 0–5 Hz and 10–20 Hz, which is around the natural frequency of column-and-tie timber structure, while the energy of 53LLT is concentrated at 1.6 Hz and is much greater than other stations. Thus, large energy in high frequency caused the instantaneous and cumulative damage to short-period structures in Yangbi County and may cause the resonance of column-and-tie timber structure, and large energy in low frequency caused the instantaneous and cumulative damage to long-period structures of Longtou Village in Ludian earthquake. The result is meaningful to understanding the seismic disasters from the characteristics of seismic signals and can provide a reference for the seismic design of structures.

1. Introduction

Yunnan Province is located on the eastern edge of the collision zone between the Indian Plate and the Eurasian Plate and the southern section of the North-South Seismic Belt of China. There are 49 active faults developed in the Yunnan Province [1], with strong tectonic movement and significant seismic activity. It is one of the areas with earthquakes most active in the world [2, 3]. By 2021, 189 earthquakes of Ms 4.6 or higher than Ms 4.6 had occurred in the area, including 49 earthquakes of Ms 4.6–5.0, 107 earthquakes of Ms 5.0-6.0, and 33 earthquakes of Ms 6.0–7.8. According to the earthquake records since the 20th century, earthquakes with M 5.0~5.9 in Yunnan occur twice a year, earthquakes with M 6.0~6.9 occur twice every three years, and earthquakes with M 7 and above occur about once every eight years [4]. Large casualties and losses are caused by the frequent occurrence of earthquakes. Particularly in 2014, there were 8 destructive earthquakes with $M \geq 5.0$ in Yunnan (including 5 with M 5.0~5.9 and 3 with M 6.0~6.9), and the

economic losses, deaths, disappearances, and injuries accounted for 84.03%, 99.2%, 100%, and 97.86%, respectively, in the same period at China [5], in which most of casualties and losses are induced by the Ms 6.5 Ludian earthquake. On May 21, 2021, another destructive earthquake with a magnitude Ms 6.4 occurred in Yangbi County, Yunnan Province. The disasters present a big difference when compared with the Ludian earthquake.

Seismic signal is a vibration phenomenon that occurs when energy is suddenly released and propagated to the ground after long-term accumulation, which is the comprehensive reflection of source, propagation path, and site effect [6]. It is the starting point and essential basis of scientific research on seismology and earthquake engineering. At present, we mainly investigate the seismic signal through amplitude, duration, and spectrum. The peak ground acceleration (PGA) and the peak ground velocity (PGV) are usually used as a sign of earthquake intensity [7]. Two factors were also widely used in the structural seismic vulnerability analysis [8, 9]. However, PGA value cannot reflect the earthquake damage degree reasonably. For example, in the 1985 Mexico earthquake, the recorded PGA was only 0.17 g, which was much smaller than 0.6 g recorded in the 1986 San Salvador earthquake, but caused more serious earthquake damage [10]. Reference [11] pointed out that PGA represents the amplitude of the high-frequency component of seismic signal and has great discreteness. The experimental and case investigation show that the types of structural damage mainly include instantaneous damage and cumulative damage, and many motions with small amplitude but long duration are very destructive to the structure [12]. Therefore, seismic duration has a great impact on the cumulative damage of structures. Amplitude and duration of seismic signals are the characteristics of the time domain. Under the effect of earthquakes, the dynamic response of the structure is closely related to the spectrum characteristics of seismic signal. When the dominant frequency band is close to the natural frequency of the structure, the structural response will be significantly amplified, resulting in serious damage to the structure [13]. If the frequency of the seismic signal is concentrated in the high-frequency band, the short-period structure will cause great harm, and when the predominant frequency of the seismic signal is in the low-frequency band, it will lead to great damage to the long-period structure. In the Peru earthquake on October 17, 1966, the seismic damage in Lima City was mainly concentrated in single-storey houses, and there was little damage to multistorey houses. According to the seismic signal records of Lima City, the predominant period is nearby 0.1 s, and the natural vibration period of single-storey houses is just close to 0.1 s.

Fourier transform is widely used in the dynamic response of the structure under seismic ground motion [14, 15]. However, previous study works show that the Fourier transform is only applicable to linear and stationary data analysis [16, 17]. Compared with the Fourier transform, the Hilbert-Huang transform (HHT) can be used for nonlinear and nonstationary signal and has been widely used in analyzing seismic signals in recent years [17–20]. However, empirical mode decomposition (EMD) of HHT essentially belongs to recursive modal decomposition. The envelope estimation error is amplified by multiple recursive decomposition, which is prone to modal aliasing, and the decomposition result is greatly affected by the sampling rate [21]. Aiming at the problems of EMD, [22] proposed variational mode decomposition (VMD), which is a nonrecursive, self-adaptive, and multiresolution signal decomposition method. VMD overcomes the problems of mode aliasing and error accumulation of EMD [23, 24]. VMD combined with Hilbert transform (HT) was used in the study.

We investigated the disasters of the epicenter of the 2021 Yangbi Ms 6.4 earthquake and the 2014 Ms 6.5 Ludian earthquake at first. The disasters show a big difference, even the magnitude with only 0.1 difference. Then, we analyzed the characteristics of seismic signals in the two events from the time domain and time-frequency-energy space which is based on VMD and HT. The result of the study can help us know better about the relationship between seismic disasters and the seismic signals and provide a reference for the seismic design of structures.

2. Cases Study

2.1. Earthquake Events. An Ms 6.4 earthquake occurred in Yangbi County, Dali City, Yunnan Province (Figure 1), on May 21, 2021, with a focal depth of 8 km. It was another destructive earthquake with a magnitude greater than 6 in Yunnan Province after the Ludian Ms 6.5 earthquake, Jinggu Ms 6.6 earthquake, and Yingjiang Ms 6.1 earthquake in 2014. The seismogenic structure of the earthquake is a secondary fault on the west side of the Weixi-Qiaohou fault, which is dominated by dextral strike-slip movement [25]. Before Ms 6.4 earthquake, four earthquakes with a magnitude of Ms 4.2, Ms 5.6, Ms 4.5, and Ms 2.8 occurred successively on the same day. By June 15, 2021, there were more than 40 aftershocks with a magnitude beyond Ms 3.0 in Yangbi County, including 2 earthquakes above Ms 5.0. The largest aftershock was the Ms 5.2 earthquake (25.59°N, 99.97°E) on May 21, 2021 (43 minutes after the mainshock) [26]. Therefore, the earthquake sequence is a typical foreshock-mainshock-aftershock sequence. The earthquake caused 3 deaths, 32 injuries, 13000 damaged buildings and triggered a few small landslides. The epicenter intensity is up to VIII (China seismic intensity scale). According to the intensity map made by the Yunnan Province earthquake administration (Figure 1), the area of the VI region is about 5500 km^2, the area of the VII region is 930 km^2, and the area of the VIII region is 170 km^2. A total of 46 landslides, 6 collapses, and 7 debris flows were triggered in the earthquake. All of them have small or medium volume and are mainly distributed in the VIII and VII regions [27].

Compared with other earthquakes (Ms > 6) that occurred in Yunnan Province, especially for Ludian Ms 6.5 earthquake, the building damage degree, landslides number, casualties, and economic loss caused by the Yangbi earthquake were much less. Ludian earthquake (Figure 1) occurred on August 3, 2014; the epicenter intensity was up to IX, and the focal depth was about 12 km, which caused 617 deaths, 2400 injuries, 86000 destroyed buildings and

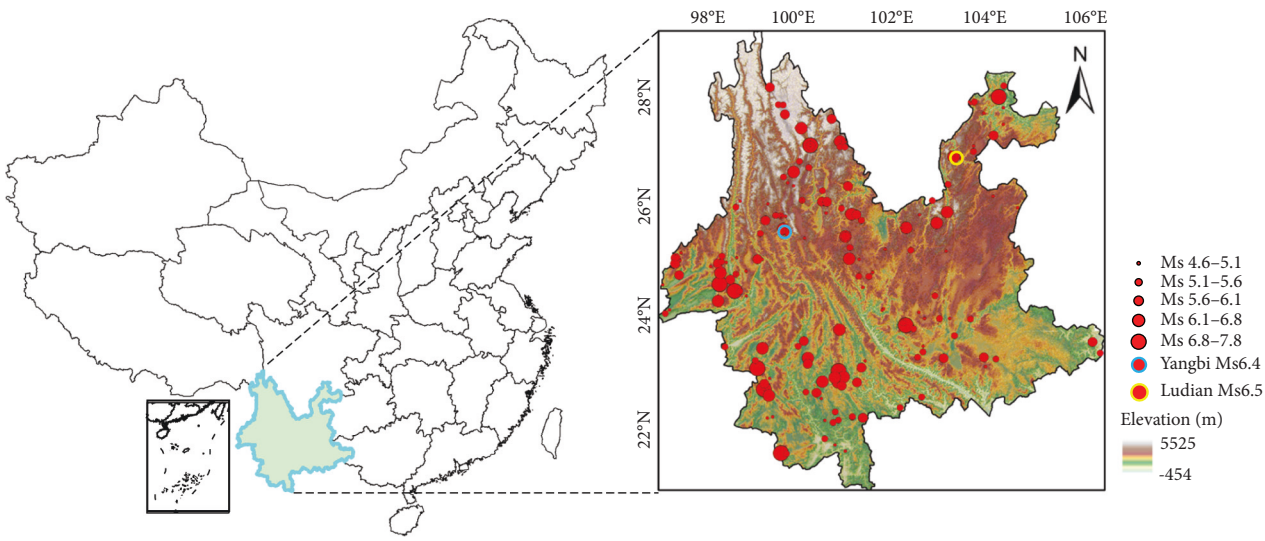

Figure 1: The location of the 2021 Yangbi and 2014 Ludian earthquakes.

triggered many large landslides [28, 29]. According to the survey data of the Department of Natural Resources of Yunnan Province, China, 986 landslides and 462 collapses were triggered. Most of them are large and huge landslides. Among them, the Hongshiyan landslide and Ganjiazhai landslide are two largest landslides with a total volume of more than 10 million m^3. Fifty-five people were buried in the Ganjiazhai landslide.

2.2. Topographic Characteristics. The elevation and slope angle shown in Figures 2 and 3 present the topography characteristics of the area within the intensity map of the Yangbi earthquake and Ludian earthquake, respectively. The elevation within the intensity map of two earthquakes changes from 1070 m to 4180 m and from 434 m to 4003 m, respectively. Figure 4(a) shows that elevation within 1500 m–2500 m in different intensity regions of two earthquakes takes the largest ratio. It takes 72.8%, 67.6%, and 99.3% in the VI region, VII region, and VIII region, respectively, for the Yangbi earthquake and takes 61.6%, 70.0%, 74.7%, and 78.9% in the VI region, VII region, VIII region, and IX region, respectively, for Ludian earthquake. The slope angle within the intensity map of two earthquakes changes from 0° to 71.98° and from 0° to 85.99°, respectively. The slope angle (Figure 4(b)) within 10–20° takes the largest ratio. Areas with a slope angle larger than 30° take 11.5%, 17.9%, and 10.6% in the VI region, VII region, and VIII region, respectively, for the Yangbi earthquake and takes 23.7%, 19.8%, 27.2%, and 30.4% in the VI region, VII region, VIII region, and IX region, respectively, for Ludian earthquake. It shows that the elevation distribution characteristics in different intensity regions of two earthquakes are close, but the slope angle larger than 30° in different intensity regions of the Ludian earthquake takes a higher ratio than that of the Yangbi earthquake.

2.3. Characteristics of Disasters. After the Yangbi Ms 6.4 earthquake, we investigated the damage degree of buildings and geotechnical disasters at Xiajie Village (in Yangbi County), Huaian Village, and Shahe Village, which are within or close to the epicenter and the 53YBX strong motion station, as it is shown in Figure 2(a). Typical seismic damage phenomenon in the Yangbi earthquake is shown in Figure 5. The structural types of buildings in the areas mainly include adobe and timber, brick and timber, and brick and concrete. Based on the investigation, we found that adobe and timber building takes the largest ratio among the damaged buildings. The damage of this structural type mainly occurred at the Earth wall, as it is shown in Figure 5. At Xiajie Village (Figure 5(a)), the Earth wall of adobe and timber structure mainly made local collapse at corner, while the brick and concrete with multistorey at Xiajie Village is stable, as it is shown in the last two pictures of Figure 5(a). At Huaian and Shahe Village (Figures 5(b)–5(c)), the Earth wall of adobe and timber structure mainly made vertical cracks at corner. At Shahe Village, a few small landslides are triggered (Figure 5(d)), which block the road.

The damaged adobe and timber buildings in the Yangbi earthquake belong to traditional Chinese column-and-tie timber structures, as shown in Figure 6. The upper load and weight of the whole roof are transmitted from rafters to purlins, then from purlins to column, and through column to the ground. Chuanfang plays an important role in connecting wooden columns and enhancing the stability of the whole frame and has little contribution to load bearing. The column is the main load-bearing member. The construction sequence of the building is as follows: the wooden column is built at first, and then the Chuanfang is used to connect the columns to establish the timber frame. On this basis, the Earth wall is built. Finally, purlin is installed, and rafters and ties are erected to complete the main construction of the building. The seismic behavior of it is poor because of lacking effective earthquake resistance measures. Its natural frequency is around 10 Hz [30].

Compared with the Yangbi earthquake, the damage phenomenon induced by the Ludian earthquake presents different characteristics. Figure 7 shows the typical seismic

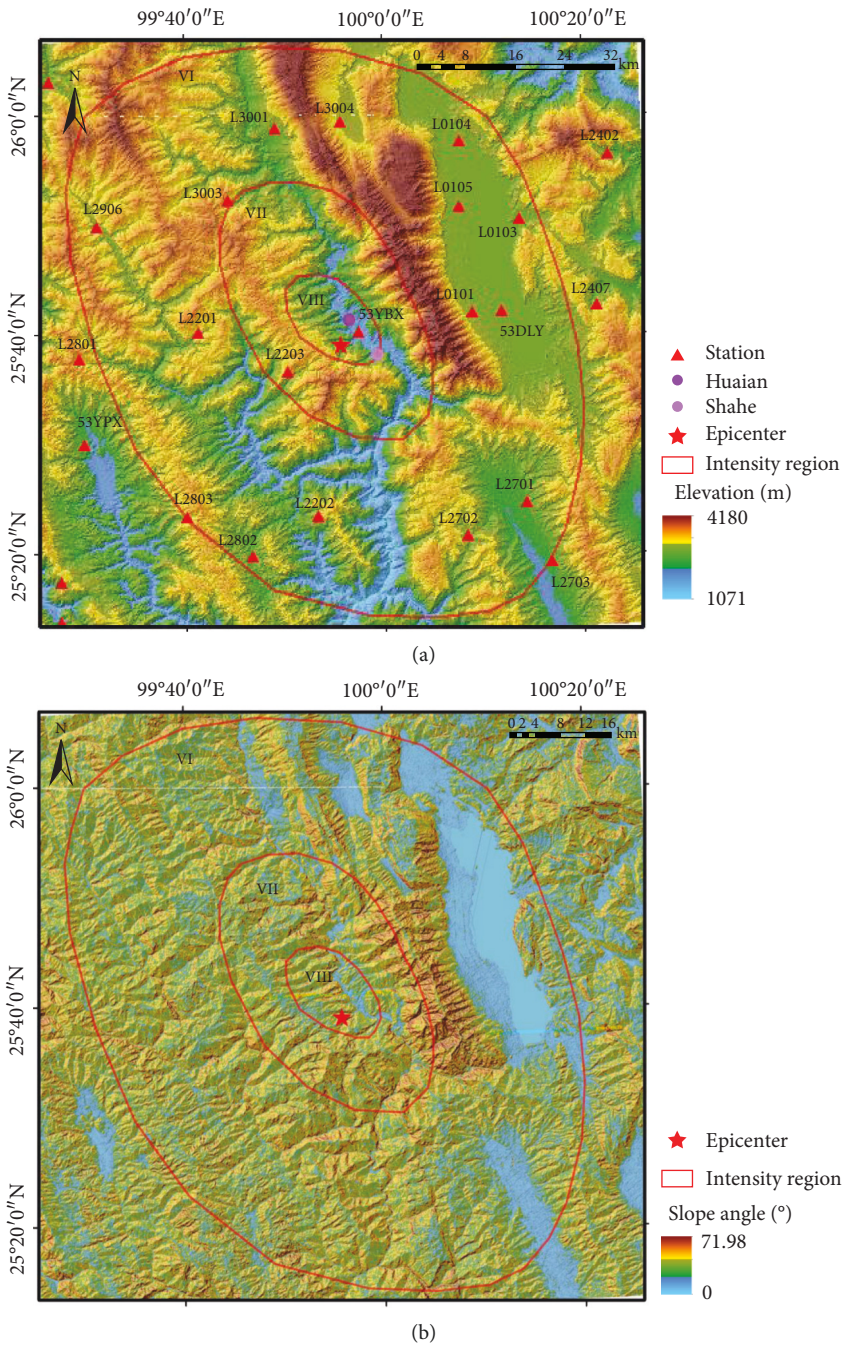

Figure 2: Distribution of elevation, slope angle, and intensity map in Yangbi earthquake. (a) Elevation and intensity map. (b) Slope angle and intensity map.

damage phenomenon in Longtou Village, which is near the 53LLT strong motion station, as it is shown in Figure 3(a). The structural types of buildings in Longtou Village mainly include frame structure, masonry structure, timber structure, and adobe and timber. In Longtou Village, frame structure and masonry structure with multistorey are seriously damaged. Figure 7(a) shows that serious X-type cracking and large interlayer displacement occurred at these buildings, and many of them even collapsed completely. Large landslides with a length of about 165 m also occurred at Longtou Village, as shown in Figure 7(b), which destroyed and buried part of the buildings. It shows that seismic damage caused by the Ludian earthquake is much more serious than the Yangbi earthquake, although the two events all occurred in Yunnan Province, and the magnitude is only 0.1 difference.

3. Data and Method

3.1. Strong Motion Data. In the Yangbi earthquake, 17 strong motion stations distributed within the intensity map record this event, including 1 in the VIII region, 1 in the VII

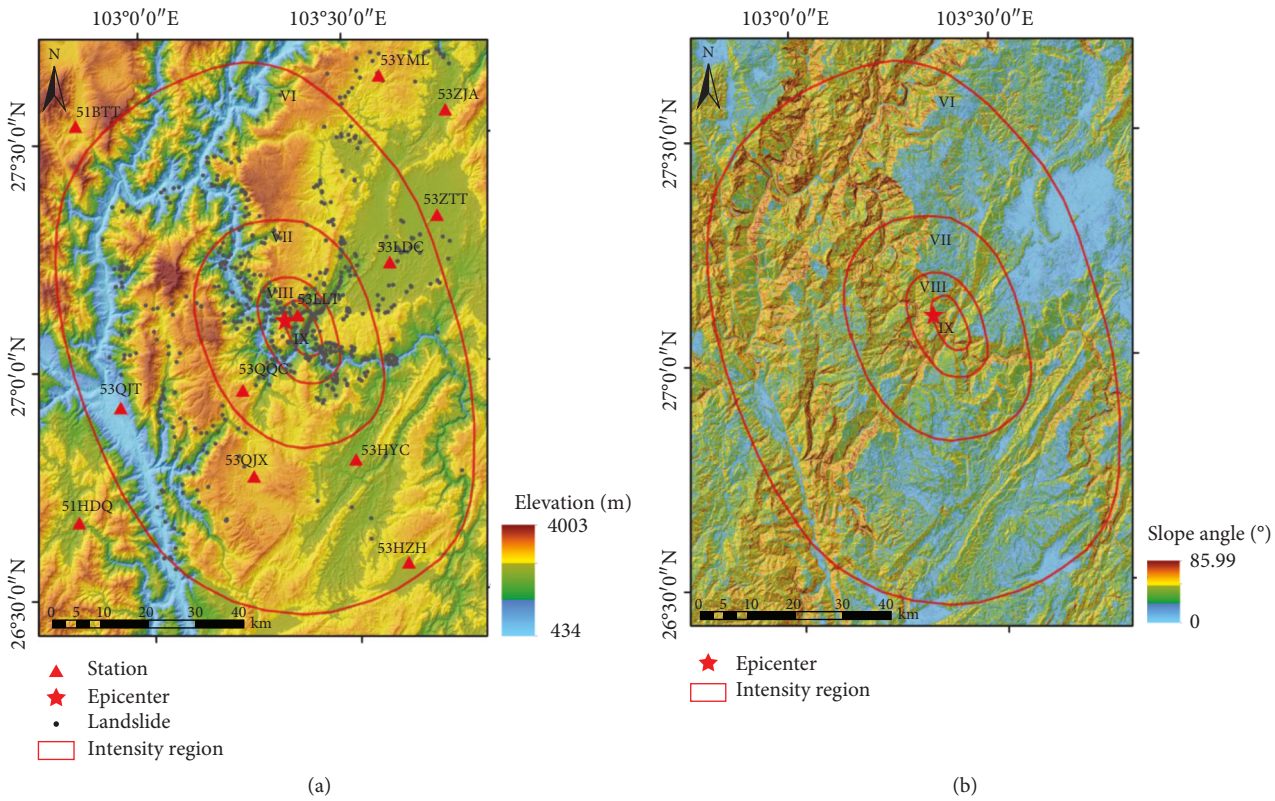

Figure 3: Distribution of elevation, slope angle, and intensity map in Ludian earthquake. (a) Elevation and intensity map. (b) Slope angle and intensity map.

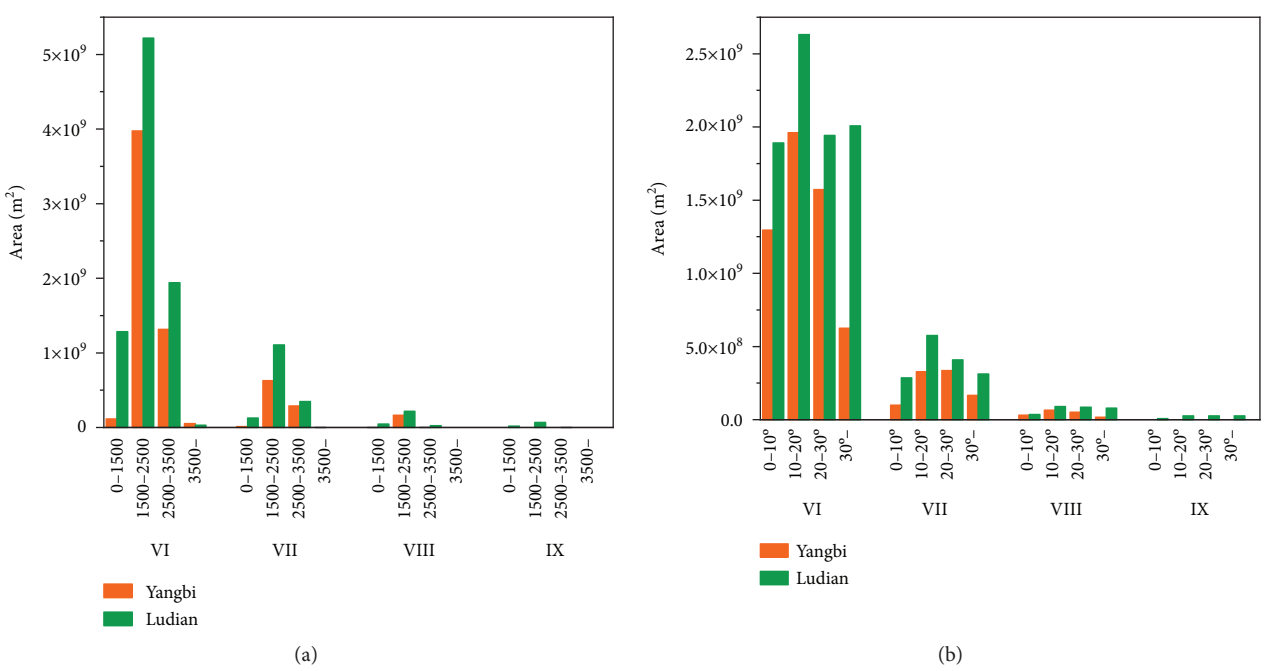

Figure 4: Distribution areas of elevation and slope angle in different intensity regions of two events. (a) Elevation. (b) Slope angle.

Figure 5: Typical seismic damage phenomenon in Yangbi Ms 6.4 earthquake. (a) Damaged buildings in Xiajie Village, Yangbi County. (b) Damaged buildings in Huaian Village. (c) Damaged buildings in Shahe Village. (d) Small landslides in Shahe Village.

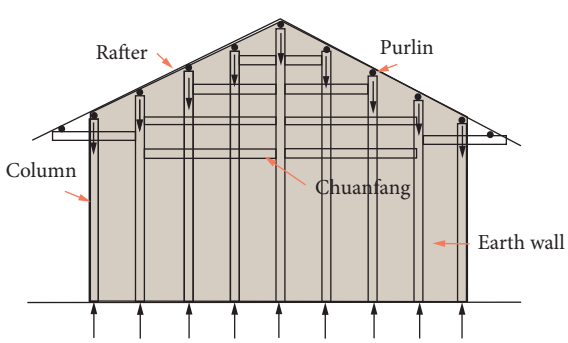

Figure 6: Column-and-tie timber structure with Earth wall.

region, and 15 in the VI region. In the Ludian earthquake, 7 strong motion stations distribute in the intensity map, including 1 in the IX region, 1 in the VII region, and 5 in the VI region. Table 1 shows the basic information of the strong motions with the epicentral distance within 40 km of two earthquakes. The 53YBX and 53LLT with an epicentral distance of around 8 km are near the disaster investigation points of two earthquakes, which give a valuable opportunity to study the disaster differences according to the characteristics of seismic signals. The baseline correction and Butterworth filter with 0.1–30 Hz bandwidth were applied to these strong motion recordings.

3.2. Method

3.2.1. Variational Mode Decomposition (VMD). The Intrinsic Mode Function (IMF) is defined as an amplitude-modulated-frequency-modulated signal, as shown in

$$u_k(t) = A_k(t)\cos(\phi_k(t)), \tag{1}$$

(a)

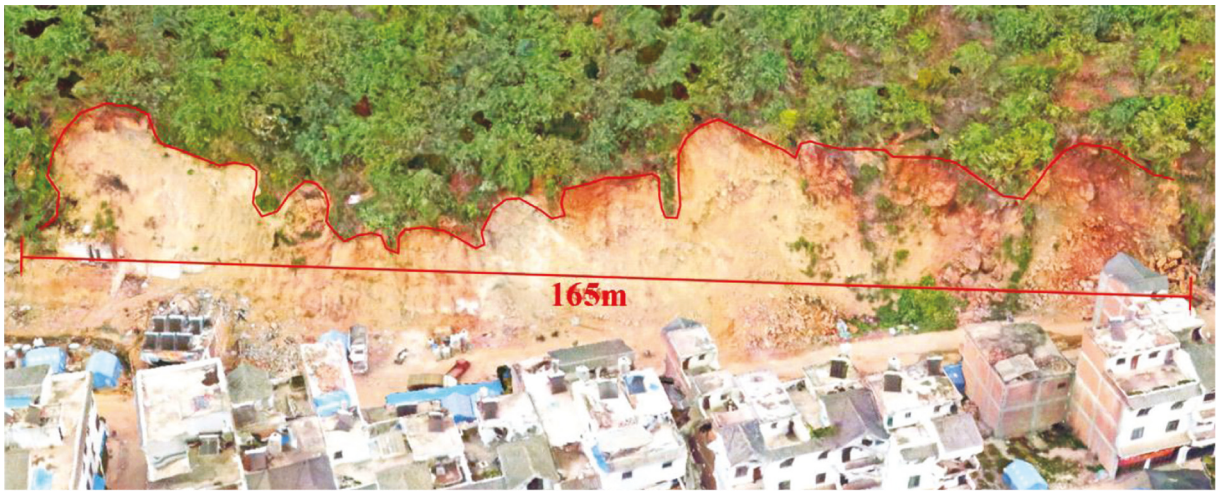

(b)

Figure 7: Typical seismic damage phenomenon in Longtou Village in Ludain Ms 6.5 earthquake. (a) Damaged buildings. (b) Landslides.

Table 1: Basic information of strong motion stations in the study.

Events	Station	Site condition	Epicentral distance (km)	Intensity scale	PGA (cm/s^2)		
					EW	NS	UD
Yangbi earthquake	53YBX	Soil	8.6	VIII	379.8	720.3	448.4
	L2203	Soil	10	VII	196.2	310.0	188.0
	L2201	Soil	16.6	VI	64.7	70.0	49.6
	L3003	Rock	25.6	VI	81.4	71.7	39.3
	L2202	Soil	30.5	VI	80.7	72.4	54.3
Ludian earthquake	53LLT	Soil	8.3	IX	949.2	−705.8	−504.4
	53QQC	Soil	18.7	VII	−146.0	−140.3	−52.8
	53LDC	Soil	32.5	VI	−45.9	44.8	−25.6
	53QJX	Soil	38	VI	135.2	−133.4	65.0
	53HYC	Rock	39.6	VI	88.3	87.7	47.5

where $\phi_k'(t) \geq 0$, $A_k(t) \geq 0$, instantaneous frequency $\omega_k(t) = \phi_k'(t)$ varies much slower than $\phi_k(t)$, and k is the number of IMFs. On the interval $[t-\delta, t+\delta]$, $\delta \approx 2\pi/\phi_k'(t)$, the mode $u_k(t)$ is a pure harmonic signal.

VMD is a process of solving the variational problem, which can minimize the sum of the estimated bandwidth of each mode. In order to estimate the bandwidth of modes, firstly, the unilateral spectrum is obtained by the Hilbert transform. Then, the modal spectrum is modulated to the fundamental frequency band by mixing the central frequency. Finally, the demodulated signal is processed by Gaussian smoothing. The constrained variational problem for estimating the bandwidth of modes is shown in the following equation:

$$\min_{\{u_k\},\{\omega_k\}} \left\{ \sum_k \left\| \partial_t \left[\left(\delta(t) + \frac{j}{\pi t} \right) * u_k(t) \right] e^{-j\omega_k t} \right\|_2^2 \right\}, \quad \sum_k u_k = f, \tag{2}$$

where $\{u_k\} = \{u_1, u_2, \ldots, u_k\}$ are the IMFs, $\{\omega_k\} = \{\omega_1, \omega_2, \ldots, \omega_k\}$ are the central frequency of each IMF, and $\delta(t)$ is the pulse function.

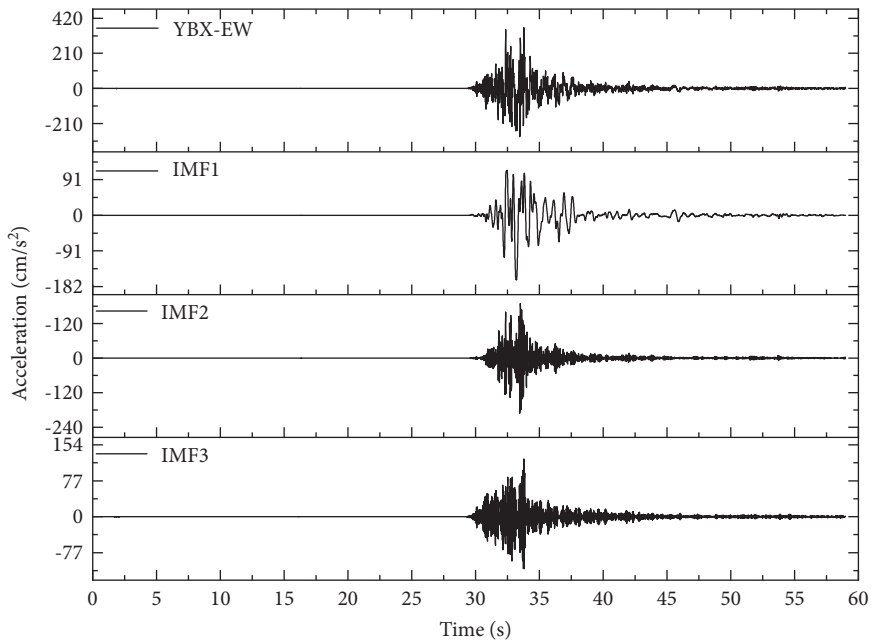

Figure 8: VMD result of the seismic signal (53YBX-EW).

The quadratic penalty term (α) and Lagrange multipliers ($\lambda(t)$) are introduced to solve the problem. The augmented Lagrangian function is as follows:

$$\mathscr{L}(\{u_k\},\{\omega_k\},\lambda) := \alpha\sum_k\left\|\partial_t\left[\left(\delta(t)+\frac{j}{\pi t}\right)*u_k(t)\right]e^{-j\omega_k t}\right\|_2^2 + \left\|f(t)-\sum_k u_k(t)\right\|_2^2 + \langle\lambda(t), f(t)-\sum_k u_k(t)\rangle. \tag{3}$$

In order to solve equation (3), Alternating Direction Method of Multipliers (ADMM) is used by iteratively updating u_k, ω_k, and λ. The specific steps are as follows: (1) $\{u_k^1\}$, $\{\omega_k^1\}$, λ^1, and n are initialized to 0; (2) $\hat{u}_k$, ω_k, and λ are iteratively updated by equations (4)–(6), respectively; (3) repeat steps (2) to (3) until the iteration termination conditions (equation (7)) are met:

$$\hat{u}_k^{n+1}(\omega) = \frac{\hat{f}(\omega)-\sum_{i\neq k}\hat{u}_i(\omega)+\hat{\lambda}(\omega)/2}{1+2\alpha(\omega-\omega_k)^2}, \tag{4}$$

$$\omega_k^{n+1} = \frac{\int_0^\infty \omega|\hat{u}_k(\omega)|^2 d\omega}{\int_0^\infty |\hat{u}_k(\omega)|^2 d\omega}, \tag{5}$$

$$\hat{\lambda}^{n+1}(\omega) = \hat{\lambda}^n(\omega)+\tau\left(\hat{f}(\omega)-\sum_k \hat{u}_k^{n+1}(\omega)\right), \tag{6}$$

$$\sum_k \frac{\|\hat{u}_k^{n+1}-\hat{u}_k^n\|_2^2}{\|\hat{u}_k^n\|_2^2} < \varepsilon, \tag{7}$$

where ε is the accuracy, $\varepsilon > 0$.

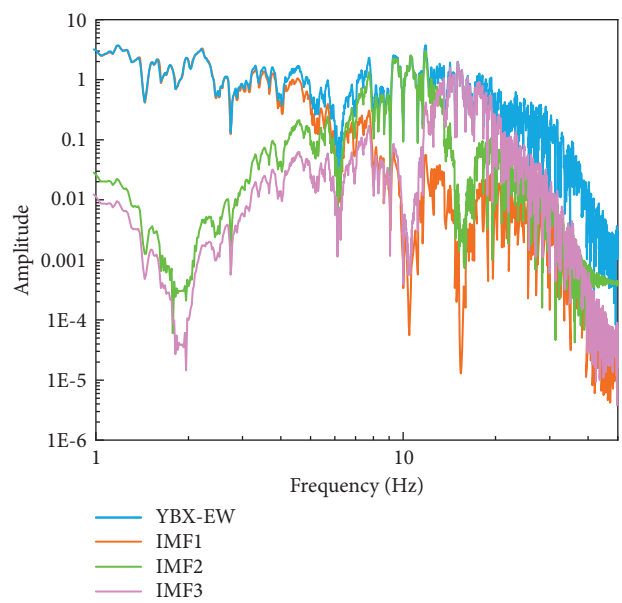

Figure 9: Fourier spectrums of the 53YBX-EW and its IMFs.

The number of IMFs is set to 3 in the study. It is taken according to the number of predominant frequencies of the Fourier spectrum. Figures 8 and 9 are the VMD result of 53YBX-EW and its Fourier spectrum, respectively. The Fourier spectrum of the original signal and its three IMFs indicates that the three predominant frequencies are around 2 Hz, 10 Hz, and 15 Hz, respectively.

3.2.2. Hilbert Transform (HT). IMF is acquired by VMD, and each of them is well behaved in the Hilbert transform. The Hilbert transform $y(t)$ is shown in the following equation [17]:

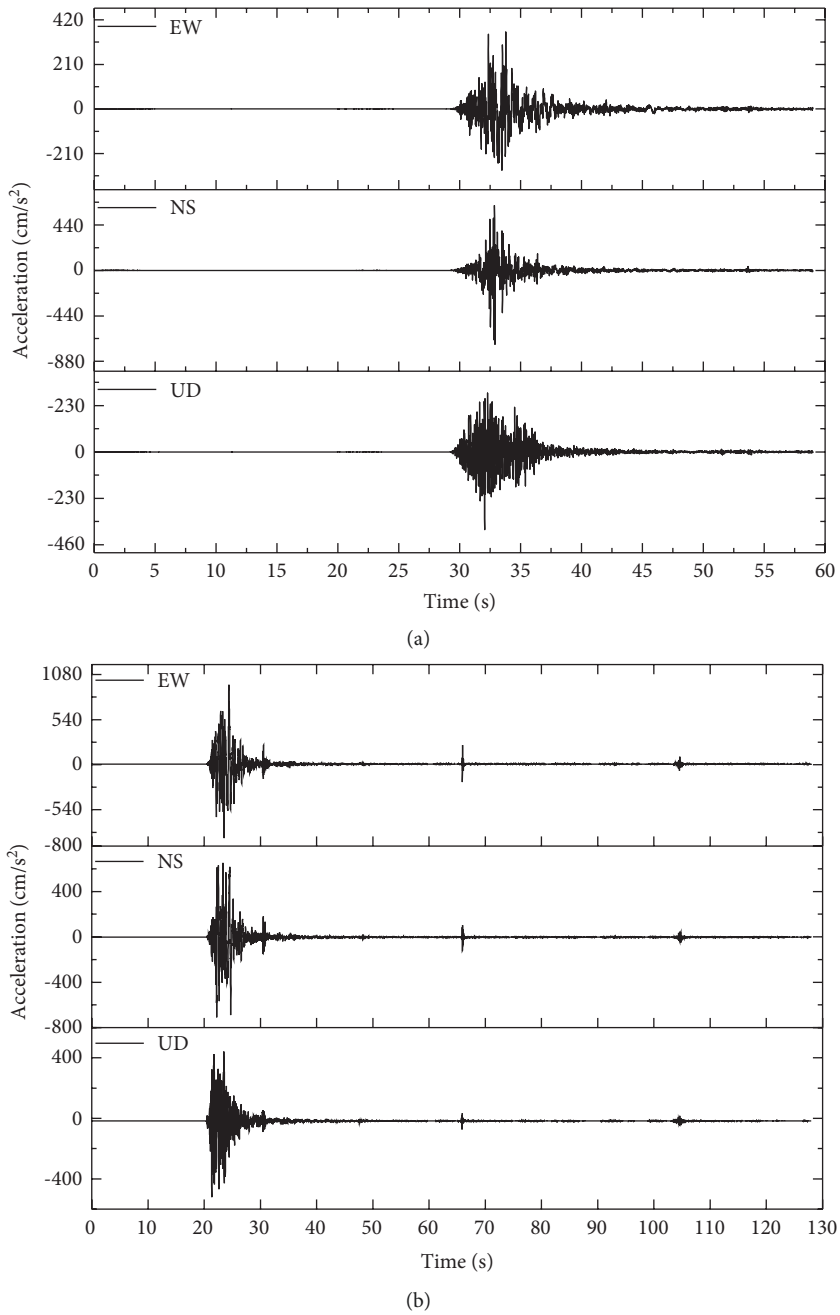

Figure 10: Acceleration time history of (a) 53YBX and (b) 53LLT.

$$y(t) = H[x(t)] = \frac{1}{\pi} P\left(\int_{-\infty}^{\infty} \frac{x(\tau)}{t-\tau} d\tau\right), \tag{8}$$

where $x(t)$ is the time history of the signal, which is equal to $u(t)$ in this study, and P is the Cauchy principal value.

An analytic signal $z(t)$ can be defined as

$$z(t) = x(t) + jy(t) = a(t)e^{j\theta(t)}. \tag{9}$$

The calculation method of $a(t)$ and $\theta(t)$ is shown in equations (10) and (11), respectively:

$$a(t) = \sqrt{x^2(t) + y^2(t)}, \tag{10}$$

$$\theta(t) = \arctan \frac{y(t)}{x(t)}. \tag{11}$$

The instantaneous frequency ($\omega(t)$) is the first derivative of $\theta(t)$ to time equation.

$$\omega(t) = \frac{d\theta(t)}{\mathrm{dt}}. \tag{12}$$

The Hilbert spectrum $H(t, \omega)$ is shown in the following equation:

$$H(t,w) = \sum_{1}^{m} a_i(t,w_i). \quad (13)$$

The marginal spectrum $h(w)$ is the integral of $H(t, \omega)$ over time, as shown in the following equation:

$$h(w) = \int_0^T H(t,w)\mathrm{d}t. \quad (14)$$

4. Characteristics of Seismic Signals

4.1. Time Domain Characteristics. Major characteristics such as PGA and duration of seismic wave record by the strong motion station can be acquired in the time domain.

The acceleration time history of 53YBX and 53LLT is shown in Figure 10. 53YBX station is 8.6 km away from the epicenter, and the PGAs in three directions were 379.8 cm/s^2 (EW), 720.3 cm/s^2 (NS), and 448.4 cm/s^2 (UD), respectively. 53LLT station is 8.3 km away from the epicenter, and the PGAs in three directions were 949.2 cm/s^2 (EW), −705.8 cm/s^2 (NS), and −504.4 cm/s^2 (UD), respectively. PGA attenuation rules of the two events are shown in Figure 11. In soil site, with the increase of epicentral distance, PGA in three directions has a decreasing tendency. In rock sites, PGA has a certain degree of increase. We should pay attention to the fact that PGA increases obviously at QJX, which may relate to the local landform.

The duration of an earthquake can reflect the cumulative damage effect of seismic signals on structures. There are two kinds of seismic signal duration, which are absolute duration and relative duration. In the earthquake engineering field, we mainly study the relative duration, which focuses on the strong part of seismic signals. Kawashima bracketed duration, which is a kind of relative duration, was used in the study to investigate the duration characteristics. It takes the duration of the first and last times reaching or exceeding 1/5~1/2 of the maximum peak acceleration as the duration, also known as fractional duration or relative peak duration. In this study, 0.3 is selected for calculation and analysis. The duration of strong motions of two earthquakes is shown in Table 2. The distribution of the duration is relatively discrete. In the Yangbi earthquake, the minimum duration is 2.1 s (53YBX-NS), and the maximum duration is 13.4 s (L3003-UD). In the Ludian earthquake, the minimum duration is 4.3 s (53LLT-UD), and the maximum duration is 15.3 s (53LDC-NS). The maximum PGA of two earthquakes occurred at 53YBX-NS and 53LLT-EW, respectively, and the duration of 53YBX-NS is less than 53LLT-EW, which indicates that the seismic signal of 53LLT has much cumulative damage effect on structures.

4.2. Time-Frequency-Energy Space Characteristics. Based on VMD and HT, the time-frequency-energy distribution characteristics of seismic waves can be obtained, which are mainly presented in the Hilbert spectrum and marginal spectrum in the study. The Hilbert spectrum reflects the distribution of time, frequency, and instantaneous energy. The marginal spectrum is the integral of the Hilbert spectrum over time, which can clarify the cumulative energy of every instantaneous frequency in the whole duration.

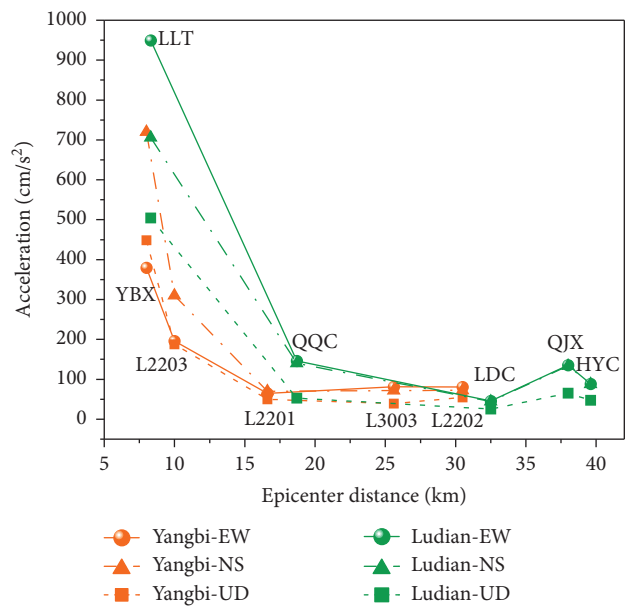

Figure 11: Attenuation of the PGA.

Table 2: Duration of strong motions.

Events	Station	Duration (s)		
		EW	NS	UD
Yangbi earthquake	53YBX	4.9	2.1	5.1
	L2203	4.6	2.3	5.9
	L2201	9.6	11.5	11.1
	L3003	12.2	11.7	13.4
	L2202	5.5	7.2	6.8
Ludian earthquake	53LLT	5.0	4.9	4.3
	53QQC	11.4	12.1	14.4
	53LDC	11.5	15.3	15.2
	53QJX	13.3	10.1	13.4
	53HYC	12.1	12.1	9.0

4.2.1. Hilbert Spectrum. The acceleration time history recorded by strong motion station has three components, and each of them contains meaningful information on seismic signals. In the time domain, it is not easy to synthesize the three components for the amplitude depending on the direction. Most studies mainly investigated the single component and ignored the others. However, in time-frequency-energy space, three components all present the distribution of time, frequency, and energy which are scalar. The synthesized Hilbert spectrum can reflect the instantaneous energy distribution of the seismic wave of a strong motion station completely. The Hilbert spectrums of 53YBX in three directions are shown in Figure 12. In the EW direction (Figure 12(a)), the energy is mainly distributed at 0–10 Hz and 10–20 Hz, respectively. However, in NS and UD directions (Figures 12(b)-12(c)), energy is mainly distributed at 10–20 Hz. The synthesized Hilbert spectrum of

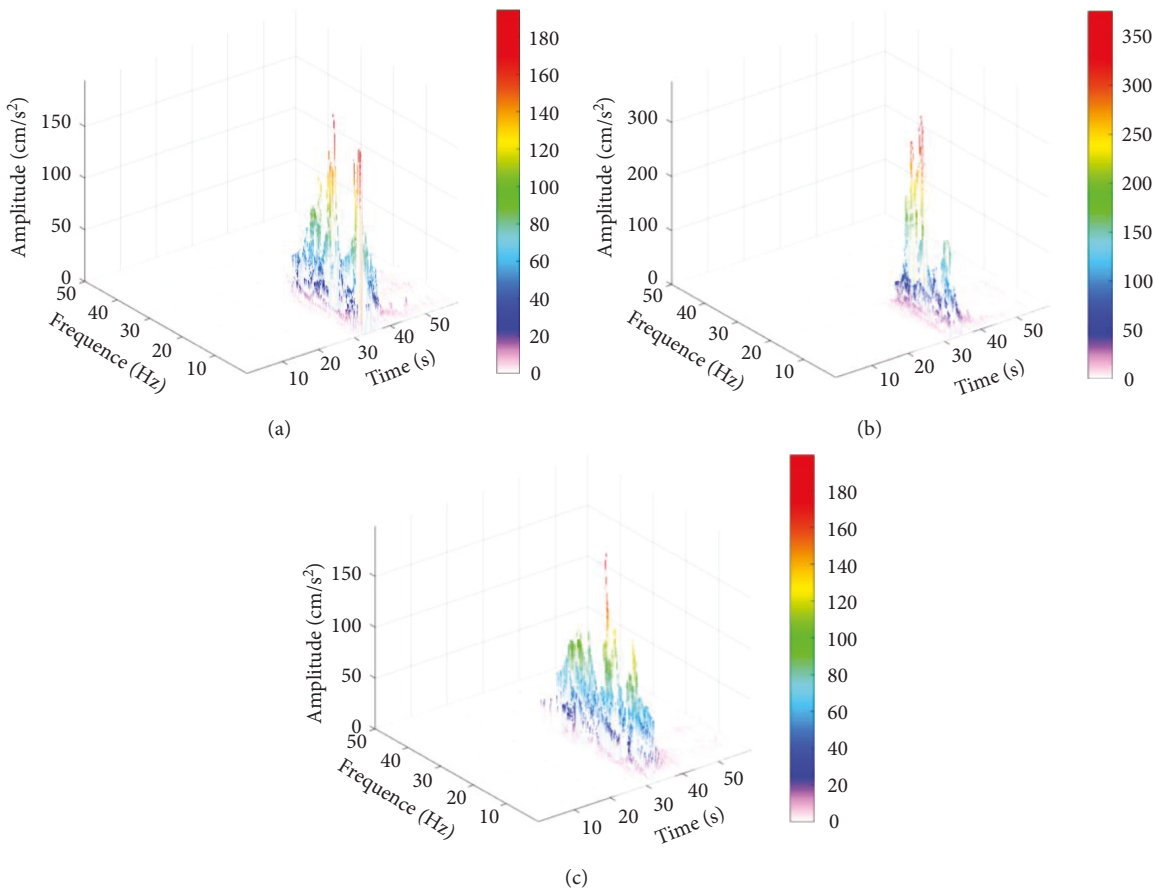

Figure 12: Hilbert spectrums of 53YBX in three directions. (a) 53YBX-EW. (b) 53YBX-NS. (c) 53YBX-UD.

53YBX is shown in Figure 13(a); two predominant frequencies are clearly clarified.

Hilbert spectrums of seismic waves recorded by different stations in the Yangbi earthquake are shown in Figures 13(a)–13(e). The shape of 53YBX presents double-peak, which are within 0–10 Hz and 10–20 Hz, respectively. However, the shape of others presents a single peak, and the instantaneous energy is mainly concentrated within 20 Hz. With the increase of epicentral distance, the energy shows a downward trend. However, the peak instantaneous energy has a slight increase in L3003 (from 52 cm/s^2 in L2201 to 73 cm/s^2 in L3003), which indicates that the soil layer can absorb peak instantaneous energy. Hilbert spectrums of seismic waves recorded by different stations in the Ludian earthquake are shown in Figures 13(f)–13(j). The shape of them shows a single peak, and the energy is mainly concentrated within 20 Hz. The peak instantaneous energy of them occurred within 10 Hz. The energy also shows a downward trend with the increases of epicentral distance, and the peak energy at the rock site (53HYC) is greater than that at the soil site when the epicentral distance is close. It should be noted that the energy at 53QJX has a significant increase in 53QJX (from 50 cm/s^2 in LDC to 130 cm/s^2 in 53QJX), which may be caused by its special site conditions and need to be investigated furtherly in our later works. The energy of 53LLT is concentrated at 5 Hz and the peak up to 1280 cm/s^2, which has a significant destructive instantaneous effect on long-period buildings. Compared with 53LLT, 53YBX contains relatively large energy in high-frequency (>10 Hz) parts, which has a destructive instantaneous effect on the short-period structures.

4.2.2. Marginal Spectrum. Marginal spectrums of seismic waves in the Yangbi earthquake are shown in Figure 14(a). In 53YBX, cumulative energy is mainly distributed in two frequency ranges, which are 0–5 Hz and 10–20 Hz, respectively. In other stations, cumulative energy is mainly distributed within 10 Hz. Peak cumulative energy shows a decreasing trend with the increases of epicentral distance, which is independent of site conditions. Marginal spectrums in the Ludian earthquake are shown in Figure 14(b). In 53LLT, the predominant frequency is 1.6 Hz, and the corresponding amplitude is much greater than it in other stations. The predominant frequency of other stations is within 3.8 Hz–4.3 Hz. Peak cumulative energy also shows a decreasing trend with the increases of epicentral distance. However, at 53QJX, cumulative energy shows an abnormal increase. This phenomenon also shows the Hilbert spectrum. Comparing the marginal spectrum of 53YBX with 53LLT, the difference is obvious. For 53LLT, large cumulative energy is concentrated at low frequency, which can induce the cumulative damage of long-period structures. For 53YBX, a large part of cumulative energy

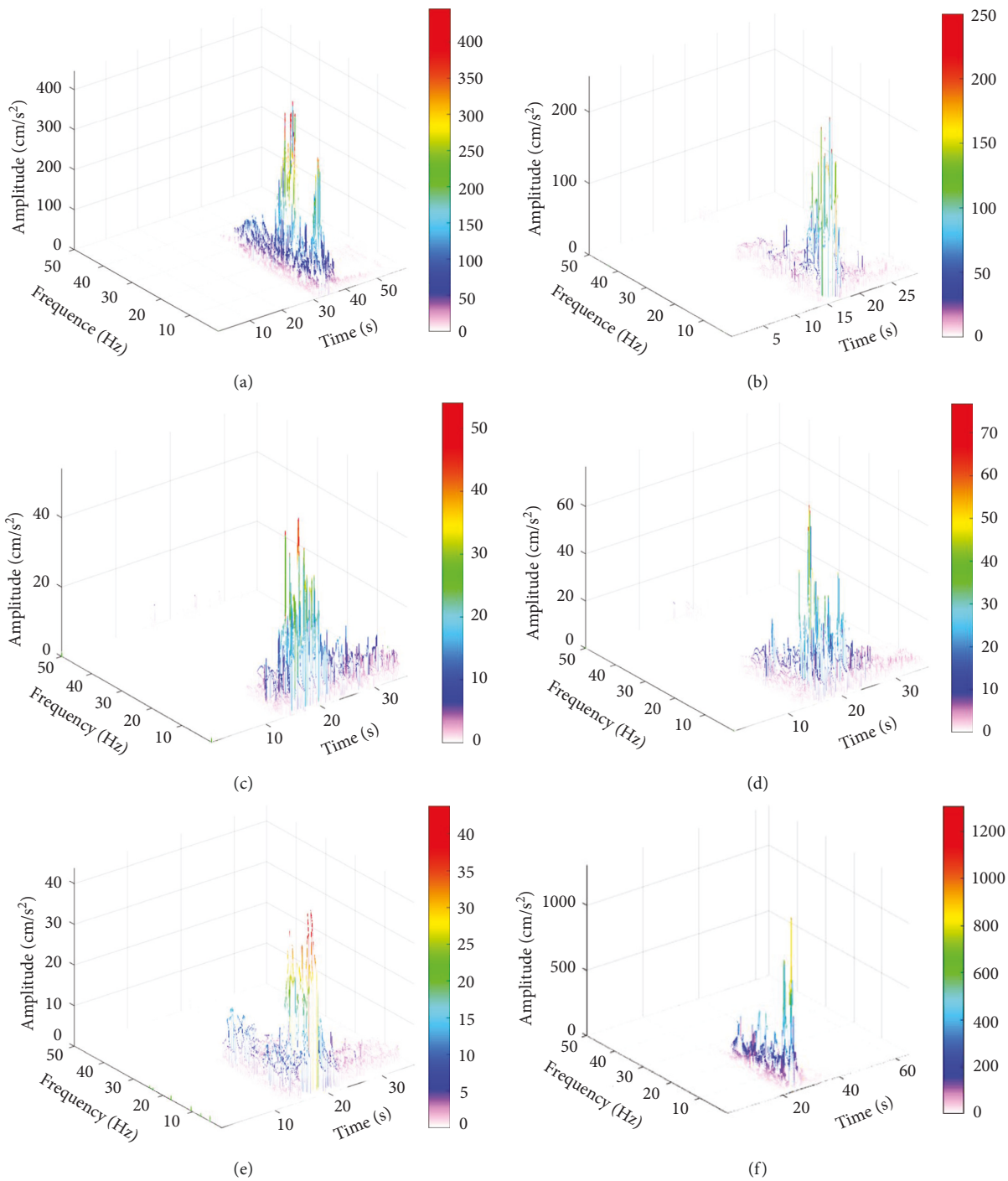

Figure 13: Continued.

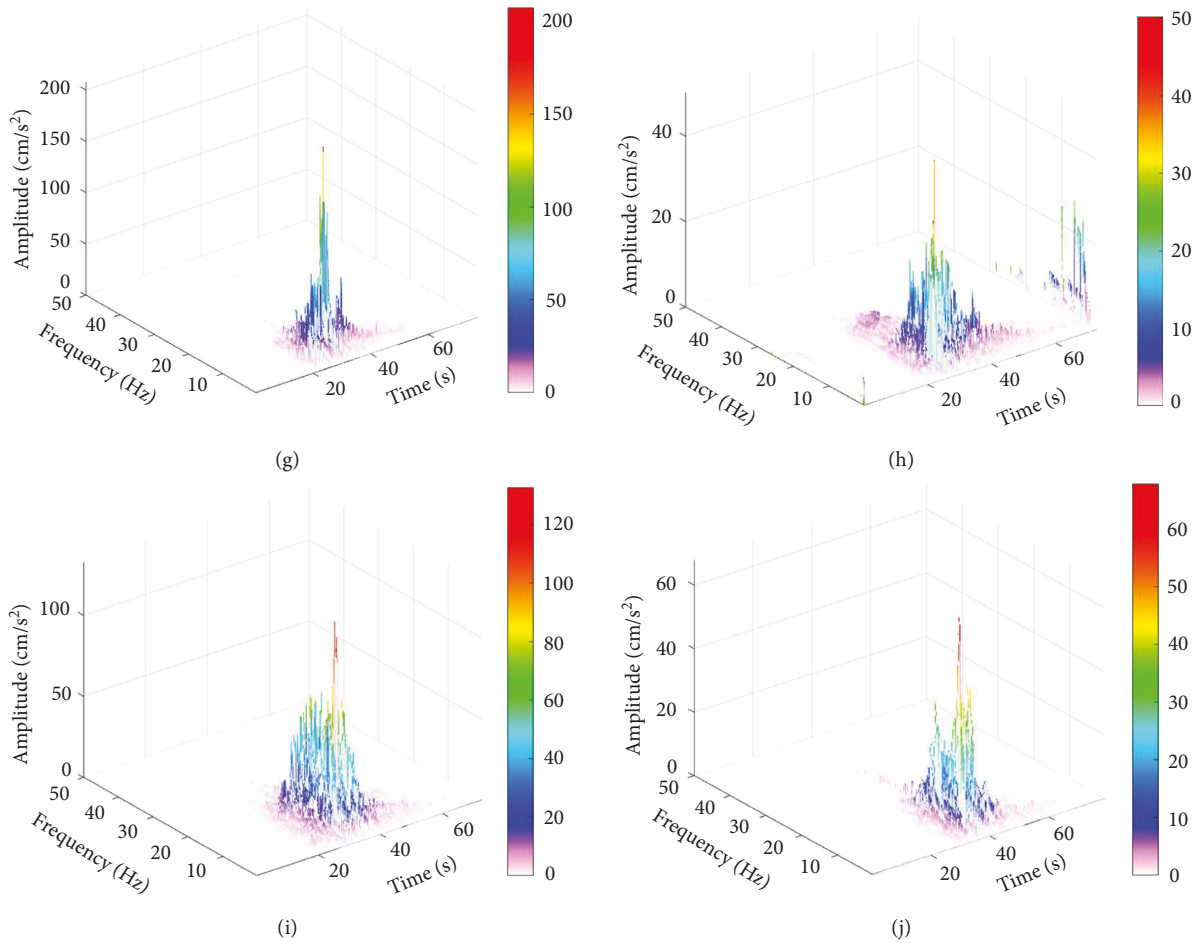

Figure 13: Hilbert spectrums of seismic wave in Yangbi earthquake and Ludian earthquake. (a) 53YBX. (b) L2203. (c) L2201. (d) L3003. (e) L2202. (f) 53LLT. (g) 53QQC. (h) 53LDC. (i) 53QJX. (j) 53HYC.

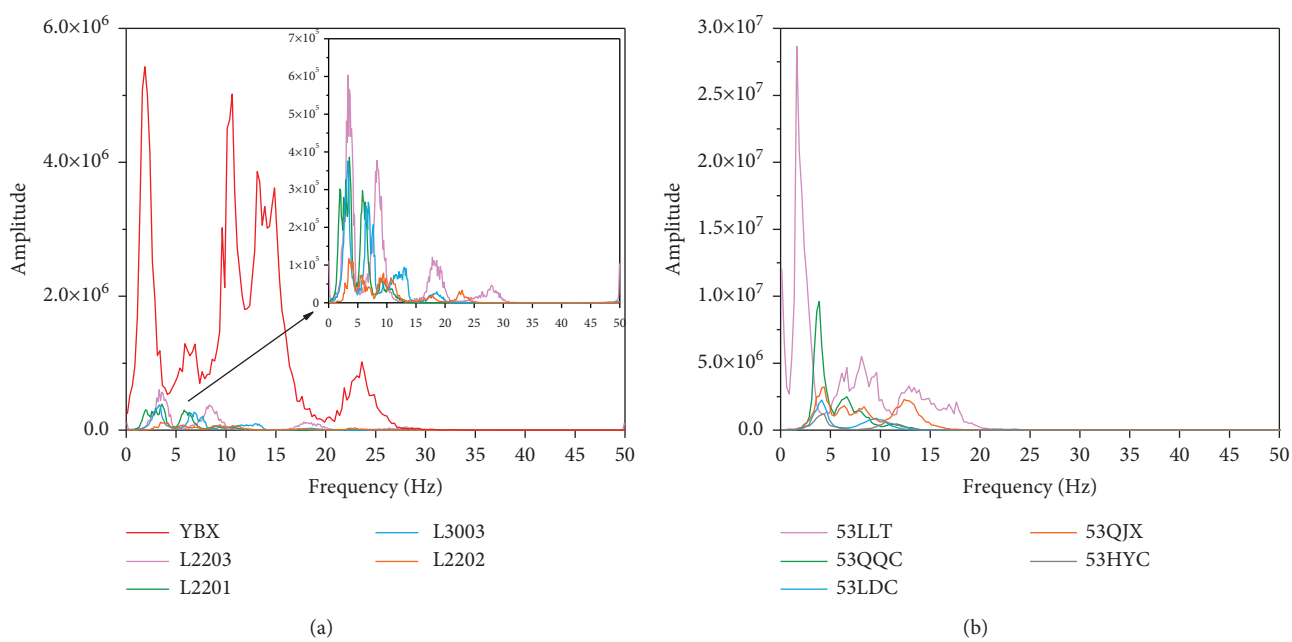

Figure 14: Marginal spectrums of seismic wave in Yangbi earthquake and Ludian earthquake. (a) Yangbi earthquake. (b) Ludian earthquake.

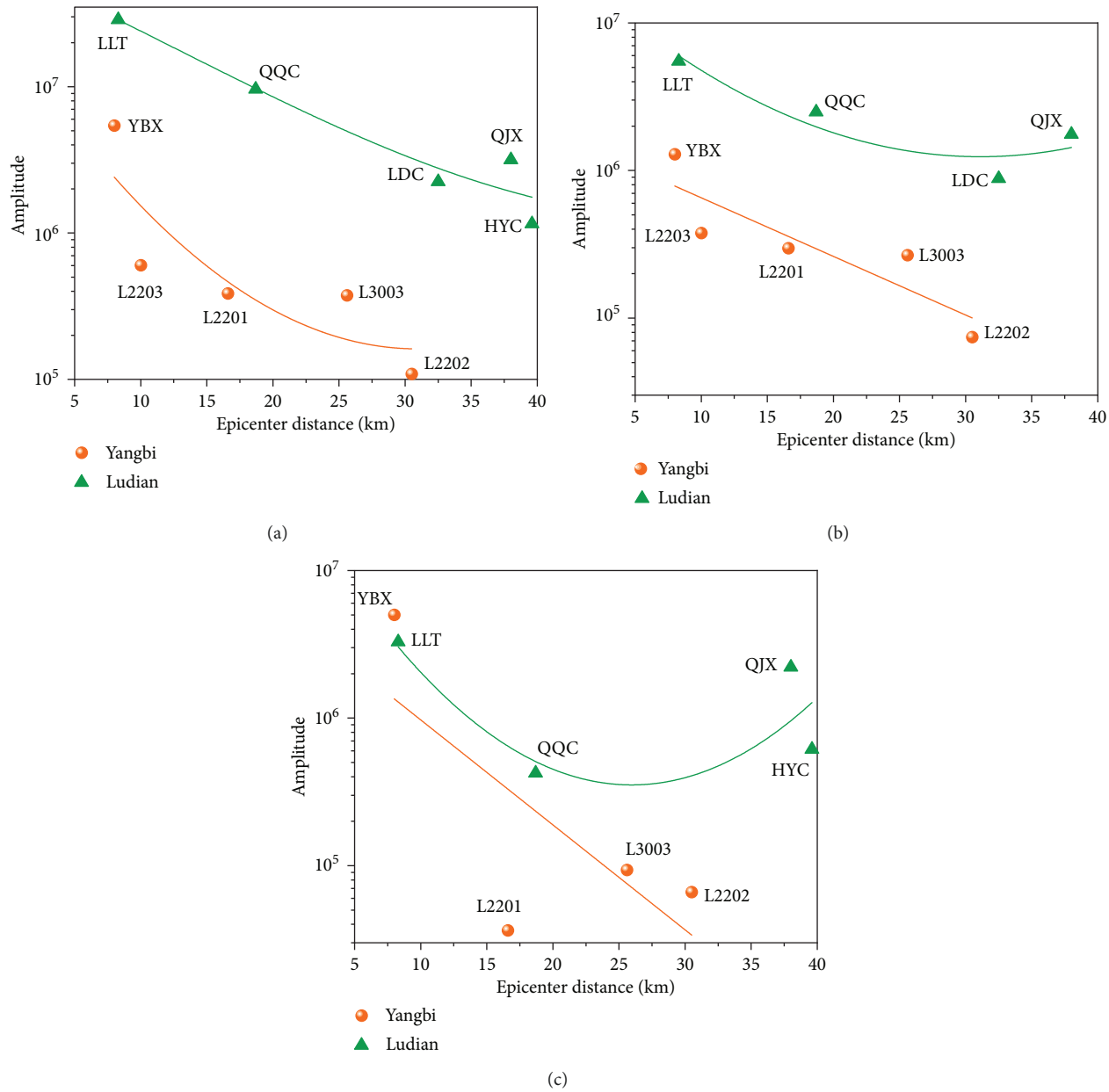

Figure 15: Attenuation of cumulative energy within different frequency ranges of the two events. (a) 0–5 Hz. (b) 5–10 Hz. (c) 10–15 Hz.

is concentrated at a high frequency, which can cause cumulative damage to the short-period structures.

According to the distribution characteristics of cumulative energy shown in Figure 14, we mainly investigate the attenuation rules of cumulative energy in three frequency ranges which are 0–5 Hz, 5–10 Hz, and 10–15 Hz, as it is shown in Figure 15. In three frequency ranges, with the increase of epicentral distance, the cumulative energy of the Yangbi earthquake decays faster than the energy of the Ludian earthquake. The energy of the Ludian earthquake is greater than the Yangbi earthquake when the epicentral distance is close. The result reflects that the seismic wave of the Ludian earthquake contains larger cumulative energy than the Yangbi earthquake and attenuates more slowly, which can cause more serious damage. It should be noticed that the energy in 10–15 Hz of 53YBX is even larger than 53LLT, although there is a 0.1 magnitude of difference between the two earthquakes, and the epicentral distance of the two stations is close. As mentioned above, the natural frequency of damaged buildings (column-and-tie timber structure with Earth wall) in the Yangbi earthquake is around 10 Hz. Large cumulative energy in high frequency (10–15 Hz) may cause the resonance of the structure. So, short-period structures in the Yangbi earthquake suffered serious cumulative damage.

5. Discussion

5.1. Effect of Frequency of Seismic Wave on Slope and Building. Disasters caused by two events show a big difference. In the Yangbi earthquake, the casualties and economic loss are

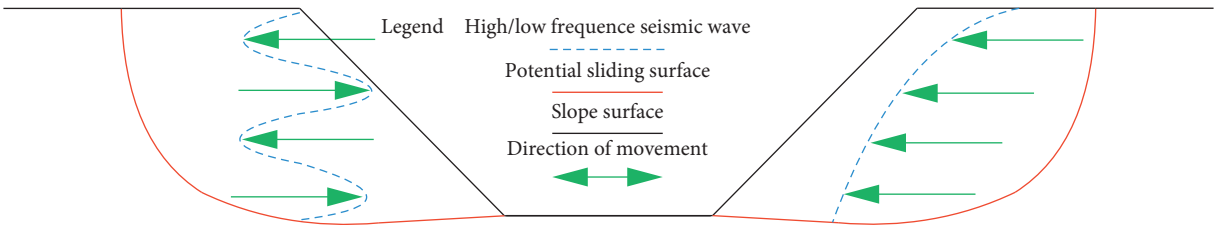

Figure 16: Effect of frequency of seismic wave on slope (modified from [31]).

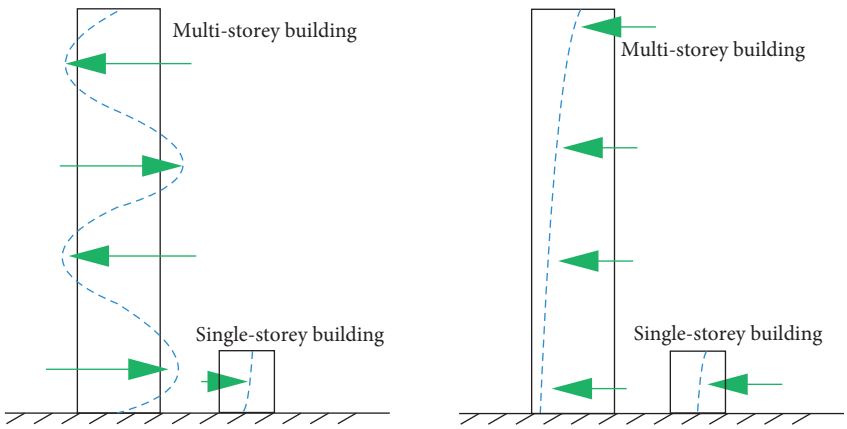

Figure 17: Effect of frequency of seismic wave on building.

minor. The most damaged building type is adobe and timber with single-storey and with local collapse or vertical crack occurring at the corner of retaining wall. There is no obvious damage to multistorey buildings. However, the epicenter of the Ludian earthquake suffered great damage. Frame structure and masonry structure with multistorey caused serious X-type cracking and large interlayer displacement and even complete collapse. Meanwhile, large landslides with a length of 165 m were triggered.

The effect of the frequency of a seismic wave on the movement of the slope is shown in Figure 16. In theory, a high-frequency seismic signal with a shorter wavelength than the dimensions of slopes is unlikely to trigger landslides because high-frequency seismic waves drive different parts of the slope in the opposite direction simultaneously, so the whole slope would remain stable. On the other hand, low-frequency seismic wave with a longer wavelength than dimensions of slopes can lead slope to move in the same direction, which is more likely to induce landslides [31]. Similarly, the frequency of seismic wave has the same effect on the building (Figure 17). The low-frequency seismic wave would lead multistorey building to move in the same direction, and the building easily collapsed. On the contrary, the building would remain stable under the effect of high frequency of the seismic wave. It is in accord with the damage phenomenon of slope and buildings in Yangbi County and Longtou Village. This study shows that 53LLT contains large instantaneous energy and cumulative energy in low-frequency parts; however, 53YBX contains large energy in high-frequency parts. Thus, the large energy in high frequency caused instantaneous and cumulative damage to short-period structures in Yangbi County. Accordingly, the large energy in low frequency caused instantaneous and cumulative damage to long-period structures (multistorey buildings) and large landslides in Longtou Village.

5.2. Site Effect Characteristics. In order to investigate the site effect in two events, we use the horizontal to vertical Fourier spectral ratio (HVSR) of seismic signals to evaluate it. The method is proposed by Nakamura [32–34] and has developed into a standard technique to study site effects [35, 36]. The expression is shown in equation (15). In the study, the Fourier spectrum of the horizontal seismic signal is the synthetic seismic signal of EW and NS. Similarly, we calculated the horizontal to vertical marginal spectral based on the VMD and Hilbert transform (VHT) ratio of seismic signals in order to compare with the ratio based on the fast Fourier transform (FFT).

HVSR results based on FFT and VHT, respectively, are shown in Figure 18. The change rules of the FFT ratio and VHT ratio of different stations in two earthquakes are close. Two methods can recognize the predominant frequency of the sites, and the predominant frequency value is close. However, the amplitude has a certain difference, and the predominant frequency recognized by the VHT ratio is clearer than that by the FFT ratio. Peak amplitude (with FFT ratio 26 and VHT ratio 49) occurred at 53QJX, and the predominant frequency is about 5 Hz, which indicates that relatively large instantaneous energy and cumulative energy here are related to the local site conditions. The amplification effects (amplitude) of 53YBX and 53LLT are not obvious compared with other stations, which reflects that the distribution of instantaneous energy and cumulative

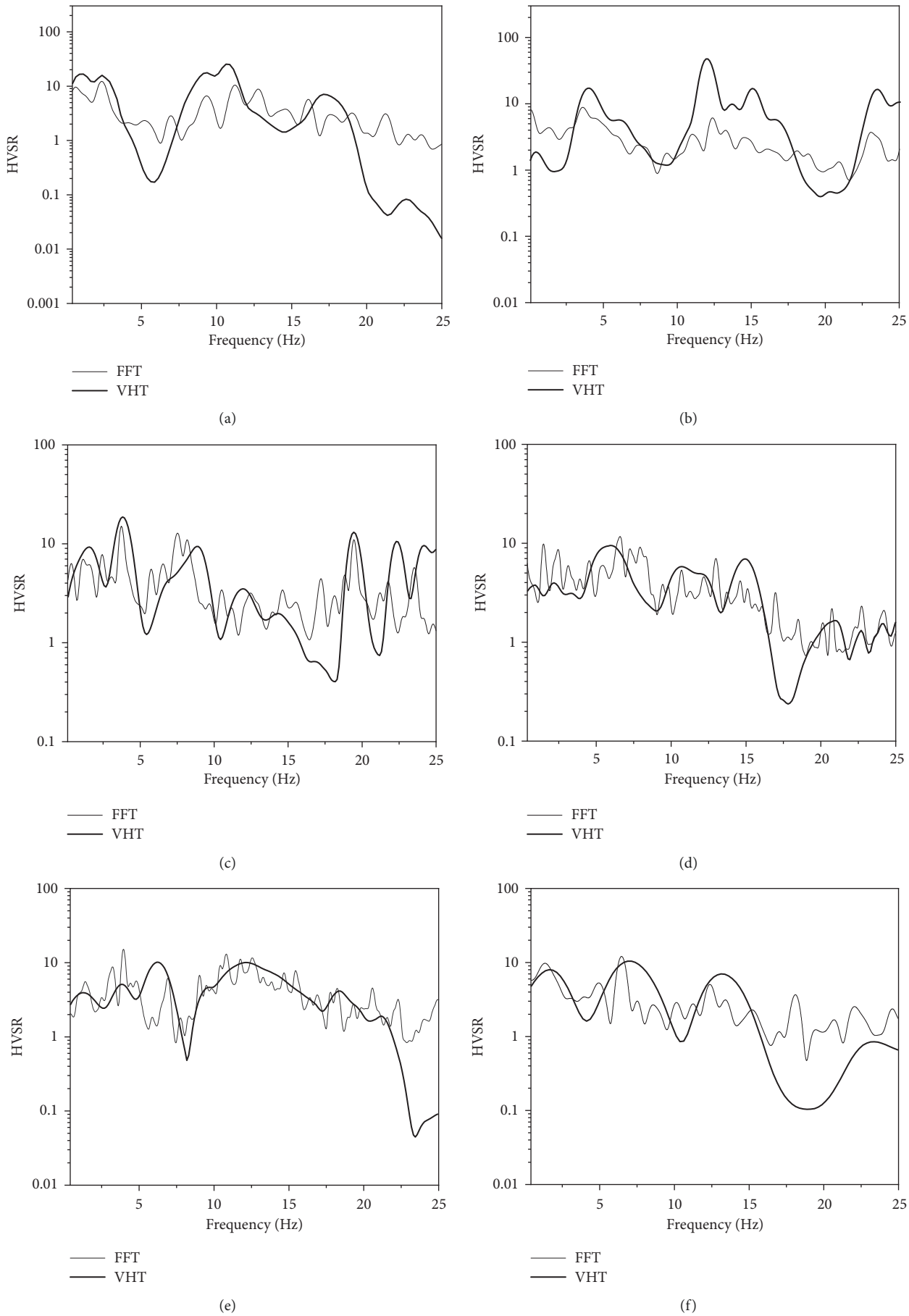

Figure 18: Continued.

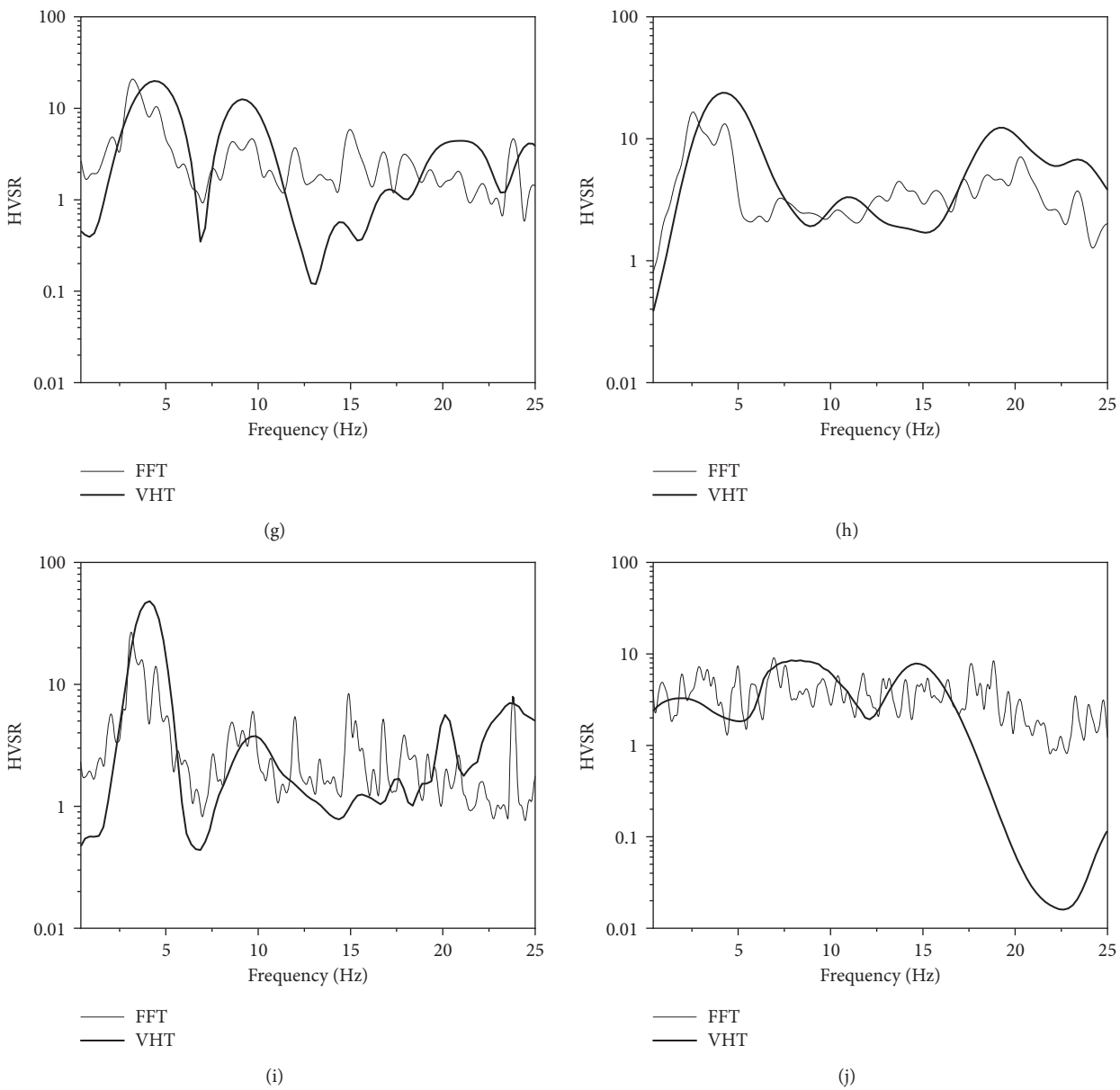

Figure 18: HVSRs based on FFT and VHT of the two events. (a) 53YBX. (b) L2203. (c) L2201. (d) L3003. (e) L2202. (f) 53LLT. (g) 53QQC. (h) 53LDC. (i) 53QJX. (j) 53HYC.

energy of the two stations mainly reflected the hypocenter characteristics.

$$R(f) = \frac{H(f)}{V(f)}, \tag{15}$$

where $H(f)$ is the Fourier spectrum of the horizontal seismic signal and $V(f)$ is the Fourier spectrum of the vertical seismic signal.

5.3. Low-Frequency Pulse Signal Extraction Based on VMD Method. Many studies have been done on the reasons for the large disaster in Longtou town caused by the Ludian earthquake. One main reason among them is the large-amplitude pulse contained in the time history of 53LLT [37–39]. Pulse-type seismic signal has more complex characteristics than ordinary seismic signal and can lead to serious damage to engineering structures [40, 41]. The Port Hueneme Mw 4.7 earthquake in 1957, the Parkfield Mw 5.6 earthquake in 1966, and the San Fernando Mw 6.6 earthquake in 1971 all showed the characteristics of small magnitude and serious disasters, and pulse-type seismic signals were recorded in these events [42, 43]. So, there is a need to identify, extract, and model the pulse-type seismic signal for further structural seismic analysis. However, the identification method requires visual inspection or repeat using wavelet transform [44, 45], and the method is based on the velocity time history of the seismic signal. In this study, an identification or extraction method using acceleration time history is proposed.

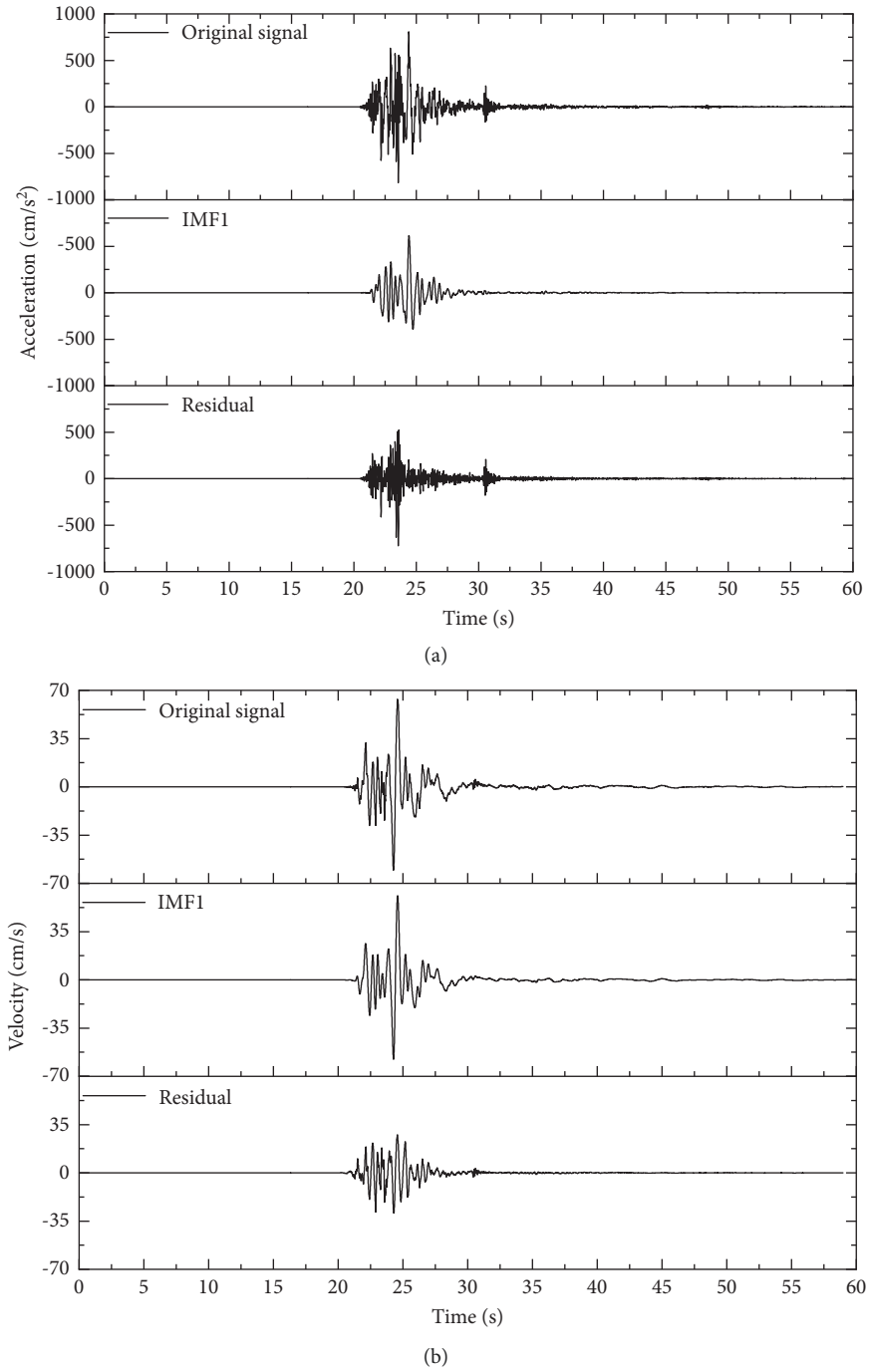

Figure 19: Acceleration and velocity time history of 53LLT (EW). (a) Acceleration time history. (b) Velocity time history.

Figure 19(b) shows the velocity time history of 53LLT (EW), which is the integral of the acceleration time history of 53LLT (EW) shown in Figure 19(a). The result shows that 53LLT (EW) contains a short-term velocity pulse of around 25 s, and IMF1 is the major component of the short-term velocity pulse of the original signal. The method based on VMD can effectively extract the pulse components from the acceleration time history of the seismic signals.

6. Conclusions

An Ms 6.4 earthquake occurred in Yangbi County, Yunnan Province, on May 21, 2021. Compared with Ms 6.5 Ludian earthquake that occurred in Yunnan Province on 2014, the disasters have a big difference, even the magnitude with 0.1 difference. The study mainly introduced the difference in seismic signals of epicenters of two earthquakes. The main conclusions are shown as follows.

The Yangbi Ms 6.4 earthquake caused 3 deaths, 32 injuries, 13000 damaged buildings and triggered a few small landslides. The epicenter intensity is VIII. Column-and-tie timber structure with Earth wall caused local collapse or vertical crack at the corner of Earth wall, which takes the largest ratio among the damaged buildings at the epicenter, and the multistorey buildings do not have obvious damage phenomenon. The Ludian Ms 6.5 earthquake caused 617 deaths, 2400 injuries, 86000 destroyed buildings and triggered many large landslides. The epicenter intensity is up to IX. Frame structure and masonry structure with multistorey in epicenter caused serious X-type cracking, large interlayer displacement, and even complete collapse.

PGAs of 53YBX in three directions are 379.8 cm/s^2 (EW), 720.3 cm/s^2 (NS), and 448.4 cm/s^2 (UD), and the PGAs of 53LLT in three directions are 949.2 cm/s^2 (EW), −705.8 cm/s^2 (NS), and −504.4 cm/s^2 (UD). PGA in the Ludian earthquake attenuates faster than that in the Yangbi earthquake with the increases of epicentral distance, and the duration in 53LLT is longer than 53YBX. The large PGA and long duration of the seismic signal may cause serious damage to the building in Longtou Village.

The Hilbert spectrum shape of 53YBX presents a double peak, and the instantaneous energy is concentrated within 0–10 Hz and 10–20 Hz, respectively. The Hilbert spectrum shape in the Ludian earthquake shows a single peak. The instantaneous energy of 53LLT is concentrated at 5 Hz, and the peak is up to 1280 cm/s^2, which may have a significant destructive instantaneous effect on long-period buildings. The marginal spectrum shows that, in 53YBX, cumulative energy is mainly distributed in two frequency ranges, which are 0–5 Hz and 10–20 Hz, respectively. In 53LLT, the predominant frequency is 1.6 Hz, and the cumulative energy is much greater than that in other stations. The large energy in low frequency caused instantaneous and cumulative damage to long-period structures in Longtou Village. The large energy in high frequency caused instantaneous and cumulative damage to short-period structures in Yangbi County and may cause the resonance of column-and-tie timber structure.

Data Availability

Basic data can be obtained from the corresponding author when needed. Data for this study are provided by the Institute of Engineering Mechanics, China Earthquake Administration.

Conflicts of Interest

The authors declare that they have no conflicts of interest.

Acknowledgments

This research work was supported by the National Key R&D Program of China (2018YFC1504506 and 2018YFC1504504) and the Key Project of National Natural Science Foundation of China (no. U1939209).

References

[1] X. W. An, Z. F. Chang, and Y. J. Chen, *Quaternary Active Faults in Yunnan*, Seismological Press, Beijing, China, 2018.

[2] W. C. Li, G. Deng, W. Cao, C. Xu, J. Chen, and M. L. Lee, "Discrete element modeling of the Hongshiyan landslide triggered by the 2014 Ms 6.5 Ludian earthquake in Yunnan, China," *Environmental Earth Sciences*, vol. 78, no. 16, p. 520, 2019.

[3] G. Huangfu, Y. Chen, and J. Z. Qin, *Seismicity in Yunnan, Kunming*, Yunnan Science and Technology Press, Kunming, China, 2010.

[4] S. G. He, H. Ran, Q. Y. Zhou, J. Yu, W. D. Luo, and X. F. Bai, "Seismic reinforcement performance of civil structure houses during Yangbi Ms 6.4 earthquake," *China Earthquake Engineering Journal*, vol. 43, no. 4, pp. 799–806, 2021, (In Chinese).

[5] Y. Q. Zhang, W. F. Chen, Y. K. Lu, K. H. Chen, G. L. Lin, and S. C. Li, "Research on the disaster characteristics of three Ms>6 earthquakes in yunnan in 2014," *Journal of Seismological Research*, vol. 40, no. 1, pp. 144–152, 2017, (In Chinese).

[6] Y. Huang, L. Y. Zhao, M. Xiong, C. Liu, and P. Lu, "Critical slip surface and landslide volume of a soil slope under random earthquake ground motions," *Environmental Earth Sciences*, vol. 77, no. 23, p. 787, 2018.

[7] A. Kafaei Mohammadnejad, S. M. Mousavi, M. Torabi, M. Mousavi, and A. H. Alavi, "Robust attenuation relations for peak time-domain parameters of strong ground motions," *Environmental Earth Sciences*, vol. 67, no. 1, pp. 53–70, 2012.

[8] S. Lagomarsino and S. Cattari, "PERPETUATE guidelines for seismic performance-based assessment of cultural heritage masonry structures," *Bulletin of Earthquake Engineering*, vol. 13, no. 1, pp. 13–47, 2015.

[9] E. A. Dizaj, R. Madandoust, and M. M. Kashani, "Probabilistic seismic vulnerability analysis of corroded reinforced concrete frames including spatial variability of pitting corrosion," *Soil Dynamics and Earthquake Engineering*, vol. 114, pp. 97–112, 2018.

[10] Y. X. Hu, *Earthquake Engineering*, Seismological Press, Beijing, China, 2006.

[11] T. C. Hanks and H. Kanamori, "A moment magnitude scale," *Journal of Geophysical Research*, vol. 84, no. B5, p. 2348, 1979.

[12] Y. Shoji, K. Tanii, and M. Kamiyama, "A study on the duration and amplitude characteristics of earthquake ground motions," *Soil Dynamics and Earthquake Engineering*, vol. 25, no. 7-10, pp. 505–512, 2005.

[13] A. K. Chopra, "Earthquake resistant design of concrete gravity dams," *Journal of the Structural Division*, vol. 104, no. 6, pp. 953–971, 1978.

[14] Q. J. Chen, W. Z. Yuan, Y. C. Li, and L. Y. Cao, "Dynamic response characteristics of super high-rise buildings subjected to long-period ground motions," *Journal of Central South University*, vol. 20, no. 5, pp. 1341–1353, 2013.

[15] M. G. Tian and W. J. Yi, "Dynamic behavior of reinforced concrete frame structure during construction," *Journal of Central South University of Technology*, vol. 15, no. 3, pp. 418–422, 2008.

[16] N. E. Huang, Z. Shen, S. R. Long et al., "The empirical mode decomposition and the Hilbert spectrum for nonlinear and non-stationary time series analysis," *Proceedings of the Royal Society of London. Series A: Mathematical, Physical and Engineering Sciences*, vol. 454, no. 1971, pp. 903–995, 1998.

[17] J. C. Chen, L. M. Wang, P. Wang, and A. L. Che, "Failure mechanism investigation on loess-mudstone landslides based on the Hilbert-Huang transform method using a large-scale

shaking table test," *Engineering Geology*, vol. 302, p. 106630, Article ID 106630, 2022.

[18] S. R. Garcia, M. P. Romo, and L. Alcántara, "Analysis of non-linear and non-stationary seismic recordings of Mexico City," *Soil Dynamics and Earthquake Engineering*, vol. 127, p. 105859, Article ID 105859, 2019.

[19] S. Chowdhury, A. Deb, M. Nurujjaman, and C. Barman, "Identification of pre-seismic anomalies of soil radon-222 signal using Hilbert-Huang transform," *Natural Hazards*, vol. 87, no. 3, pp. 1587–1606, 2017.

[20] Y. Changwei, F. Ning, Z. Jianjing, B. Junwei, and Z. Jun, "Research on time-frequency analysis method of seismic stability of covering-layer type slope subjected to complex wave," *Environmental Earth Sciences*, vol. 74, no. 6, pp. 5295–5306, 2015.

[21] T. Liu, Z. J. Luo, J. H. Huang, and S. Yan, "A comparative study of four kinds of adaptive decomposition algorithms and their applications," *Sensors*, vol. 18, no. 7, p. 2120, 2018.

[22] K. Dragomiretskiy and D. Zosso, "Variational mode decomposition," *IEEE Transactions on Signal Processing*, vol. 62, no. 3, pp. 531–544, 2014.

[23] M. Thomas, D. Zarour, S. Meziani, and M. Kedadouche, "Faulty bearing features by variational mode decomposition," *Vibroengineering PROCEDIA*, vol. 16, pp. 29–34, 2017.

[24] Y. F. Guo, Z. S. Zhang, T. Gong, J. B. Cao, and W. Z. Yang, "Generalized variational mode decomposition for interlayer slipping detection of viscoelastic sandwich cylindrical structures," *Measurement Science and Technology*, vol. 29, no. 9, p. 095001, Article ID 095001, 2018.

[25] C. Y. Li, J. Y. Zhang, W. Wang, K. Sun, and X. J. Shan, "The seismogenic fault of the 2021 Yunnan Yangbi M_S 6.4 earthquake," *Seismology and Geology*, vol. 43, no. 3, pp. 706–721, 2021, (In Chinese).

[26] Z. R. Pan, T. L. Li, J. W. Cui et al., "Characteristics of strong motion records of the Yangbi Ms 6.4 and related earthquakes on May 21, 2021," *China Earthquake Engineering Journal*, vol. 43, no. 4, pp. 791–798, 2021, (In Chinese).

[27] S. C. Liu, Y. K. Lu, Y. Zhou et al., "Characteristics of earthquake damage caused by the 2021 Yangbi, yunnan MS6. 4 earthquake," *Journal of Seismological Research*, vol. 44, no. 03, pp. 452–460, 2021, (In Chinese).

[28] H. C. Jia, F. Chen, Y. D. Fan, and D. H. Pan, "Comparison of two large earthquakes in China: the ms 6.6 yunnan Jinggu earthquake and the ms 6.5 yunnan ludian earthquake in 2014," *International Journal of Disaster Risk Reduction*, vol. 16, pp. 99–107, 2016.

[29] X. Chaoxu, N. Gaozhong, F. Xiwei, L. Huayue, Z. Junxue, and Z. Xun, "A new model for the quantitative assessment of earthquake casualties based on the correction of anti-lethal level," *Natural Hazards*, vol. 110, no. 2, pp. 1199–1226, 2022.

[30] B. Zhang, X. J. Li, M. S. Rong, Y. X. Yu, Y. S. Wang, and J. X. Wang, "Analysis of strong ground motion characteristics and earthquake damage for the Yangbi Ms 6.4 earthquake, Yunnan," *Seismology and Geology*, vol. 43, no. 5, pp. 1127–1139, 2021, (In Chinese).

[31] S. L. Kramer and M. W. Smith, "Modified Newmark model for seismic displacements of compliant slopes," *Journal of Geotechnical and Geoenvironmental Engineering*, vol. 123, no. 7, pp. 635–644, 1997.

[32] L. Agostini, J. Boaga, A. Galgaro, and A. Ninfo, "HVSR technique in near-surface thermal-basin characterization: the example of the Caldiero district (North-East Italy)," *Environmental Earth Sciences*, vol. 74, no. 2, pp. 1199–1210, 2015.

[33] J. D. Thornley, U. Dutta, J. Douglas, and Z. J. Yang, "Evaluation of horizontal to vertical spectral ratio and standard spectral ratio methods for mapping shear wave velocity across anchorage, Alaska," *Soil Dynamics and Earthquake Engineering*, vol. 150, Article ID 106918, 106918 pages, 2021.

[34] İT. Güven, "Seismic vulnerability indices for ground in Derince-Kocaeli (NW Turkey)," *Environmental Earth Sciences*, vol. 81, no. 5, p. 167, 2022.

[35] S. Yang, G. P. Mavroeidis, J. C. de la Llera et al., "Empirical site classification of seismological stations in Chile using horizontal-to-vertical spectral ratios determined from recordings of large subduction-zone earthquakes," *Soil Dynamics and Earthquake Engineering*, vol. 125, Article ID 105678, 105678 pages, 2019.

[36] Y. A. Nakamura, "Method for dynamic characteristics estimation of subsurface using microtremor on the ground surface," *Quarterly Report of Railway Technical Research Institute*, vol. 30, no. 1, pp. 25–33, 1989.

[37] P. B. Xu, R. Z. Wen, H. W. Wang, K. Ji, and Y. F. Ren, "Characteristics of strong motions and damage implications of M S6.5 Ludian earthquake on August 3, 2014," *Earthquake Science*, vol. 28, no. 1, pp. 17–24, 2015.

[38] P. B. Xu, R. Z. Wen, and Y. F. Wen, "Comparison of strong-motion records and damage implications between the 2014 Yunnan Ms 6.5 Ludian earthquake and Ms 6.6 Jinggu earthquake," *Earthquake Science*, vol. 31, no. 1, pp. 12–18, 2018.

[39] Z. Qu and X. Shi, "Comparative study on the pulse-like seismic signals in the Wenchuan and the Ludian earthquakes," *Engineering Mechanics*, vol. 33, no. 8, pp. 150–157, 2016, (In Chinese).

[40] R. Sehhati, A. Rodriguez-Marek, M. Eigawady, and W. F. Cofer, "Effects of near-fault seismic signals and equivalent pulses on multistory structures," *Engineering Structures*, vol. 33, no. 3, pp. 767–779, 2011.

[41] C. H. Zhai, S. Li, L. L. Xie, and Y. M. Sun, "Study on inelastic displacement ratio spectra for near-fault pulse-type ground motions," *Earthquake Engineering and Engineering Vibration*, vol. 6, no. 4, pp. 351–355, 2007.

[42] G. W. Housner and D. E. Hudson, "The port hueneme earthquake of march 18, 1957," *Bulletin of the Seismological Society of America*, vol. 48, no. 2, pp. 163–168, 1958.

[43] G. P. Mavroeidis and A. S. Papageorgiou, "A mathematical representation of near-fault ground motions," *Bulletin of the Seismological Society of America*, vol. 93, no. 3, pp. 1099–1131, 2003.

[44] J. W. Baker, "Quantitative classification of near-fault ground motions using wavelet analysis," *Bulletin of the Seismological Society of America*, vol. 97, no. 5, pp. 1486–1501, 2007.

[45] S. Mukhopadhyay and V. K. Gupta, "Directivity pulses in near-fault ground motions—I: identification, extraction and modeling," *Soil Dynamics and Earthquake Engineering*, vol. 50, pp. 1–15, 2013.